UNIVERSITÀ DEGLI STUDI DI CATANIA
FACOLTÀ DI SCIENZE MATEMATICHE, FISICHE E NATURALI
DOTTORATO DI RICERCA IN FISICA – XXIV CICLO

Gaetano Scandariato

THE INITIAL MASS FUNCTION OF THE ORION NEBULA CLUSTER FROM NEAR-INFRARED PHOTOMETRY

Ph.D. Thesis

Supervisor:
Prof. A.C. Lanzafame

Tutors:
Doct. I. Pagano
Doct. M. Robberto

Coordinator:
Prof. F. Riggi

anno accademico 2011/2012

“Fussiro tutti comu a tia…”
“Comu?”
“Forti…”
“Puru tu a’ essiri forti, figghiu meu!”

Contents

Abstract

An important issue for the understanding of the star and planet formation process is the determination of the Initial Mass Function (IMF), in particular in the very low-mass and sub-stellar regimes, where recent investigations give controversial results.

The main goal of this thesis is the complete characterization of the IMF of the Orion Nebula Cluster (ONC) down to the Brown Dwarfs (BDs) regime, using ground-based Near-Infrared (NIR) photometric observations. The data taken in the framework of the Hubble Space Telescope (HST) Treasury Program on the ONC have been obtained with the wide-field imager Infrared Side Port Imager (ISPI) at the Blanco 4m telescope of CTIO, and cover an area of about 0.25 square degrees roughly centered on Θ^1OriC. We observed the region in the JHK_S bands with exposure times of 330 s. As a result of our survey, we provide 2MASS-calibrated astrometry and photometry for ∼7000 sources in the ONC region.

Aiming at the photometric determination of the IMF of the ONC, we first clean the catalog for contaminants. We thus analyze the observed $(H, H-K_S)$ Color-Magnitude Diagram (CMD), and we select a sample of bona-fide contaminant background stars, deriving the interstellar reddenings by comparison with a synthetic galactic model. A statistical analysis is then performed to consistently account for local extinction, reddening and star-counts analysis in order to derive the background extinction map of the Orion Molecular Cloud 1 (OMC-1). The derived map has angular resolution $<5'$ and shows spatial structures of a few arcminutes and a general increase from the outskirts ($A_V \sim 6$) to the direction of the Trapezium asterism ($A_V \gtrsim 30$). Similarly, we select a sample of bona-fide cluster members and we compare the observed colors to the expected colors for Pre-Main Sequence (PMS) stars, deriving the extinction map of the foreground Orion Nebula (ON) with angular resolution $<7\overset{'}{.}5$. The ON extinction map is more irregular and optically thinner than the one of the OMC-1,

with A_V of the order of $\lesssim$3 magnitudes. Both maps show the presence of a north-south high-density ridge, which confirms the filamentary structure of the Orion molecular complex inside which star formation is still taking place.

We then analyze a sample of ∼300 stars with previous measurements of luminosities, temperatures and simultaneous optical and NIR photometry. By analyzing their photospheric colors, we find that the synthetic JHK_S photometry provided by theoretical spectral templates for late spectral types (>K6) are accurate only to a level of ∼0.2 mag. We can thus provide an empirically-determined isochrone for low mass stars (spectral types later than K6) in the ONC, necessary to convert magnitudes into temperatures and masses.

Comparing the extinction-corrected magnitudes with our empirical isochrone, we derive the flux excess in the three JHK_S bands, that we attribute to the presence of a circumstellar disk. The observed fraction of disked stars ($\gtrsim$ 20% of the total sample) does not show any trend with stellar mass or stellar age. On the other hand, it increases with decreasing distance from the cluster center, consistently with the fact that the UV radiation field in the ON interacts with circumstellar disks forming the inflated structures known as "proplyds".

Combining the previous results, we derive the contamination-completeness corrected (J,J-H) CMDs of the ONC, canceling out the contribution from the contaminant population. We also develop a statistical algorithm, which combines the CMD of the ONC with our reference isochrone and, taking into account the presence of extinction and NIR excess, derives the intrinsic Luminosity Function (LF) of the cluster. We finally combine the LF with our empirical NIR isochrone to derive a statistical estimate of the IMF at different distances from the cluster center. We find that the mass distribution of the cluster is peaked at ∼0.16 $M_\odot$ and falls off crossing the hydrogen burning limit, continuously decreasing in the BDs domain down to ∼0.03 $M_\odot$. We also find that the substellar-to-stellar objects ratio in the ONC decreases with increasing distance from the cluster center, suggesting that BDs are preferentially formed in the deep gravitational potential well where the most massive stars of the Trapezium cluster are also found.

Introduction

A fundamental relation for understanding star formation and the evolution of stellar systems is the Initial Mass Function (IMF), that specifies the distribution in mass of a newly formed stellar population.

The shape of the IMF describes how long the galactic material will remain locked up in stars of different masses, since the stellar mass determines both its lifetime and its contribution to enriching the interstellar medium with heavy elements, especially when it dies. During their life, intermediate-mass ($1M_\odot < M < 8M_\odot$) and massive stars ($M > 8M_\odot$) affect the interstellar medium through radiation, outflows, winds and supernova explosions. When they die, they expel a large fraction of their mass, enriching the interstellar medium with elements heavier than H and He. On the other hand, lower-mass objects, from Brown Dwarfs (BDs) ($0.013M_\odot < M < 0.075M_\odot$) to dim low-mass stars ($0.075M_\odot < M < 1M_\odot$), retain most of their masses over cosmological time scales. Consequently, the chemical evolution of galaxies is very sensitive to the IMF.

The importance of understanding the origin of the IMF and its apparent universality has therefore triggered much research on star formation, both theoretical and observational. The history of the subject began in 1955, when E. Salpeter published the first estimate of the IMF for stars in the solar-neighborhood ($d \lesssim 100$ pc) and found that it can be described by a power-law on a $\log N - \log M$ histogram with slope α=1.35 in the range $0.4M_\odot < M < 10M_\odot$ (Salpeter 1955). This result was then extended up to more massive stars ($M \simeq 20M_\odot$) (e.g. Massey 1998), while a significant flattening was found below $\sim 0.5M_\odot$ (Kroupa 2002).

Today the IMF has been estimated from low-mass BDs to very massive stars in a variety of systems. The regions that have been studied with direct star counts so far include the local field star population in our Galaxy and many star clusters and associations of all ages and metallicities in both our Galaxy and the

Magellanic Clouds. The sample ranges from present-day star-forming regions in small molecular clouds, to rich and dense massive star-clusters forming in giant clouds, up to ancient and metal-poor exotic stellar populations. This large body of direct evidence is consistent with the IMF being roughly the same for starbursts that have occurred under remarkably different circumstances and across the entire history of the Galaxy. Thus, the average IMF appears to be a universal function and can be approximately described by a power-law above $1\mathrm{M}_{\odot}$, having a slope between 1 and 1.6, which is in agreement with the Salpeter determination; below $1\mathrm{M}_{\odot}$, the IMF shows a flattening down to $0.1\mathrm{M}_{\odot}$ or lower (Kroupa 2002; Bastian et al. 2010).

Since at the moment there is no a priori reason to suppose that the IMF is a universal function, its apparent universality is a challenge for star formation theory; elementary considerations suggest in fact that the IMF should vary systematically with star-forming conditions, depending on the properties of the natal molecular cloud or of a nearby young stellar population (Elmegreen 1999).

Given the still large uncertainties on the IMF determination, the question whether the differences in the observed IMFs under different star-forming conditions are real and significant is still an open issue. The IMF is particularly controversial in the very-low mass and substellar regimes. Recent studies have provided more information about Very Low Mass Stars (VLMSs) and BDs, confirming that the IMFs remains approximately constant or shows a moderate decline in the BDs regime. Nevertheless, there is no systematic indication of such a turnover, and certain regions have been found where the IMF appears to rise below the sub-stellar limit (Bastian et al. 2010, and references therein).

If the shape of the IMF depends on the environment, it may offer vital insights into the physical processes that regulate the formation of stars and BDs and may also have strong implications for the choice of places in which to look for the most elusive BDs with mass comparable to those of giant planets.

The current differences in the sub-stellar IMFs may be ascribed to the following reasons:

- an incomplete census for sub-stellar objects, due to the fact that the surveys for such objects concentrate sharply in selected sky areas, in particular in the cores of star-forming regions;

- BDs may form only as unlucky members of small groups of stars, ejected by dynamical interactions before they can accrete to stellar masses (Reipurth & Clarke 2001). Hence, many sub-stellar objects might have escaped detection in the pencil-beam surveys in star-forming regions;

- alternatively, different processes (turbulent fragmentation, disk fragmentation, core collapse, see e.g. Whitworth et al. 2007, for a review) can produce different initial conditions for star and planet formation, and hence might lead to different mass spectra in different star-forming regions. Also, the radiation and winds from OB stars or supernova shock waves that may trigger star formation in OB associations may also have an important effect on mass accretion during the formation process. While in a T association a protostar may accumulate a significant fraction of mass, the mass accretion of a low-mass protostar in a region exposed to the winds of OB stars or supernova shock waves can be terminated abruptly because of the photo-evaporation of the circumstellar matter (Kroupa 2001, 2002; Robberto et al. 2004). Therefore, many low-mass protostars may not complete their accretion and hence can result as sub-stellar objects.

Spatially complete deep imaging surveys are then crucial in order to single out VLMSs and BDs with a minimum bias in the search strategy, and hence address problems like mass segregation in star-forming regions and the low end of the IMFs.

Wide-field imaging in the optical and especially in the infrared, as well as in the X-ray domain, are primary tools for the search of very low-mass Pre-Main Sequence (PMS) stars, young BDs and even giant free-floating planets. Moreover, one has to take into account that young stellar objects can be interacting with a circumstellar accretion disk. The presence of the disk is revealed by the excess emission in the near-infrared (Meyer et al. 1997; Hillenbrand et al. 1998; Cieza et al. 2005; Fischer et al. 2011), mid infrared (Persi et al. 2000) and far-infrared (Prusti et al. 1992), while the magnetically funneled accretion columns produce broadened emission lines (i.e. strong H_α emission, etc. Hartmann 2009). X-ray emission from low-mass PMS stars, on the other hand, is likely to be originated, as in the Sun, from their surface activity involving a dynamo generated magnetic field (Feigelson & Montmerle 1999) and may be therefore less sensitive to the presence of accretion.

In recent years it has been shown that young BDs are also X-ray emitters and may exhibit strong H_α emission (Jayawardhana 2010). The ubiquity of circumstellar disks across the full mass range hints to a common formation scenario for VLMSs and BDs. Therefore, all the phenomenological characteristics regarding PMS activity can be extrapolated, at a smaller scale, to the BDs regime.

The importance of the Orion Nebula Cluster

The IMF inferred for the local field stars is subject to significant uncertainty because it depends on the assumed evolutionary history of the local Galactic disk and on the assumed stellar lifetimes. In general, determining the IMF of a stellar population with mixed ages requires strong assumptions. Stellar masses cannot be measured directly in most cases, so the mass has to be deduced indirectly by measuring the star luminosity and the spectral type; mass measurements are then affected by the errors on the star distance and the accuracy of theoretical stellar models, which are rather uncertain particularly in the low-mass and substellar regimes (Baraffe et al. 2002).

In contrast, the IMF of homogeneous star clusters or associations can be derived with fewer assumptions and should be more reliable, since all of the stars in each cluster have roughly the same distance and age and, at least in the youngest clusters, all of the stars are still present (with a few possible exceptions for runaway stars) and can be directly counted as a function of mass without the need for evolutionary corrections. The best time to determine the IMF is then early in the life of a cluster or association, before high mass stars burn out and dynamical friction ejects the lower mass systems.

Another important issue is that the luminosity of PMS VLMSs and BDs is a decreasing function of age. Their bolometric luminosity during the gravo-thermal contraction phase evolves with time approximately as $t^{-1/2}$ (Black 1980; Burrows et al. 1995). Therefore, it may also be easier to detect VLMSs and BDs in star-forming regions, when they are very young. Thus, at ages of a few Myr, one can more readily reach masses below the hydrogen-burning limit. For example, at this age, a $0.075 M_{\odot}$ object (i.e. the high mass limit for a BD) is as luminous as a $0.35\ M_{\odot}$ mid-M spectral type star on the main sequence, according to the current evolutionary models.

The Orion Nebula (ON) (M42, NGC 1976) (Fig. 1.7) hosts the richest cluster of young ($\tau \simeq$1-2 Myr) PMS stars within 1 kpc of the Sun: the Orion Nebula Cluster (ONC) (see Muench et al. 2008; O'Dell et al. 2008, for recent reviews). The ON can be characterized as a bright blister of ionized gas on the surface of the Orion Molecular Cloud 1 (OMC-1). The rapid expansion of the HII region, powered by a small number of massive OB stars mostly clustered in the Trapezium multiplet (θ^1 Ori) (O'Dell et al. 2008, 2009), has exposed to our view the ONC, an extremely rich aggregate of PMS stars ranging from 45 $M_\odot$ to less than 0.02 $M_\odot$. A foreground veil of neutral gas, marginally optically-thick, passes through the nearest members of the ONC. The NW part of the nebula, designated M43 (NGC1982), is illuminated by NU Ori (Sp.Type BIV) with its own associated cluster. Two additional sites of embedded star formation are projected on the core region: 1) the cluster associated with the BN-KL infrared sources, $\sim 1'$ NW of the center; 2) the Orion-S sources, with numerous HH sources, $\sim 1'$ SW of the center. Both clusters are younger than the ONC, but the ONC is by far the richest, having bona-fide members located up to the edges of the nebula.

Because the ONC is one of the nearest massive star-forming regions to the Sun and the most populous young cluster within 1 kpc, it has been observed at virtually all wavelengths over the past several decades. However, only recently the increased sensitivities of the Near-Infrared (NIR) detectors on larger telescopes allowed us to begin to understand and characterize the extent of the ONC's young stellar and BD population, which, at $\sim$1–2 Myr, is just beginning to emerge from its giant molecular cloud OMC-1. The whole program was designed to study the ON in great detail. We take advantage of the fact that it is close (d$\sim$400 pc), lies well below the Galactic Plane (b=-19), and in an anti-center quadrant (l=209) with minimal foreground confusion. It lies on the front edge of the OMC-1 Giant Molecular Cloud, whose total extinction (up to A_V=50-100 on the main ridge) eliminates background confusion. The moderate foreground extinction ($A_V \lesssim 0.5$) allows detailed studies at visible and NIR wavelengths of individual stars. The richness of the stellar cluster (n$\sim$3500 stars) and its density ($\sim 2 \cdot 10^4$ stars pc^{-3} at the core, Hillenbrand & Carpenter 2000) make the ONC a unique target for wide-field imaging. In addition, a number of deep NIR surveys (Hillenbrand et al. 1998; Lucas & Roche 2000; Luhman et al. 2000; Muench et al. 2002) indicate that there are >200 PMS BDs, and perhaps tens of objects below the D-burning limit of 0.013 $M_\odot$, in the ONC core. Substellar objects are a thousand times brighter at an age of a few Myr than at an age of a few Gyr: this property, combined with the strategic projected position of the cluster in the sky, makes the ONC the ideal laboratory to study the low-mass end of the cluster IMF.

In the last decade, several studies have explored the ONC at substellar masses. Hillenbrand & Carpenter (2000) present the results of an H and K_S imaging survey of the inner $5' \times 5'$ region of the ONC. Observed magnitudes, colors, and star counts were used to constrain the shape of the ONC mass function across the hydrogen-burning limit down to 0.03 $M_\odot$. They find evidence in the $\log N - \log M$ mass function for a turnover above the hydrogen-burning limit, then a plateau into the substellar regime. A similar study by Muench et al. (2002) uses J, H and K_S imaging of the ONC to derive an IMF that rises to a broad primary peak at the lowest stellar masses between 0.3 $M_\odot$ and the hydrogen-burning limit before turning over and declining into the substellar regime. However, instead of a plateau through the lowest masses, they find evidence for a secondary peak between 0.03 $M_\odot$ and 0.02 $M_\odot$. Luhman et al. (2000) use H and K_S infrared imaging and limited ground-based spectroscopy to constrain the mass function and again find a peak just above the substellar regime but then a steady decline through the lowest mass objects.

Generally speaking, photometry alone is not sufficient for deriving stellar masses but, on the other hand, it is adequate in a statistical sense for estimating mass distributions given the right assumptions. This is a great advantage with respect to spectroscopy, as it allows to collect data for a large number of stars in a limited observational time. On the other hand, the position of a PMS star in the Color-Magnitude Diagram (CMD) is dependent on mass, age, extinction, and the possible presence of circumstellar activity (either accretion processes or the presence of a circumstellar disk). These characteristics affect the conversion of a star's magnitudes and colors into its stellar mass.

Specifically for the ONC, photometric observations are hampered by the brightness and non-uniformity of the nebular background. To overcome observational difficulties and theoretical uncertainties, the unique combination of sensitivity and spatial resolution offered by the Hubble Space Telescope (HST) has been exploited to obtain accurate photometry of the cluster, especially at substellar masses (HST Treasury program GO-10246). The HST survey has been complemented by ground-based observations, imaging the ON from the U-band to the K_S-band at La Silla and Cerro Tololo (CTIO) observatories. The ground-based observations, carried out in parallel on the same nights (but at a different epoch than the HST observations), complement the deep HST data which saturate at relatively low brightness levels. Their simultaneity makes the derived stellar colors largely immune to the uncertainties associated with photometry collected at different epochs.

Outline

In the following chapters we aim at the complete characterization of the ONC down to the BDs regime, using the ground-based NIR JHK_S photometric observations presented in Chapter 1. In particular, the main objective of the program is to derive the photometrically-determined IMF of the cluster. As discussed in Lada & Lada (2003), to achieve this goal one needs the intrinsic Luminosity Function (LF) of the cluster and the most appropriate Mass-Luminosity Relation (MLR). In order to derive the intrinsic LF, the first step is to correct the observed LF for galactic and extragalactic contamination. To this purpose, in Chapter 2 we extract a sample of bona-fide background stars from the catalog and analyze their projected spatial density and color excess to derive the extinction map of the OMC-1. We then combine this map with the galactic population model to derive a statistical estimate of the contaminant LF as seen through the bulk of the OMC-1, to be subtracted from the observed LF.

Another correction needed in order to derive the intrinsic LF is the removal of the NIR excess due to circumstellar disks. To achieve this goal, we first cross-match our NIR catalog with previous spectro-photometric optical observations, selecting a sample of ONC members with no evidence of flux excess due to accretion and/or circumstellar disks. Combining the observed colors of these stars with previous determinations of their $T_{\rm eff}$, we derive the empirical NIR isochrone of the ONC (Chapter 3).

With this empirical isochrone at hand, which is meant to closely reproduce the intrinsic colors of the ONC members, in Chapter 4 we analyze the amount NIR excess entering our observed photometry. In particular, we use the subsample of ONC members with spectral type to compare the expected colors of stars with the corresponding extinction-corrected colors. We thus derive the excess in the three JHK_S bands and we find that correlations between them are consistent with a circumstellar disk thermally radiating in the NIR.

Combining the previous results, in Chapter 5 we present a numerical method which simultaneously takes into account the effects of interstellar extinction and NIR excess, using the full set of observed JHK_S magnitudes. Our algorithm also statistically estimates the membership of each star in our catalog, based on the incidence of galactic contamination consistently with the extinction provided by the OMC-1. This allows us to statistically derive the intrinsic NIR LF of the ONC. We then combine the LF with the empirical isochrone, and we derive the complete IMF of the ONC down to the BDs domain.

Chapter 1

Observations and data reduction. The catalog.

1.1 ISPI observations

The Infrared Side Port Imager (ISPI) is the facility infrared camera at the CTIO Blanco 4 m telescope. ISPI uses a 2k×2k HgCdTe HAWAII-2 array, with reimaging optics providing a scale of $0.3''$/pixel corresponding to a $10'.25\times10'.25$ field of view. Our target area, about $30'\times40'$, covers the field imaged with the HST.

The observations were performed on the nights of 1 and 2 January 2005 (indicated hereafter as Night A and Night B respectively) in the J, H and K_S filters using the Double Correlated Sampling readout mode. The main filter parameters are listed in Table 1.1. The seeing was $\simeq 0''.7$ in most of the K_S-band images and occasionally worse on night B.

The survey area was divided into eleven fields (Fig. 1.1). The central position of each field, together with the airmass of the observations, is listed in Table 1.2. Each field was observed with an ABBA pattern. After pointing the telescope to the center of a field (A position) a 5 point dithering pattern was executed offsetting the telescope approximately by $\pm30''$ along the field diagonals. This first group of 5 dithered exposures was followed by a second group

Table 1.1: ISPI Broad Band Filters.

Filter	Central wavelength (μm)	$\Delta\lambda$ (80%) (μm)
J	1.250	1.176 - 1.322
H	1.635	1.500 - 1.770
K_S	2.150	1.992 - 2.300

Table 1.2: Log of the ISPI observations.

Field	Night	RA (2000.0)	DEC (2000.0)	Airmass
1	A	05:35:38.37	-5:12:50.7	1.144 - 1.291
2	A	05:34:59.63	-5:12:57.6	1.123 - 1.139
3	A	05:34:18.52	-5:12:59.6	1.123 - 1.139
4	A	05:35:37.05	-5:22:38.6	1.309 - 1.158
5	A	05:34:59.08	-5:22:28.3	1.319 - 1.938
6	A	05:34:17.98	-5:22:28.3	1.319 - 1.938
7	B	05:35:38.16	-5:33:03.8	1.218 - 1.410
8	B	05:34:59.82	-5:33:18.6	1.104 - 1.211
9	B	05:34:18.50	-5:33:21.4	1.104 - 1.211
10	B	05:35:37.48	-5:43:06.9	1.110 - 1.215
11	B	05:34:56.28	-5:43:09.2	1.110 - 1.215

of sky frames (B position) taken on a nearby field free, or nearly free, of diffuse nebular emission to extend the field coverage and monitor the flat-field response close in time to our observations. The sky-source sequence was then repeated back, completing the ABBA cycle. This provides a total of 10 frames of 30 s exposure for the common part of each field, totaling 300 s integration. Due to the high background, we split the K_S-band 30 s exposures in two consecutive 15 s exposures, maintaining the background well within the linear regime.

Each dithering sequence was repeated with a 3 s integration time. These short frames were coadded into another image of 30 s total integration time, which we used to extract the photometry of sources saturated in the longer exposures. Due to an error in our observing procedure, the J-band observations of field 3 were obtained only with 3 s exposures.

For absolute calibration we observed at various airmass the faint IR standard stars 9108, 9118 and 9133 of Persson et al. (1998). Unfortunately, on both nights the atmospheric transmission at IR wavelengths turned out to be unstable due to variations in the water vapor opacity, and we eventually derived the zero point calibration of our images through comparison with the extensive set of 2MASS data across our wide field area, as described in Sect. 1.2.2.

1.2 Data reduction

The first step in the data reduction was the correction for the intrinsic non-linearity of the detector, which we performed by applying the correction curve

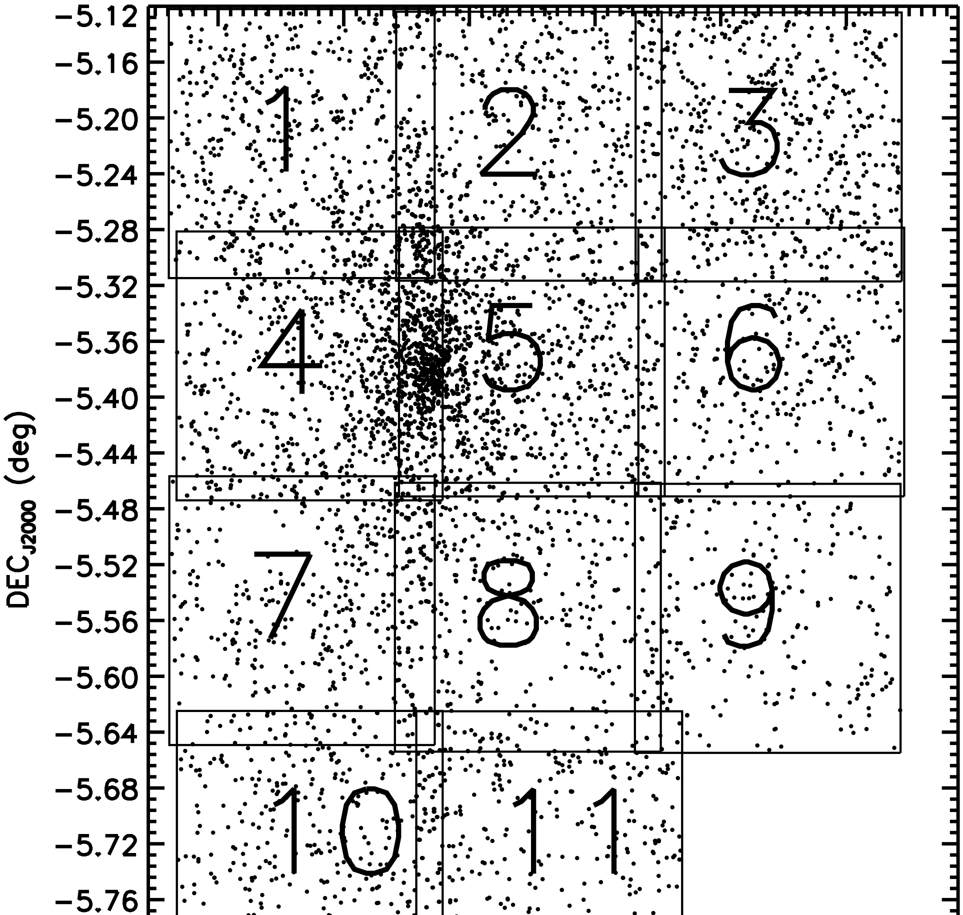

Figure 1.1: Position of the eleven ISPI fields, superimposed to the positions of the sources detected in our survey.

kindly provided by N. Van der Bliek[1]. We flat-fielded each image using dome flats and correct for residual color terms at low-spatial frequency using delta-flats derived from median averaged sky images. The dome flats were also used to flag bad pixels. The sky frames, properly filtered to remove spurious sources arising from the latent images of bright stars on the infrared detectors, were combined and subtracted from the science images.

Since ISPI exhibits significant field distortion, each science image had to be geometrically corrected before being combined in a dithering group. This required a first pass of aperture photometry with DAOPHOT, in order to extract a source catalog with well measured centroids and photometry (to disentangle the case of multiple candidates in the search radius). These sources were then cross-identified with the 2MASS catalog for astrometric reference, building an image distortion map relating their position on the original images to the actual position provided by 2MASS.

Due to the non-uniform distribution of sources, clustered at the center of the nebula, the accuracy of the distortion correction map varies across each field. Therefore, we combined the distortion maps relative to all images taken on the same night to derive, for each filter, a master distortion map. Each individual image was then warped using a 4th-order polynomial fit with coefficients derived from the corresponding distortion map.

Images belonging to the same dithered groups were then combined per integer pixels into single 2500×2500 images. The DAOPHOT source extraction was then repeated on these geometrically corrected images to produce a new source catalog from which we derived the final astrometric solution of each image by minimizing the residual shift and rotation with respect to the 2MASS positions. The average scatter between our coordinates and the corresponding 2MASS coordinates turns out to be about $0.15''$, i.e. half of a ISPI pixel. The same procedure has been adopted on the 3 s images.

In conclusion, for each field the final data consist of one combined image in each of the 3 filters (J, H, K_S) and exposure times (300 s and 30 s), with the exception of fields 4, 5, and 6, which have double this number of images, and field 3, which was not observed with deep J images.

---

[1] now also available on the ISPI web page: `http://www.ctio.noao.edu/instruments/ir_instruments/ispi/`

1.2.1 Instrumental magnitudes

The extraction of source photometry was performed on the final combined images, for both short and long exposure times. The Daophot FIND IDL procedure was used to extract an initial list of candidate sources, with rather loose detection thresholds and criteria to include the largest possible number of candidates. This initial list, counting more than 60,000 candidates, has been visually inspected on the original images to clean up artifacts and to preliminarily classify real sources as either point-like or extended. The list was then reduced to 7563 sources, divided between 6630 point-like and 933 diffuse.

For all sources we first derived an aperture magnitude by integrating the flux over a 5 pixel ($1.5''$) radius circular aperture, taking sky annuli typically between 10 and 15 pixels (3.0-$4.5''$); for 1416 bright sources, saturated in the 30 s images, we used the photometry extracted from the 3 s images.

We then performed Point Spread Function (PSF) photometry on all point-like sources. Due to the spatial variability of the PSF across the field of view of ISPI, present even after geometric correction, we divided each image in 9 parts (3×3 squares) allowing for some overlap between adjacent sub-images. The samples of stars in each sub-image, still relatively rich, had a more homogeneous PSF allowing us to reliably derive PSF magnitudes. We subtracted the PSFs and looked at the residual images searching for faint companion stars previously undetected. We found in this way 325 “hidden companions”. Finally, we performed a second pass of PSF photometry, first by removing from the list of stars used to derive the PSF those having a faint companion, and then deriving also the photometry of the newly detected faint companions.

1.2.2 Absolute calibration

As mentioned in Sect. 1.1, the IR photometric quality of our nights turned out to be unsatisfactory due to hygrometric variability. We therefore calibrated our ISPI instrumental magnitudes directly to the 2MASS photometric system. The 2MASS catalog provides absolute photometry in the J (1.25μm), H (1.65μm), and K_S (2.17μm) bands to a limiting magnitude of 15.8, 15.1, and 14.3, respectively, with Signal-to-Noise Ratio (SNR) greater than 10.

To estimate the color terms and zero points of each image, we first scaled the instrumental PSF magnitudes of point sources measured in the short 30 s images to the long 300 s images, chosen as the reference time because of their source richness. To minimize systematic effects due do atmospheric variations, we did not simply add the nominal Δmag=2.5 factor but compared the instrumental magnitudes of well measured stars to derive for each field and filter a mean magnitude offset $\overline{\Delta mag}$ between the short and long images. By homogenizing in this way the zero points of the short and long images, we add a small uncertainty to the photometric errors of the bright stars measured in the short exposures.

For each bandpass λ we then evaluated the relations

$$mag_{\rm 2MASS}(\lambda) - mag_{\rm ISPI}(\lambda) = ZP_\lambda + \epsilon_{\lambda_1,\lambda_2} \cdot c_{\rm ISPI}(\lambda_1, \lambda_2),$$

where $mag_{\rm 2MASS}$ is the magnitudes in the 2MASS photometric system, $mag_{\rm ISPI}$ is the ISPI instrumental magnitude, the intercept ZP_λ is the zero point in a given bandpass, the slope $\epsilon_{\lambda_1,\lambda_2}$ is a color coefficient between the wavelengths λ_1 and λ_2 and $c_{\rm ISPI}$ is the corresponding observed ISPI color. We found the strongest statistical correlation in the combination:

$$H_{\rm 2MASS} - H_{\rm ISPI} = ZP_H + \epsilon_{JK} \cdot (J-K)_{\rm ISPI}.$$

For each field, we derived the linear fit parameters ZP_H and ϵ_{JK} using an iterative procedure to rejects spurious outliers and all sources with errors greater than 0.1^m in the 2MASS catalog and 0.05^m in our input catalog. As shown in Table 1.3, the color coefficient ϵ_{JK} varies slightly from field to field during each night, whereas the zeropoint ZP_λ shows an increase towards the middle of the night (observation were scheduled with fields 4 and 10 transiting at the meridian, in the two nights).

For the J and K_S bands, we derived the zero-points and the color terms from a linear fit to the color relations

$$(J-H)_{\rm 2MASS} = ZP_{JH} + \epsilon_{JH} \cdot (J-H)_{\rm ISPI},$$
$$(H-K_S)_{\rm 2MASS} = ZP_{HK} + \epsilon_{HK} \cdot (H-K_S)_{\rm ISPI}.$$

This allowed us to derive magnitudes calibrated in the 2MASS system for all sources with ISPI JHK instrumental photometry. In Fig. 1.2 we show a comparison between the magnitudes reported in the 2MASS catalog and our calibrated magnitudes. The plots show the lack of systematic differences, besides the random errors that we attribute to photometric errors or stellar variability.

For sources lacking one or two magnitudes (typically either J or both J and H), we assumed a linear relation of this type

$$mag_{\rm 2MASS}(\lambda) = \alpha \times mag_{\rm ISPI}(\lambda) + \beta$$

Table 1.3: Best estimate for calibration coefficients

Field	Z_H	σ_{Z_H}	ϵ_{JK}	$\sigma_{\epsilon_{JK}}$
1	1.09	0.01	-0.010	0.008
2	1.07	0.01	0.001	0.007
3^a	1.08	0.04	0.00	0.02
4	1.13	0.01	-0.022	0.006
5	1.11	0.01	-0.023	0.007
6	1.03	0.02	-0.05	0.02
7	0.93	0.02	0.00	0.01
8	0.93	0.01	-0.023	0.008
9	0.95	0.01	-0.02	0.01
10	1.09	0.02	-0.06	0.01
11	1.07	0.02	-0.02	0.01

Notes. $^{(a)}$ Parameters for field 3 are computed using non-normalized *J*-band magnitudes.

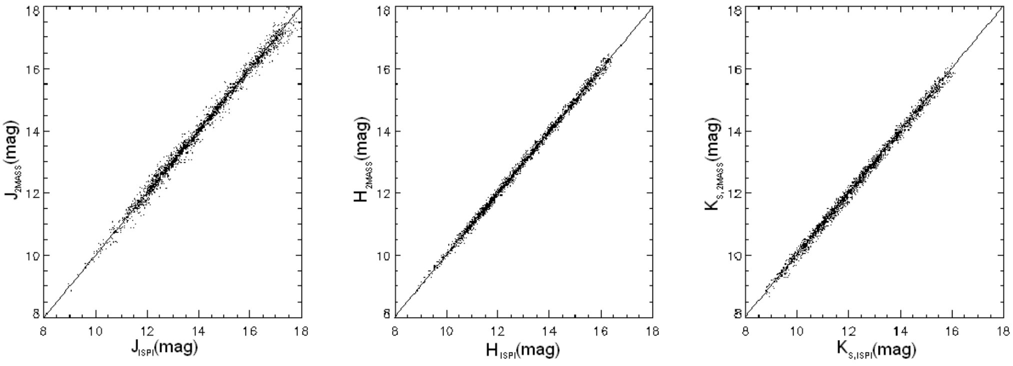

Figure 1.2: Comparison between 2MASS magnitudes and ISPI calibrated magnitudes.

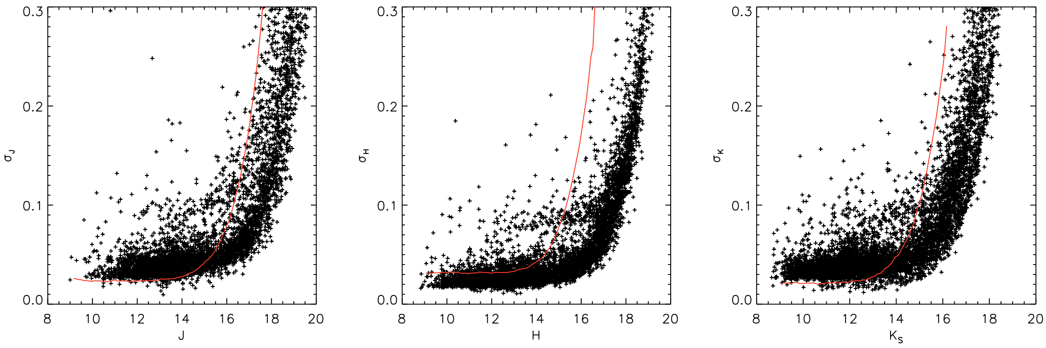

Figure 1.3: PSF photometric error as a function of magnitude for our point-like sources. The solid red line indicates the locus of the average relation for the 2MASS sources falling in the ISPI field.

deriving α and β, for each bandpass and field, from the sample of calibrated sources. The parameter α provides a magnitude-dependent correction to the zero point β, which is appropriate since fainter sources have, on average, redder colors. Using these coefficients we calibrated the magnitudes, with the relative uncertainties, of all remaining sources.

Figure 1.3 shows the photometric errors plotted as a function of magnitude for all point-like sources. The multiple threads in the distribution of the photometric errors are due either to the superposition of deep and short exposures (bright stars, measured in short 3 s exposures, turn out to have relatively larger errors) or to the sources measured, with higher photometric errors, in the crowded central part of the cluster. For comparison we also plot the average mag vs. Δmag relation for the 2MASS sources falling in our field.

1.3 Completeness

To determine the completeness of our photometric catalog, we used an artificial star experiment. For each field and filter, we averaged the 9 PSFs created for photometric extraction (Sect. 1.2.1) into a common reference PSF valid for the full image. We scaled the reference PSF in steps of 0.1 mag covering the entire magnitude range measured across each field and injected each scaled PSF at a random position in the image, with the only caveat of leaving enough distance from the border to allow for a meaningful measure. We assumed as a detection criterion a photometric error less than 0.3 mag and less than 0.5 mag difference between the injected and recovered magnitude, making also sure that the stars recovered by the code were the artificial ones and not previously known real stars. The completeness was calculated as the fraction of successful detection after 10000 iterations of the process, for each magnitude bin.

It turns out that the completeness (and the sensitivity) of our survey is significantly affected by the nebular brightness. We have therefore defined three concentric regions (Fig. 1.4) at increasing distance from Θ^1OriC (RA (2000.0)=05^h 35^m 16.46^s, DEC (2000.0)=-05° 23′23.″18). The limiting radii, respectively 6.′7, 14.′3 and 27.′2 (corresponding to projected distances of 0.81, 1.72 and 3.27 pc at a distance of 414 pc (Menten et al. 2007)) have been set in such a way that the three regions contain the same number of point-like sources. In order to avoid significant contamination from the M43 cluster, we neglect in our analysis a circle with a 5′radius centered on NU Ori (RA(2000.0)=$05^h35^m31.37^s$, DEC(2000.0)=-05° 16′02.″6) (see Fig. 1.4).

The results of our simulations are shown in Fig. 1.6. For each filter, the completeness estimated in the outer region is slightly, but systematically, larger than that in the intermediate region, which in turn is much larger than in the bright inner region, the most heavily affected by crowding and diffuse emission, where our sensitivity begins to drop at HK_S ∼14 mag. A comparison with Hillenbrand & Carpenter (2000) and Muench et al. (2002), who surveyed the inner part of the cluster (5′×5′ and 6′×6′ fields, respectively) deriving HK photometry down to our photometric limit (K_S∼18 mag), shows that we detect as point sources more than 90% of their sources (648/706 in the H-band and 657/698 in the K_S-band for Hillenbrand & Carpenter (2000) and 601/662(H) and 665/714(K_S) for Muench et al. (2002)). Figure 1.5, where we overplot the LFs obtained by Hillenbrand & Carpenter (2000) and Muench et al. (2002) (dashed lines) to our observed LFs (gray area) constructed for their same regions, confirms that the missing sources are generally fainter than $HK_S \simeq 14$ mag (the missing bright sources, detected but not measured by ISPI due to saturation, are not relevant here). If we apply to our H and K_S LFs the appropriate completeness corrections, estimated by repeating the artificial star experiment on the same fields of Hillenbrand & Carpenter (2000) and Muench et al. (2002), our LFs become consistent with theirs, with the exception of the secondary peak at $K_S \simeq 15.5$ mag discussed by Muench et al. (2002). In Sect. 1.5.3 we will apply the completeness corrections to the measured counts, when we will compare the LFs at various distances from the cluster center.

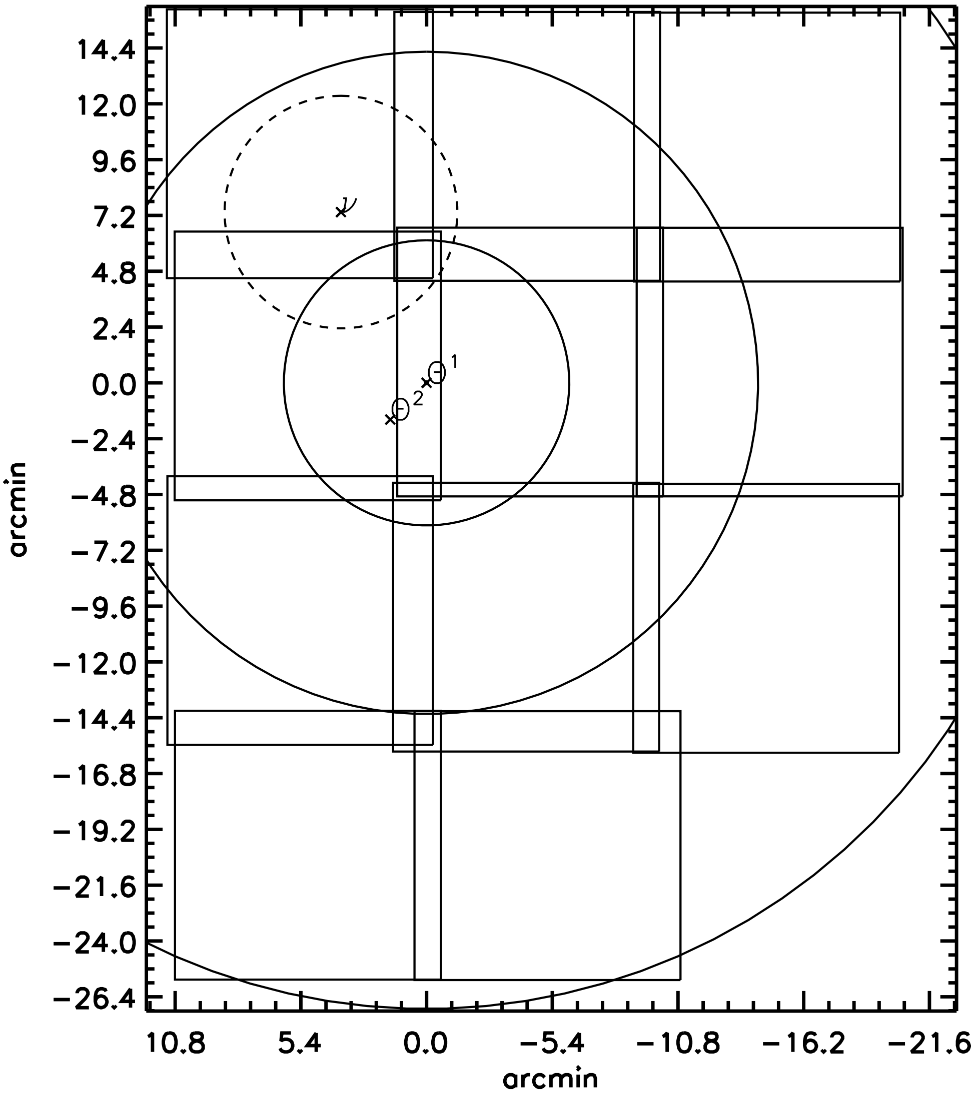

Figure 1.4: Projected regions identified in our surveyed area. The solid circles define the three radial areas containing an equal number of point-like sources, with radii of 6.7′, 14.3′ and 27.2′ respectively. The dashed circle indicates the exclusion field centered around NU Ori. The positions of Θ^1OriC, Θ^2 Ori and NU Ori are also indicated, together with our original field positions. The axes show the angular offsets from Θ^1OriC (RA (2000.0)=$05^h\ 35^m\ 16.46^s$, DEC (2000.0)=-05° 23′23.″18).

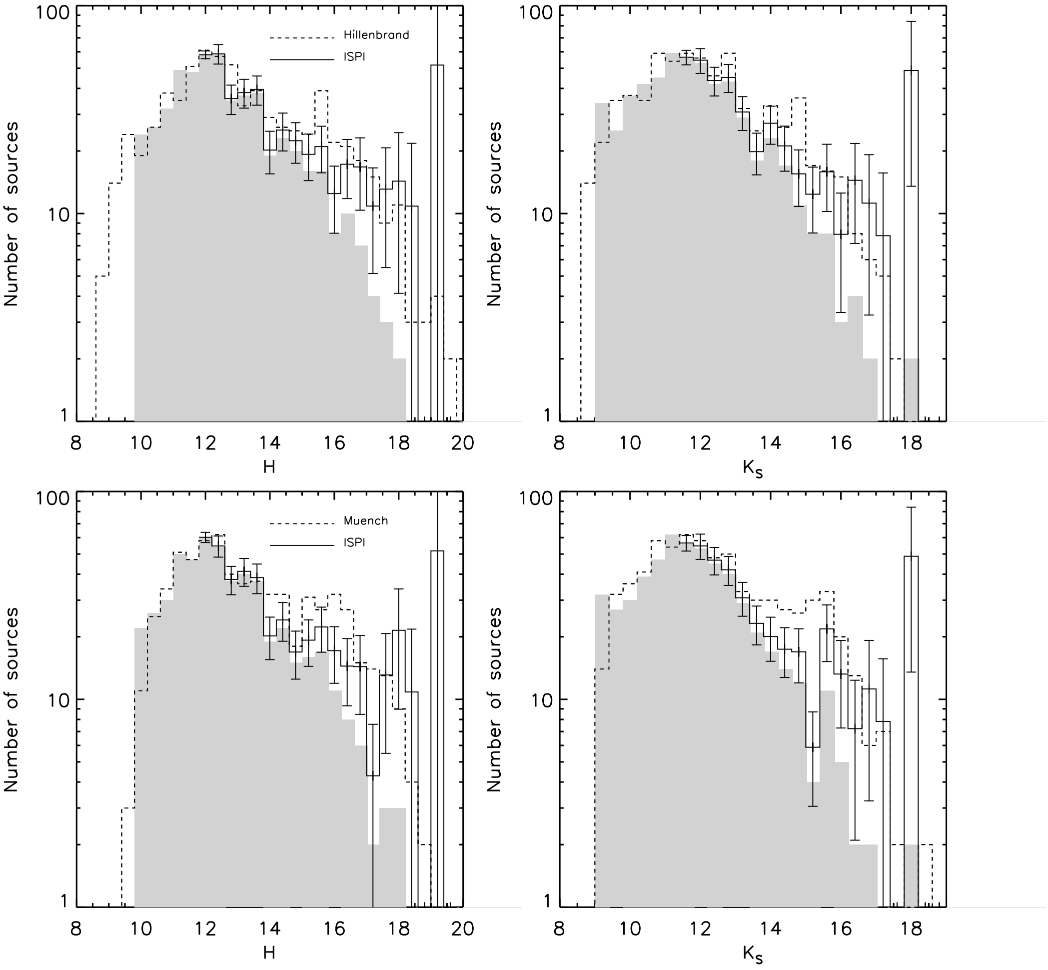

Figure 1.5: Dashed lines: *H* and K_S luminosity functions for the Hillenbrand & Carpenter (2000) (upper panels) and Muench et al. (2002) (bottom panels) catalogs; gray area: luminosity functions for the same filter and fields from the ISPI observations (point sources only); solid line: ISPI luminosity functions corrected for completeness. The error bars have been obtained by adding quadratically the statistical (poissonian) uncertainty on the measured counts to the completeness correction error derived from the Monte Carlo simulations.

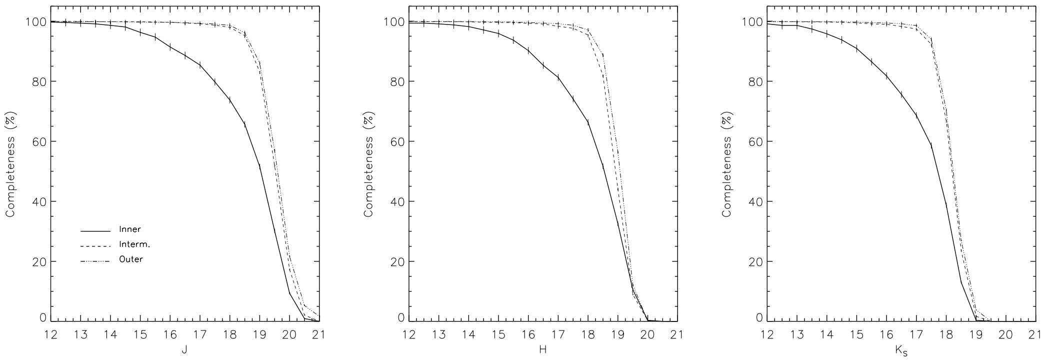

Figure 1.6: Completeness levels for the *J* (left), *H* (center) and K_S (right) bands derived from the artificial star experiment. Each plot shows the results for the 3 radial regions.

1.4 Results

Our final photometric catalog contains 7759 sources. Having visually inspected all sources, we find that 6630 can be classified as point-like sources and 933 as diffuse objects. The other 174 sources, typically brighter than $K_S \simeq 10$, turned out to be saturated even in our short 3 s images. We included them in our catalog, adopting the photometry and coordinates reported by 2MASS. We also found that the 2MASS photometric catalog misses 22 sources in the Trapezium region clearly visible in the 2MASS images and saturated even in our short exposures. We have added their JHK_S photometry using the Muench et al. (2002) photometry.

In Table 1.4 we summarize the number of sources measured in different combination of filters, exposure times, and morphological types. The source catalog is available at Centre de Données astronomiques de Strasbourg (CDS).

Figure 1.7 shows a JHK_S color composite of our imaged field. The image, produced by the graphic staff of the Space Telescope Science Institute, has been artificially enhanced to reduce the original dynamic range and more clearly reveal the inner part of the cluster.

1.5 Analysis of the catalog

1.5.1 Two-color diagrams

In Fig. 1.8a we show the NIR *J-H* versus *H-*K_S Two-Color Diagram (2CD) for 3866 sources. Following Lee et al. (2005), we overplot the intrinsic colors of

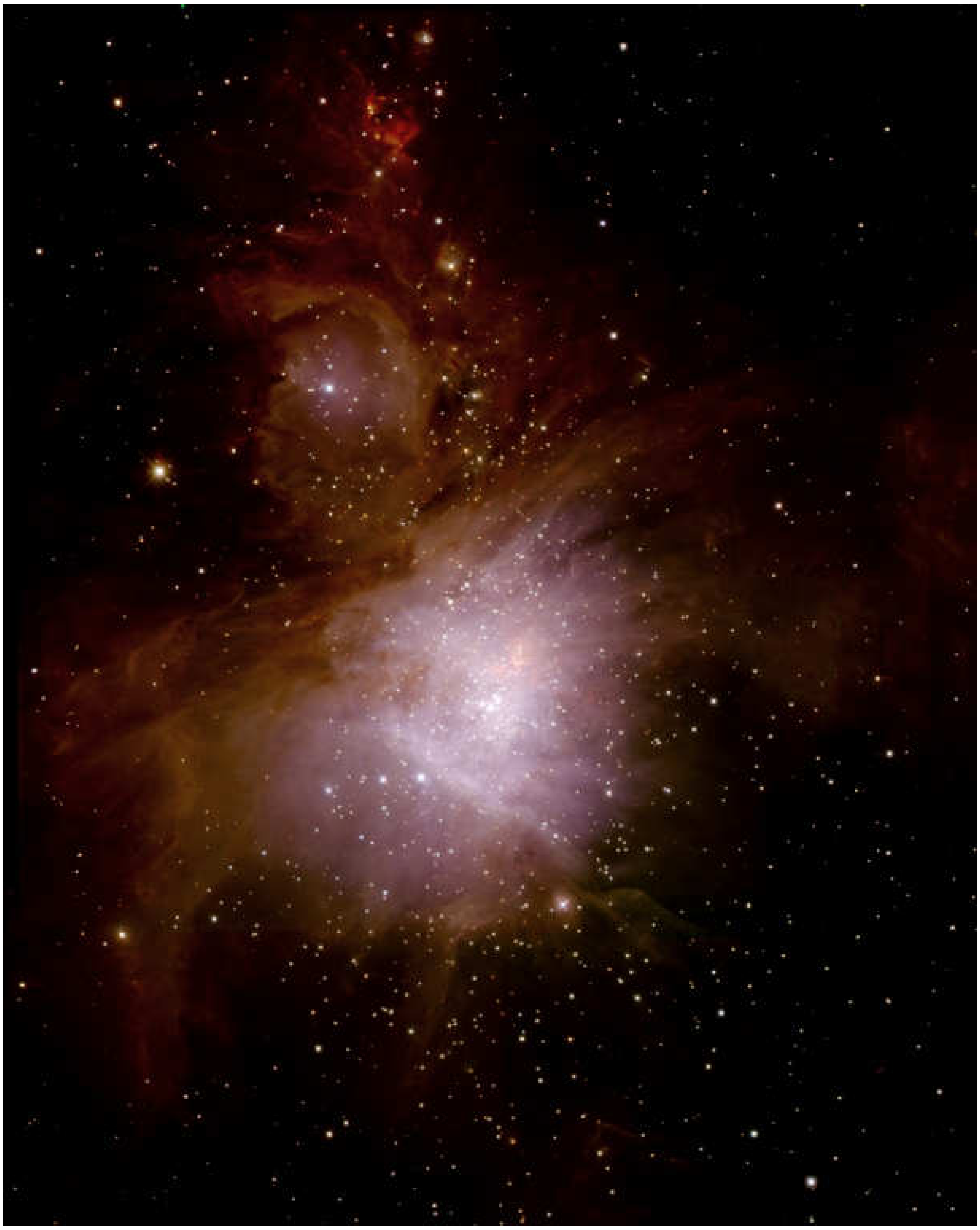

Figure 1.7: NIR color composite mosaic of the ON from our ISPI images. The image has been digitally enhanced to improve the visibility of the stellar sources in the central region. The RGB colors code the K_S, H and J bands, respectively.

Table 1.4: Source Summary.

Source	Number of stars
ISPI detected in *J*-, *H*- and K_S-bands	4851
ISPI detected in *J*- and *H*-bands, not in K_S-band	92
ISPI detected in *H*- and K_S-bands, not in *J*-band	1096
ISPI detected in *J*- and K_S-bands, not in *H*-band	85
ISPI detected only in *J*-band	175
ISPI detected only in *H*-band	80
ISPI detected only in K_S-band	251
ISPI diffuse	933
ISPI Total	7563
Extracted from the 2MASS catalog	174
Extracted from the Muench et al. (2002) catalog	22
Grand Total	7759
ISPI detected in 30 s images	6147
ISPI detected in 3 s images	1416
ISPI first run detection	6305
ISPI hidden companions	325
ISPI diffuse	933

the main-sequence stars and giant branch, together with the locus of Classical T Tauri Stars (CTTSs) surrounded by circumstellar disks (Meyer et al. 1997), given by the relation $(J\text{-}H)\text{-}0.630(H\text{-}K_S)\text{-}0.497=0$ in the 2MASS photometric system. We also plot the interstellar reddening vector of Cardelli et al. (1989), given by the relation $E(J\text{-}H)/E(H\text{-}K_S)=1.83$ in the 2MASS photometric system. Accounting for extinction, the locus of the CTTSs lies between the two parallel dotted lines defined by the equations $(J\text{-}H)\text{-}1.83(H\text{-}K_S)+0.098=0$ and $(J\text{-}H)\text{-}1.83(H\text{-}K_S)+0.50=0$.

For 45.2% (1853/4103) of the sources, the NIR colors are consistent with those of stellar dwarfs (luminosity class V), giants (luminosity class III) or CTTSs reddened by various amounts of foreground extinction. For 11.4% (466/4103) of the sources the NIR excess is compatible only with the reddened CTTSs, whereas only 0.8% (35/4103) of the sources show NIR excess significantly greater than those of CTTSs, indicative of strong K_S-band excess.

To assess how the observed reddening and color excess vary with the distance from the center of the cluster, we consider the so-called Hess diagrams (i.e. the density distribution diagrams) for the three radial regions. The inner field (Fig. 1.8b) shows a peak well detached from the main sequence, with isodensity contours elongated in a direction parallel to the CTTSs locus, together

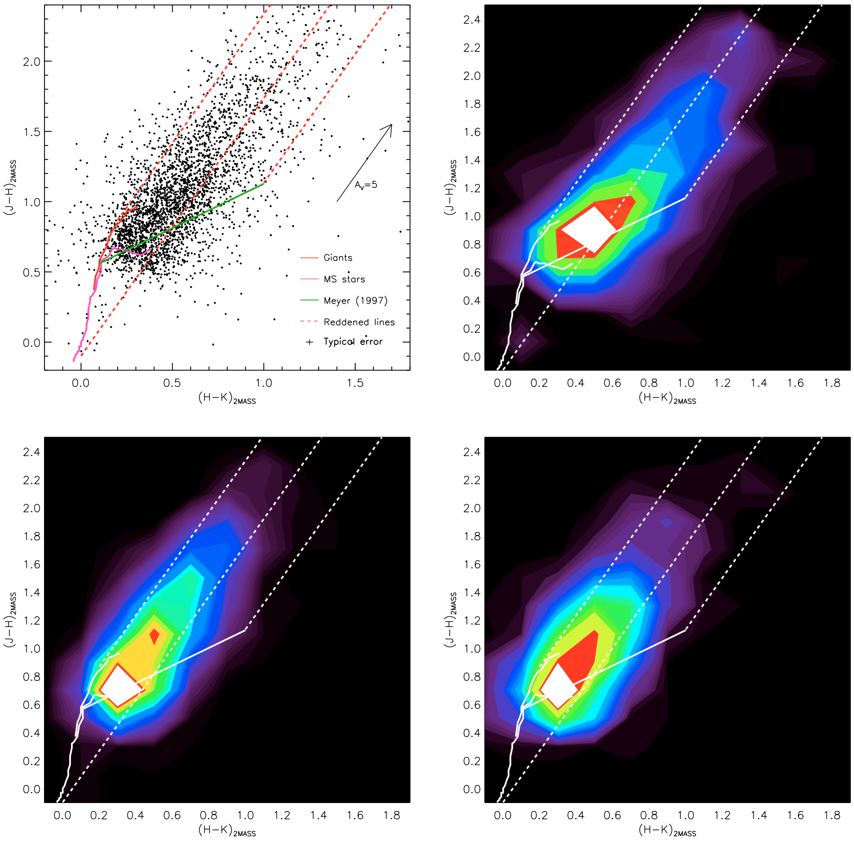

Figure 1.8: *a) top-left panel*: NIR 2CD diagrams for selected point-like sources in our catalog detected in all 3 bands (see text for the selection criteria). Also shown are the main-sequence (magenta solid line), the giant-branch (red solid line) sequence and the CTTSs locus by Meyer et al. (1997) (green solid line). The dotted lines are parallel to the standard reddening vector. *b) (top-right panel)* - Hess diagrams of the color-color diagram relative to the inner region. *c) bottom-left panel*: Similar to panel *b)*, for the median region. *d) bottom-right panel*: Similar to panel *b)* for the outer region.

with a long tail of stars with high reddening. The Hess diagram for the intermediate region (Fig. 1.8c) shows a main peak much closer to the locus of dwarf stars, together with a secondary maximum at higher extinction. The intermediate contour levels (e.g. the green area) are now elongated along the range of reddened main sequence stars.

Finally, the Hess diagram for the outer region (Fig. 1.8d) shows again a strong peak compatible with dwarf stars affected by a small amount of extinction, whereas the low contour levels appear less pronounced than in the two other regions and well within the limits of reddened main sequence or giant stars.

Overall, the three 2CDs can be interpreted as follows: 1) the inner Trapezium region is mostly populated by young stars with NIR excesses typical of CTTSs. They have generally relatively modest amounts of extinction, which is compatible with the fact that the ionizing radiation from the Trapezium stars has cleared the molecular cloud and exposed them to our view; 2) the intermediate region contains a relatively larger number of heavily reddened sources. They are seen through denser parts of the OMC-1, not yet reached by the expansion of the ionized cavity; 3) the outer regions mostly contain background objects seen trough the low opacity layers at the edges of the main OMC-1 ridge, which crosses the ONC approximately in north-south direction (Goldsmith et al. 1997).

1.5.2 Color-magnitude diagrams

In Fig. 1.9 we present the (H, J-H) and (K_S, H-K_S) CMD still for the same sample. Together with our data, we plot the 1 Myr isochrone of Chabrier et al. (2000), which covers the range $0.001\ M_\odot < M < 0.1\ M_\odot$ and is tailored to model substellar and planetary mass objects in the limit of high opacity photospheres. We also plot the 1 Myr isochrone of Siess et al. (2000) ranging from 0.1 $M_\odot$ to 7 $M_\odot$, well-suited for stellar sources. Both isochrones have been converted to the 2MASS photometric system using the transformations of Carpenter (2001). The offset between the two isochrones can be regarded as a graphic representation of the uncertainties in theoretical models. An $A_V = 10$ reddening vector is also indicated, as well as the reddening lines starting from the isochrones in correspondence of a 1 $M_\odot$ object (J=10.50, H=9.88 and K_S=9.76 at 414 pc in the 1 Myr `Siess00` isochrone), a $M = 0.075\ M_\odot$ object at the

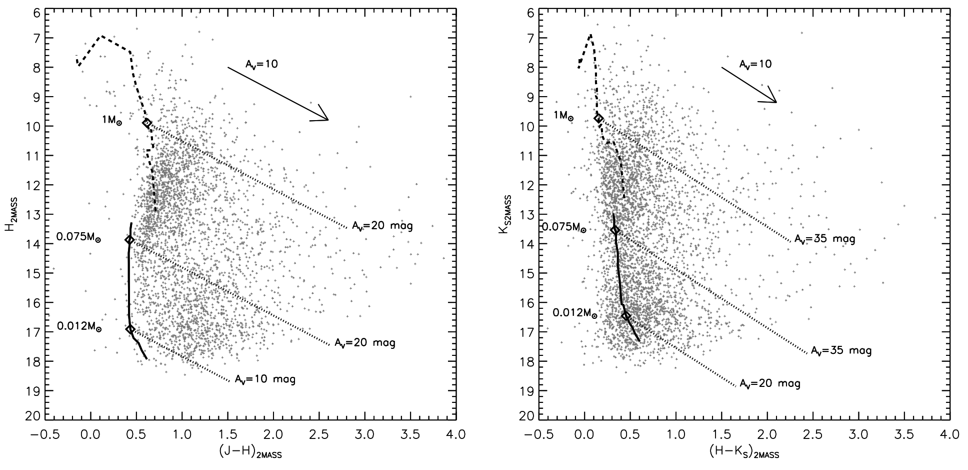

Figure 1.9: NIR CMDs for selected point sources in our catalog detected in all 3 bands, with 1 Myr isochrones, assuming a distance d = 414 pc (DM = 8.01). To derive these isochrones, we used Chabrier et al. (2000) combined to the Siess et al. (2000) model, as discussed in Sect. 1.5.2. The A_V=10 mag reddening vector is also shown. The diamond symbols represent the positions of a $M = 0.012\ M_\odot$ (deuterium burning limit) object, a $M = 0.075\ M_\odot$ (hydrogen burning limit) object and a $M = 1\ M_\odot$ star from bottom to top respectively.

hydrogen-burning limit mass (J=14.29, H=13.86 and K_S=13.56 at 414 pc in the 1 Myr `Chabrier00` isochrone) and a $M = 0.012\ M_\odot$ substellar object at the deuterium-burning limit mass (J=17.33, H=16.90 and K_S=16.48 at 414 pc in the 1 Myr `CBAH00` isochrone). For this distance and isochrone, our survey is therefore sensitive to stellar sources down to $A_V \simeq 60$, BDs down to $A_V \simeq 40$, and planetary mass objects down to $A_V \simeq 15$.

Almost all data points lie to the right of the isochrones and are therefore compatible with reddened 1 Myr old sources (as well as heavily reddened field objects). If we discard the blue sources with J-H<0.3, typically affected by large measurement errors, we find that the reddening lines identify 2246 sources in the region of reddened stellar photospheres, 1298 sources in the region of extincted BDs and 142 sources in the region of reddened planetary mass objects. In the (K_S, H-K_S) color-magnitude diagrams these values are 2134, 1145, and 421, respectively.

Splitting the cluster in the same three regions of Fig. 1.4, we obtain the CMDs presented in Fig. 1.10. From top to bottom, Fig. 1.10 shows the (H, J-H) (left column) and (K_S, H-K_S) CMDs for the inner, median and outer regions respectively. Consistent with what was found analyzing the 2CDs, the inner and outer regions appear dominated by two different populations. The top diagrams clearly reveal the location of the ONC: an ensemble of stellar sources with modest amounts of foreground extinction. The bottom diagrams are dominated by fainter sources (of course, for background stars the 1 Myr isochrone at 414 pc does not apply), whereas the intermediate region contains a mix of both populations. A careful look at the diagrams show that the peak corresponding to the ONC drifts down (i.e., to lower masses) and left (to lower extinction values) moving from the inner to the outer regions. The shift to lower masses represents an overabundance of higher mass sources at the center of the cluster, in agreement with the evidence for mass segregation found by Hillenbrand & Hartmann (1998). The redder colors of the cluster members in the central field may be due to the fact that they are, on average, either more embedded in the OMC-1 or subject to higher circumstellar extinction from their warped or flared circumstellar disks, or a combination of the two. In any case, these effects seem to point to the central cluster as the region where star formation is more recent (or even still ongoing, e.g. the sources in BN and Orion South). One could therefore coherently deduce a scenario in which low mass stars started to form first in the outer regions, whereas star formation in the inner part followed somewhat later with a relatively higher fraction of massive stars. Such an evolutionary sequence of events could indicate that mass segregation is primordial instead of temporary due to the random motions of massive stars, as recently suggested by Xin-yue et al. (2009).

1.5.3 Luminosity Functions

We conclude our analysis of the catalog showing the J, H and K_S-band LFs for all point-like sources. Once again, we remove stars less than $5'$ projected distance from NU Ori and divide the remaining sample in three groups according to the distance criteria adopted in the previous sections. Rather than assuming a certain completeness limit, we fully apply our completeness corrections, derived in Sect. 1.3, to the source counts measured in the various regions.

The histograms for the inner region (Fig. 1.11, thick solid line) show a broad peak at $J \simeq 13$, $H \simeq 12$ and $K_S \simeq 12$, corresponding to an M6 star (0.175 $M_\odot$) at 1 Myr, according to the Siess et al. (2000) model with zero reddening. The peak shows an abrupt drop at about $JH \simeq 14$ and $K_S \simeq 13$, approximately by a factor $\simeq 2$, which is fully consistent with the previous NIR studies of the ONC,

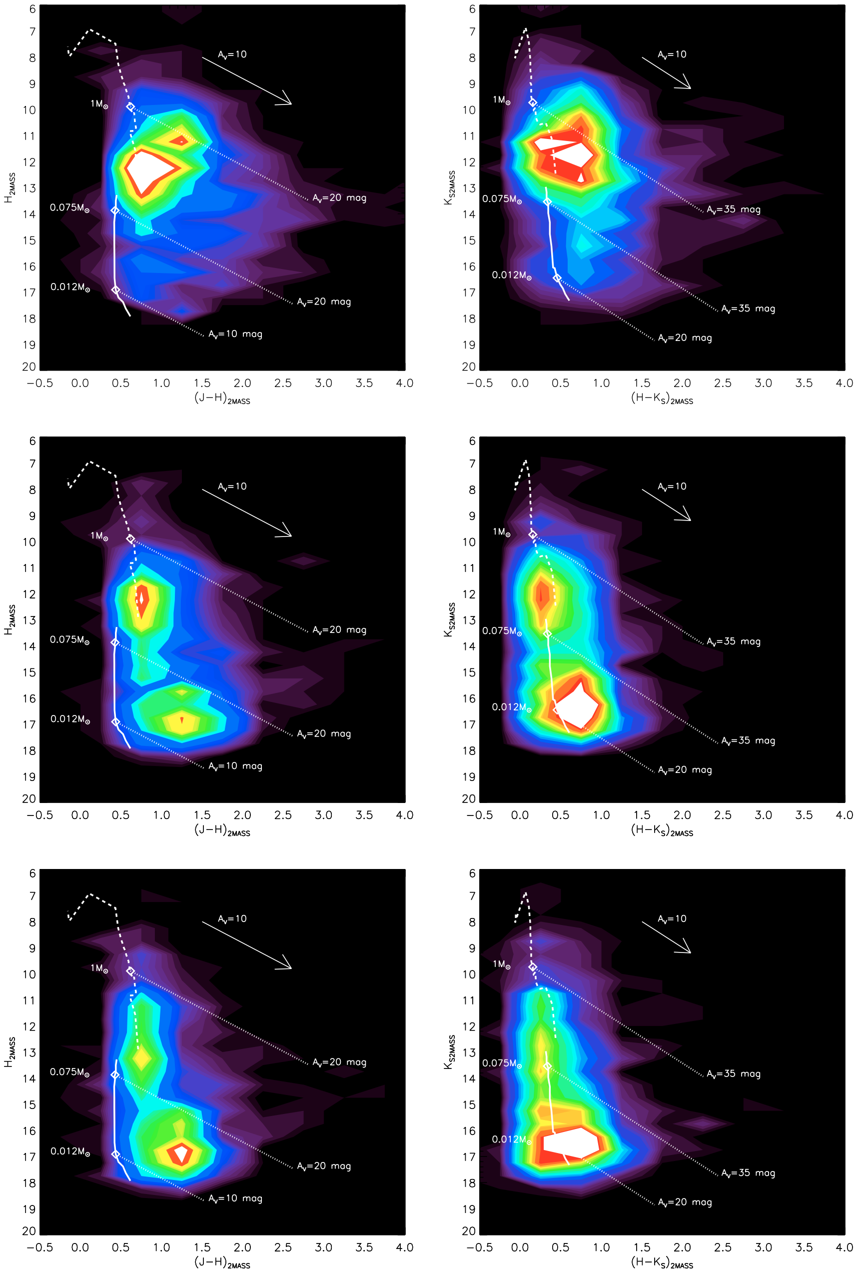

Figure 1.10: Hess format for the *J*,*J*-*H* (left panels) and K_S,*H*-K_S(right panels) CMDs. Line styles and symbols are the same as in Fig. 1.9. From top to bottom, the diagrams for the inner (r<6.7′), medium (6.7′<r<14.3′) and outer (14.3′<r<27.2′) regions are shown.

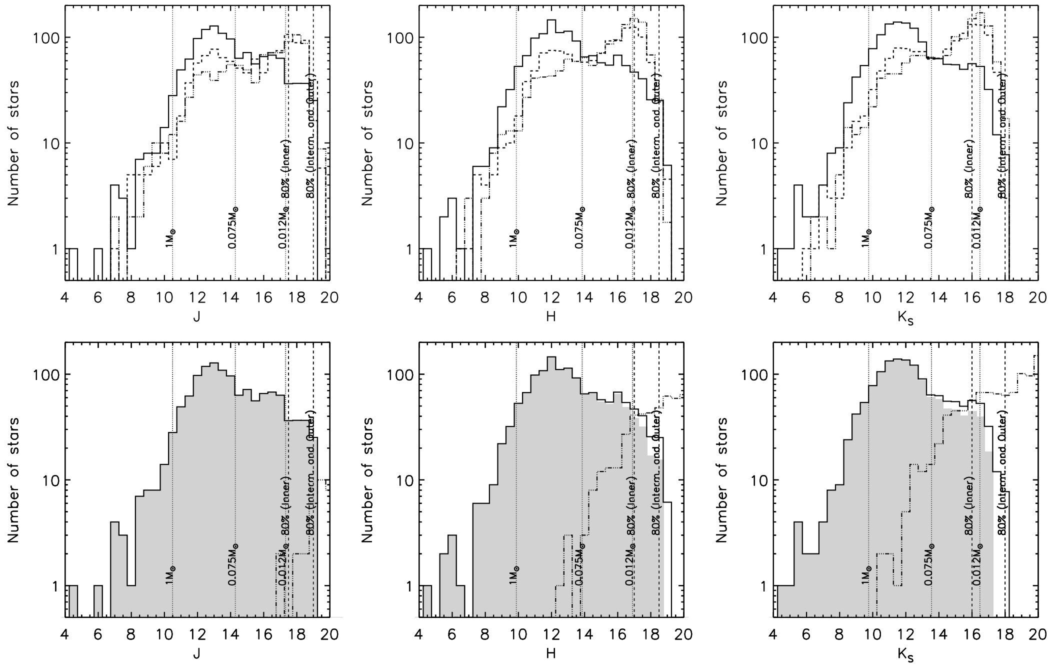

Figure 1.11: *Top panels*: *J*-band (*left*), *H*-band (*center*) and K_S-band (*right*) LFs for the ONC, corrected for completeness. The solid line is relative to the inner region, the dashed line to the intermediate region and the dotted-dashed lines to the outer region. *Bottom panels*: for each bandpass, LFs of the inner region (gray area), of the outer region shifted by $A_V = 33$ mag of extinction (dot-dashed line), and difference of the two (solid line). In each plot, we indicate with vertical lines the magnitudes corresponding to stars 1 Myr old at 414 pc with 1 $M_\odot$, 0.075 $M_\odot$ and 0.012 $M_\odot$ respectively, without interstellar reddening. The vertical dashed line stands for the 80% sensitivity level in the outer region.

e.g. Fig. 5 of Hillenbrand & Carpenter (2000). On the other hand, the luminosity functions corrected for completeness remains remarkably flat across the substellar region down to our sensitivity limit. This is not what has been found by other authors who concentrated on the innermost area. We remark that our completeness correction has the largest effect in the inner region, the one more affected by crowding and by the brightness of the nebular background. On the other hand, we have seen that our completeness correction fails to reproduce the $K_S \simeq 14$ secondary peak of Muench et al. (2002), and for this reason can hardly be suspected of providing an artificial overcorrection in the central area.

Moving from the inner to the outer parts of our survey area, the main peak in the LFs becomes less prominent in the median region and eventually disappears in the outer regions giving to the LFs an increasing monotonic slope.

If we compare our K_S-band LF for the outer cluster with the K-band LF of the off-cluster control field presented by Muench et al. (2002) (Fig. 3a of their paper), which shows no stars brighter than $K \simeq 12$, we see that our outer field still contains a fraction of sources belonging to the cluster or, more in general, associated to the recent star formation events in the Orion region (i.e. possible foreground members of the Orion OB1 association). This is in agreement with what we found in the previous section discussing the CMDs, not by chance since the LF represents the projection on the vertical axis of the color–magnitude plot.

The flattening of the substellar LFs in the inner region may be due to field star contamination. To address this possibility, we can use our outer field as a control field, knowing that it will probably provide an overestimate of the contribution of non-cluster sources and therefore, after subtraction, a lower limit to the cluster LF. This for two main reasons: first, we have seen that our outer field still contains a fraction of cluster-related sources and, second, background sources should be more easily observed in the outer field rather than in the central region due to the larger background extinction caused by the underlying OMC-1, which has the ridge of highest density crossing the cluster core nearly in a north-south direction (see e.g. the extinction map obtained from the $C^{18}O$ column density data of Goldsmith et al. (1997) presented in Fig. 2 in Hillenbrand & Carpenter (2000), or the extinction map of the OMC-1 we derive in Chapter 2). Figure 1.11 (bottom, gray area) shows the LFs corrected in this way, having properly normalized the source densities to the same surface area. There is a clear reduction of source density in the substellar regime and the main peak becomes more prominent, but the substellar LFs seem to remain flat or show, at best, a very modest negative slope.

Alternatively, it is possible to account for the higher background extinction beyond the central field, and therefore remove at least some of the systematic bias introduced by using the outer field, by shifting the outer LFs, for each filter, by magnitude values compatible with the interstellar reddening law of Cardelli et al. (1989). This because with a proper, wavelength dependent, change of zero points one can use the outer field counts to reproduce the LFs that would have been observed with higher foreground extinction. If we refer again to the Hillenbrand & Carpenter (2000) extinction map, we see that the very central part of the OMC-1 is characterized by a visual extinction as high as $A_V = 75^m$. For a detailed analysis one should account for the spatial variation of the extinction, as done e.g. by Hillenbrand & Carpenter (2000), but for the moment let's simply assume the LFs of the outer region and put all sources under $A_J \simeq 10$ mag, $A_H \simeq 6$ mag, and $A_{K_S} \simeq 4$ mag, corresponding to $A_V \simeq 33$ mag. It is immediate to see that shifting the monotonically increasing field LFs to the right by a few magnitudes and subtracting them from the central ones produces no visible change on the central ones.

One can therefore safely conclude that the true LF of the inner region lies between the one derived above subtracting the outer field source density (corresponding to a fully transparent background) and the one originally observed (corresponding to a fully opaque background), which means that the inner LFs overall remain quite flat in the BDs regime (0.075-0.012$M_\odot$).

1.6 Summary

In this chapter we have presented a photometric survey of the ONC in the *J*-, *H*- and K_S-passbands carried out at the 4 m telescope of Cerro Tololo. The survey, covering a field of about $30' \times 40'$ centered about $1'$ southwest of the Trapezium, has been performed in parallel to visible observations of the same region made in La Silla (Da Rio et al. 2009). The two datasets constitute the first panchromatic survey covering simultaneously the ONC from the *U*-band to the K_S-band.

The final catalog, photometrically and astrometrically calibrated to the 2MASS system, contains 7759 sources, (including 174 and 22 sources whose photometry has been taken directly from the 2MASS and Muench et al. (2002) catalogs, respectively). This represents the largest NIR catalog of the ONC to date. Our sensitivity limits allow to detect objects of a few Jupiter masses under about $A_V \simeq$10 magnitudes of extinction.

We present the 2CDs, CMDs and the LFs for three regions centered on the Trapezium containing the same number of sources (excluding the M43 subcluster). Sources in the inner region typically show IR colors compatible with reddened T Tauri stars, whereas the outer fields are dominated by field stars seen through an amount of extinction which decreases with the projected distance from the center.

The CMDs allow to clearly distinguish between the main ONC population, spread across the full field, and background sources. The position of the ONC peak slightly drifts to lower mass and bluer colors moving from the inner to the outer region, suggesting that the inner cluster contains a higher fraction of massive and young stars. This points to a scenario in which star formation in the ONC has proceeded from the outside to the inside increasing the efficiency of massive star formation. After correction for completeness, the LFs in the inner region remains nearly flat, with marginal contamination from background sources.

Chapter 2

The extinction map of the OMC-1 molecular cloud behind the Orion Nebula

The closest event of massive star formation is occurring at present in the direction of the Galactic anticenter (l=209°, b=-19°), in the Orion constellation. The ON represents the most spectacular signature of star formation activity in this region. The ON is a blister HII region carved into the OMC-1 giant molecular cloud by the UV flux emitted by a handful of OB stars, the so-called Orion "Trapezium" (Muench et al. 2008; O'Dell et al. 2008), the most massive members of the ONC. Given its youth, vicinity, and low foreground extinction, the observed LF of the ONC can be converted into a true IMF with relatively modest assumptions (Muench et al. 2002, and references therein). It is largely for this reason that the ON and its associated cluster are regarded as a critical benchmark for our understanding of the star formation process.

In order to build a reliable LF, especially in the substellar regime (BDs and planetary mass objects) and to explore its spatial variations with the distance from the cluster center, it is necessary to remove the contribution of non-cluster sources. In principle, this requires the acquisition of thousand of spectra of faint sources distributed over the bright nebular background. On the other hand, the number of contaminant sources, both galactic and extragalactic, can be estimated using the most recent models for stellar and galaxy counts at various wavelengths. The main complication in this case arises from the presence of the OMC-1, which provides a backdrop to the ONC of high and non-uniform extinction. Deriving an accurate extinction map would be beneficial not only to better discriminate the ONC membership, but also to understand the 3-D distribution of the cluster, still partially embedded within the ONC, and the evolutionary history of the region.

In this chapter we present a reconstruction of the OMC-1 extinction map based on the analysis of the NIR source catalog we compile in Chapter 1. In Sect. 2.1 we briefly review the previous studies relevant to the ON region. In Sect. 2.2 we illustrate our statistical method to disentangle background stars from the cluster population. By combining an estimate of the interstellar extinction affecting each contaminant star with the source count density, we derive the OMC-1 extinction map. In Sect. 2.3 we apply a similar statistical procedure to the candidate cluster members, deriving an extinction map for the dust in the foreground ON. Finally, in Sect. 2.4 we compare our maps to previous studies, and we briefly discuss their main features and similarities to stellar distributions.

2.1 Overview of previous studies

A number of previous studies provide results relevant to the issue of the galactic reddening in the direction of OMC-1.

Schlegel et al. (1998) (SFD98 hereafter) combined the *COBE*/DIRBE observations (100 μm and 240 μm) and the *IRAS*/ISSA observations (100 μm) to obtain a full-sky 100 μm map with $\sim 6'$ resolution. On the basis of the correlation between the Mg line strength and the $(B-V)$ color of elliptical galaxies, they were able to calibrate their column-density map to a $E(B-V)$ color excess map. Their all-sky reddening map, available through the NASA/IPAC Infrared Science Archive[1] Dust Extinction Service web page, represents the benchmark for the following studies of our region.

The accuracy of the SFD98 maps has been analyzed by Arce & Goodman (1999), who compared the extinction map of the Taurus dark cloud with the extinction maps obtained using four other methods, i.e. 1) the color excess of background stars with known spectral types; 2) the ISSA 60 and 100 μm images; 3) star counts; and 4) optical color excess analysis. These four methods give similar results in regions with $A_V \leq 4$. Their comparison shows that the extinction map derived by SFD98 tends to overestimate the extinction by a factor of $1.3 \div 1.5$. They ascribe this discrepancy to the the calibration sample of ellipticals used by SFD98, which containing few sources with $A_V > 0.5$ may

---

[1] `http://irsa.ipac.caltech.edu/applications/DUST/`

lead to a lower estimate of the opacity. Arce & Goodman (1999) also find that when the extinctions shows high gradients ($\gtrsim 10^m/deg$, see their Fig. 1), its value is generally smaller than that given from SFD98, and argue that the effective angular resolution of the SFD98 map could be somewhat larger than $6'$.

Dobashi et al. (2005) obtained another all-sky absolute absorption map applying the traditional star-count technique to the "Digitized Sky Survey I" (DSSI) optical database, which provides star densities in the range ~1–30 arcmin^{-2}. Comparing the SFD98 maps to their results in the Taurus, Chameleon, Orion and Ophiucus complexes, they found that SFD98 extinction values are generally up to 2-3 times larger (see their Figs. 46, 47 and 48). A least-squares fit of the two extinction estimates in the $A_V \leq 4$ gives a proportionality coefficient of 2.17, while the same analysis in the $A_V \geq 4$ suggests a coefficient of ~ 3. The authors discuss the possible causes of discrepancy. First, they stress that the SFD98 map are mostly sensitive to the total dust along the line of sight, while their maps measure the extinction due to the nearby dust, as the optical thickness is much larger in the visible than in the far infrared. Second, they point out that the low resolution ($\sim 1\,\mathrm{deg}$) of the temperature map adopted by SFD98 cannot reproduce the typical high spatial frequency temperature variations across dark dense clouds. Finally, they suggest that SFD98 do not account for enhancement in the far infrared emission by fluffy aggregates: this excess emission could explain the inconsistency between SFD98 map and maps derived using other methods. Unfortunately, DSSI optical plates saturate in proximity of the Trapezium cluster, so a large fraction of the ONC field is excluded from their analysis.

An extinction map limited to the inner $\sim 5' \times 5'$ region of the ONC was provided by Hillenbrand & Carpenter (2000) on the basis of the C^{18}O column density data of Goldsmith et al. (1997), with a $50''$spatial resolution. A comparison of the extinction map they derive with the extinction obtained by SFD98 shows that that the SFD98 extinction is generally ~ 3 times larger.

In summary, the SFD98 extinction map for the OMC-1 is still the only one covering the entire ONC field. However, its spatial resolution ($6'$) is limited and the accuracy, in a region as complex as the OMC-1, remains questionable.

In Sect. 2.2 we overcome most of the issues listed above using photometric data in the NIR bands, as they offer several well known advantages. First, 90% of the galactic population is made up of M dwarfs which, by virtue of their

Spectral Energy Distribution (SED), radiate mostly in the NIR. Second, the extinction is lower at IR wavelengths and therefore stars here can be more easily detected through optically thick clouds. Third, the high surface density of field stars allows to overcome the limited spatial resolution typical of far-infrared wide-field surveys used to measure diffuse dust emission. As a caveat, however, we anticipate that the number of detected background stars will be limited by the brightness of the background, which affects the completeness limit of the NIR survey (Sect. 2.2). This effect will be taken into account in our analysis.

2.2 The OMC-1 extinction map

To compute a new extinction map of the OMC-1 region, we use the NIR catalog we compile in Chapter 1. We concentrate our analysis on the (H,H-K_S) CMD of the ∼6000 point-like sources with both H and K_S measured photometry. Lombardi & Alves (2001) show that the inclusion of the J magnitudes can reduce the noise of the extinction measurements by a factor of two, especially in regions characterized by low extinctions. Unfortunately, this is not our case. By using the full sample of stars detected in the H and K_S bands, we greatly increase the stellar density and therefore maximize the angular resolution of our map, since our photometric catalog is shallower in the J-band. Our survey also lacks deep J-band observations of the North-East corner of their field, which makes the deep field covered by the the J-band smaller by about 9% than the field covered in H and K_S-bands. Later in this chapter we will include the J-band data, when we will consider the extinction map toward the ONC, which lays in the foreground of the OMC-1.

The (H,H-K_S) CMD in Fig. 2.1 shows a characteristic bimodal distribution: a first group of stars (the ONC) is clustered at H-K_S=0.5 and H=12, whereas a second group of fainter objects appears clustered around H∼17. This second group also has a peak, but this is a selection effect, as the number of faint sources drops at $H \gtrsim 17.5$ in correspondence of the sensitivity limit of our survey.

Figure 2.1 also shows a 2 Myr isochrone appropriate for the ONC (solid green line) and the density contour of the galactic stellar population along the line of sight of the ONC (solid contours). The galactic population has been derived from the Besançon galactic model (Robin et al. 2003)[2], computed at the galactic coordinates of the ONC over our survey area of 0.329 deg^2. For

---

[2] `http://bison.obs-besancon.fr/modele/`

each star we computed synthetic photometry in the 2MASS system using the grid of atmosphere models of Allard et al. (2010). Since the galactic model also provides for each star the distance and interstellar extinction, both parameters were accounted for in the synthetic photometry.

Of the 4868 sources with $H \leq 18$ returned by the model, 4616 (≈95%) lie at distances larger than 420 pc. Their colors will generally be further reddened by the OMC-1. In Fig. 2.1 we plot (dashed lines) the galactic model reddened by $A_V = 6$, an *ad-hoc* value chosen to shift the contours in the same region occupied by the second peak at $H \sim 17$ in the (H,H-K_S) diagram. As anticipated in Chapter 1, this confirms that the second peak in Fig. 2.1 is fully compatible with the reddened galactic population.

The peculiar morphology of the CMD, characterized by two well separated peaks associated to the ONC and the reddened galactic populations, allows us to assume that sources fainter than H=15 or redder than H-K_S=1.3 (respectively below and to the right of the dotted lines in Fig. 2.1) are largely background field star, being either too faint or too red to belong to the ONC, and vice versa for the other sources within the area. This is a first order criterion that can be further refined. Firstly, we can take advantage of the finer angular resolution of the ACS images obtained for the HST Treasury Program to discard 73 double stars and 166 extended objects, either background galaxies or proplyds (Ricci et al. 2008). Moreover, by looking at the JHK_S 2CD for the subsample of stars with available J magnitude, we find 61 "field" stars well compatible with the locus of reddened circumstellar disks (Sect. 2.3). These sources have been therefore moved to the cluster sample. Our final samples are thus made up of 1716 cluster sources and 1913 background galactic stars.

Figure 2.2 shows the projected density contours for the two samples of background and cluster stars. The relatively low surface density of background stars in the direction of the Trapezium cluster indicates that the optical depth of the OMC-1 reaches its maximum behind the Trapezium. Vice versa, the density of bona-fide cluster members reaches its maximum in the direction of the Trapezium cluster and decreases towards the outskirts of the ON, as already suggested by e.g. Hillenbrand & Hartmann (1998). The density of stars, either background stars or cluster members, is critical in our statistical derivation of the extinction map of the OMC-1 (Sect. 2.2.2) and of the ON (Sect. 2.3) and drives the angular resolution of our derived maps.

It is clear that the two samples are not pure, e.g. there are BDs and/or plan-

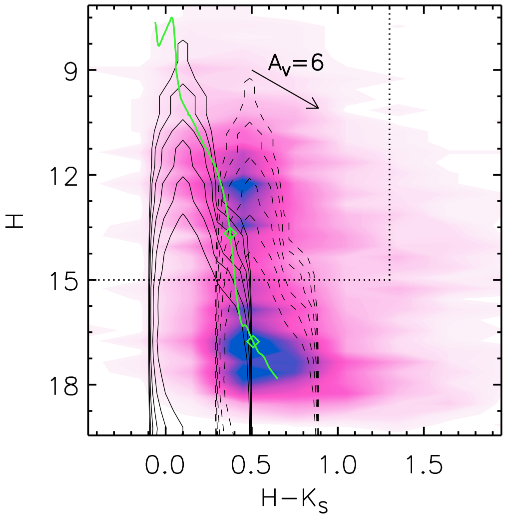

Figure 2.1: Density map in the (H,H-K_S) CMD of all point-like sources in our catalog with measured HK_S photometry (color-filled areas), together with the 2 Myr isochrone (solid green line, the diamond symbols correspond to 1$M_\odot$ and 0.1$M_\odot$ from top to bottom respectively). Two main populations are apparent: the ONC clustered at H=12 and the bona-fide background stars at H∼17. The latter population is to be compared with the synthetic galactic population provided by Robin et al. (2003) (solid contours) after accounting for the extinction provided by the OMC-1. The case of a constant A_V=6 across the cloud is shown in dashed contours, the highest ones roughly overlapping with the observed background population. The dotted line represents our safe selection criterion: any source fainter than H=15 or redder than H-K_S=1.3 is considered a field star, provided that its colors are not compatible with the reddened CTTSs locus (Sect. 2.3).

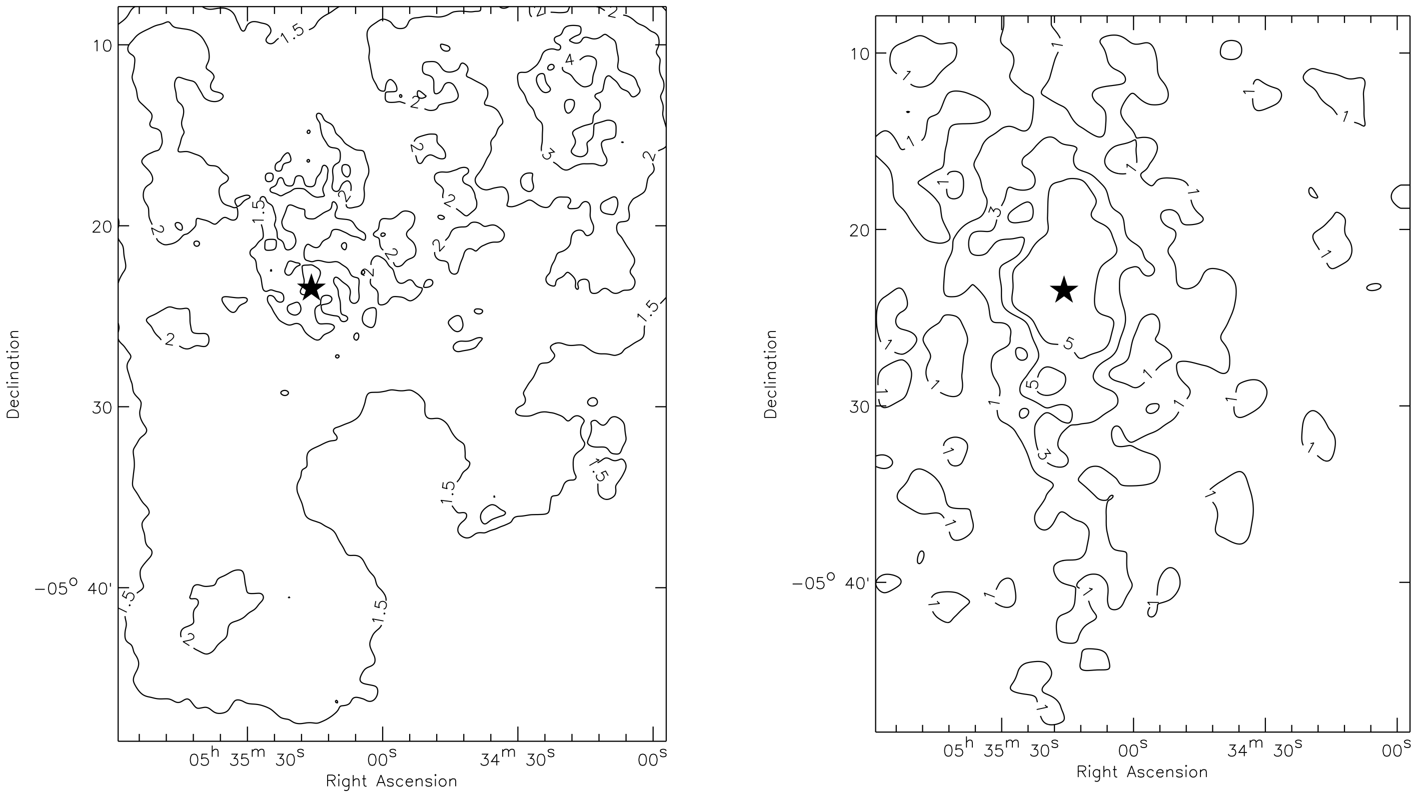

Figure 2.2: Projected surface density of bona-fide background stars (left panel) and of bona-fide cluster members (right panel), as selected in Sect. 2.2. The contour labels give the density of stars in $arcmin^{-2}$. In the direction of the Trapezium cluster (the star symbol indicates the position of Θ^1OriC, assumed to be the cluster center) we find the minimum density of background stars, while it increases towards the outskirts of the cloud. This is indicative of the decreasing optical thickness of the OMC-1 with increasing projected distance from the cluster center. Conversely, the surface density of cluster members steeply increases with decreasing distance from Θ^1OriC.

etary objects belonging to the cluster that may have been improperly included in the background sample. According to the previous studies of the ONC IMF (see Muench et al. 2008, and references therein), the fraction of sources having substellar masses decreases with decreasing mass and therefore one may argue that the background sample is poorly affected by the presence of ONC member with very low masses. By constraining the stellar density to match the average extinction, we will further reduce the cases of spurious identifications. In any case, contamination will remain a source of uncertainty.

While it is possible to assume that the intrinsic color of a cluster star (neglecting disk excess emission) roughly corresponds to that of a source on the 2 Myr isochrone, for the background population there is no such isochrone. In the following sections we describe the statistical approach (Sect. 2.2.1) we have used to derive the extinction affecting each background star and consistently derive the extinction map of the OMC-1.

2.2.1 The extinction affecting each background star

The basic idea of our method, similar to the one outlined by Hillenbrand & Carpenter (2000), is illustrated in the left panel of Fig. 2.3. Each star is represented in the CMD by a 2D probability distribution (the ellipse at the bottom right of the figure), where the shape of the distribution is due to the correlation between the H and H-K_S measures, with their uncertainties. This density distribution has been uniformly binned in a 20×20 grid, resulting in 400 grid points.

We project each grid point backward in the reddening direction, tracing a stripe which intersects the galactic population model. Each grid point is thus associated to a certain number of galactic stars with different extinction values, without any restriction on the maximum extinction allowed. Each of these stars is a candidate to represent the extinction-corrected photometry of the grid point. The central panel of Fig. 2.3 shows the cumulative distribution $F(A_V)$ of the extinction distribution of the candidates associated to the grid point shown in the left panel.

Using the cumulative distribution of A_V, for each grid point we randomly draw 100 A_V–values and assign to the full set of 100 estimates of A_V a weight given by the 2D probability density distribution of the given grid point. Repeating this process for all grid points, we obtain a total of 400×100=40000 probability estimates, each one with its own weight: the weighted mean of this

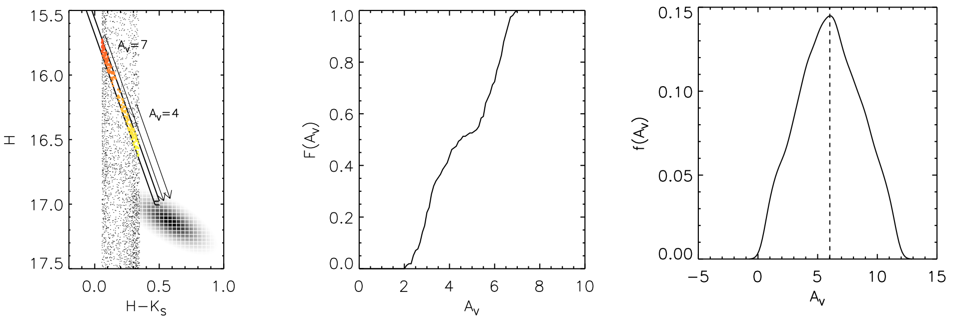

Figure 2.3: *Left panel* – Example of our extinction-correction algorithm for the star with ID=578 in our catalog. The star is represented in the CMD by a regularly gridded 2D gaussian density distribution, and to each grid element it corresponds a stripe of the galactic model (represented in dots) parallel to the extinction direction. Extinction-corrected candidates for the outlined grid point are coded with colors from yellow to red according to increasing A_V. *Central panel* – Cumulative distribution $F(A_V)$ for the colored synthetic galactic stars in the left panel. For each A_V, this function represents the fraction of candidate extinction-corrected photometries with extinction $\leq A_V$. *Right panel* – Weighted probability density function $f(A_V)$ of the 40000 probabilistic A_V estimates for the representative case shown in the left panel, computed using a gaussian kernel. The weighted mean of the sample (dashed vertical line) is our best estimate of the true extinction affecting the star.

sample gives the most likely estimate of the extinction affecting a given observed star. The right panel in Fig. 2.3 shows the weighted probability function $f(A_V)$ corresponding to the 40000 random estimates of A_V; to avoid data binning and for the sake of smoothness, the function is computed using a gaussian kernel density estimator (Silverman 1986). The computation is repeated for all background sources, providing an extinction estimate, with relative uncertainty, for each star of the sample.

2.2.2 Computation of the extinction map

To compute the OMC-1 extinction map, we project over the original survey area a grid of points every 100×100 pixels (corresponding to $30'' \times 30''$). For each grid point we select the 20 closest background stars within 1,000 pixels ($5'$). This limit is meant to prevent that, especially in regions with high extinction (A_V >15) where the density of background stars can be extremely low, the algorithm collects sources over an area too widespread. Thus, by setting an upper limit to the distance of background stars, we tend to preserve the angular resolution of the extinction map at the price of working with smaller statistical samples and therefore with locally more uncertain results. The value of $5'$ has been tuned to make sure than even in the regions with the highest extinction and lowest background density the algorithm will find a few background stars within that distance. This limit is also comparable to the scale size of major nebular structures seen in the NIR images.

Each sample of 20 (or less) background stars is averaged using an iterative sigma-clipping routine, deriving a robust estimate of both the mean local extinction $\bar{A_V}$ and standard deviation $\sigma_{\bar{A_V}}$. This would represent the solution to our problem, except that we want to make sure that the observed surface density and brightness distribution of the background sample is still compatible with the model. To this purpose, we apply the $\bar{A_V}$ extinction to the synthetic galactic model and compare the local density of the reddened model population to the observed one.

The predicted density of the reddened galactic population has to be adjusted for the completeness of the survey, which statistically accounts for the success/failure of detection based on the magnitude of both stars and local background. In Sect. 1.3 we computed the completeness levels in three concentric regions centered on Θ^1OriC, neglecting any variation inside each region. For this study we now use the same fake-star experiment, this time computing the "local" completeness appropriate for each grid point in the extinction map.

It turns out that, particularly within a few arcminutes from the Trapezium cluster, the number of predicted background stars is lower than the number of the observed ones. The excess sources are, most probably, ONC members wrongly identified as background stars, having photometry matching our background selection criteria. To statistically reject these extra sources, for each group of 20 stars we discard the background star with the lowest extinction $A_{V,min}$, assuming it is a cluster member, and replace it with a new, further background star with $A_V > A_{V,min}$, if existing (we are still constrained by the 1,000 pixels maximum distance). By decreasing the density of background sources, we obtain an extinction map which matches both the typical reddening and source density of the galactic component, averaged over $5'$, or less. The result is shown in Fig. 2.4, where we have interpolated the discrete gridding of the map using the IDL `GRIDDATA.pro` routine. The angular resolution ranges between $1.5'$ and $5'$, depending on the density of background sources (Fig. 2.2). In correspondence of the highest extinction values the map reaches its worst resolution, as expected.

The error map shown in Fig. 2.4 shows a typical uncertainty $A_V \lesssim 1$. The regularity in this map is due to the fact that for each grid point, apart the Trapezium region, the algorithm collects the requested 20 stars within a distance shorter than the limit of $5'$. It follows that the number of stars in the analyzed subsample (corresponding to the given grid point) does not depend on the stellar density, but on the combination of the density and the angular resolution of the extinction map.

2.2.3 Biases in the selection of background stars

Foreground contamination

In deriving our extinction map we have assumed that the foreground contamination is closely modeled by the Besançon synthetic galactic population. It is otherwise well established that the ONC (also known as Orion subgroup Id) is neighbored by three somewhat older subgroups of stars (Ia, Ib, and Ic, Brown et al. 1994), which are located at distances ranging from ~360 to 400 pc and have ages from ~2 to 11.5 Myr. The most likely subgroup from which we would see contamination in our data is subgroup Ic, which is located along the same line of sight of the ONC and is thought to be as young as 2 Myr (Brown et al. 1994). Thus, we expect little differences between the ONC and subgroup Ic isochrones, the main source of scatter being the smaller distance modulus, providing photometry up to 0.3 magnitudes brighter.

Considering that subgroup Ic is, at most, as reddened as the ONC by interstellar extinction, we expect that the isochrone shown in Fig. 2.1 also applies to the CMD of subgroup Ic. Thus, we still expect to find in each neighborhood the two main populations discussed above, the least reddened containing both ONC and subgroup Ic members, together with foreground field stars. Therefore, the presence of spurious sources belonging to the Ic subgroup should not affect our computation of the OMC-1 extinction map.

Contamination by extragalactic sources

In deriving the OMC-1 extinction map, we model the background sample with the reddened galactic model but neglect any contamination by extragalactic sources. We now address the reliability of this assumption.

To compute the extragalactic counts model reddened by the OMC-1, we

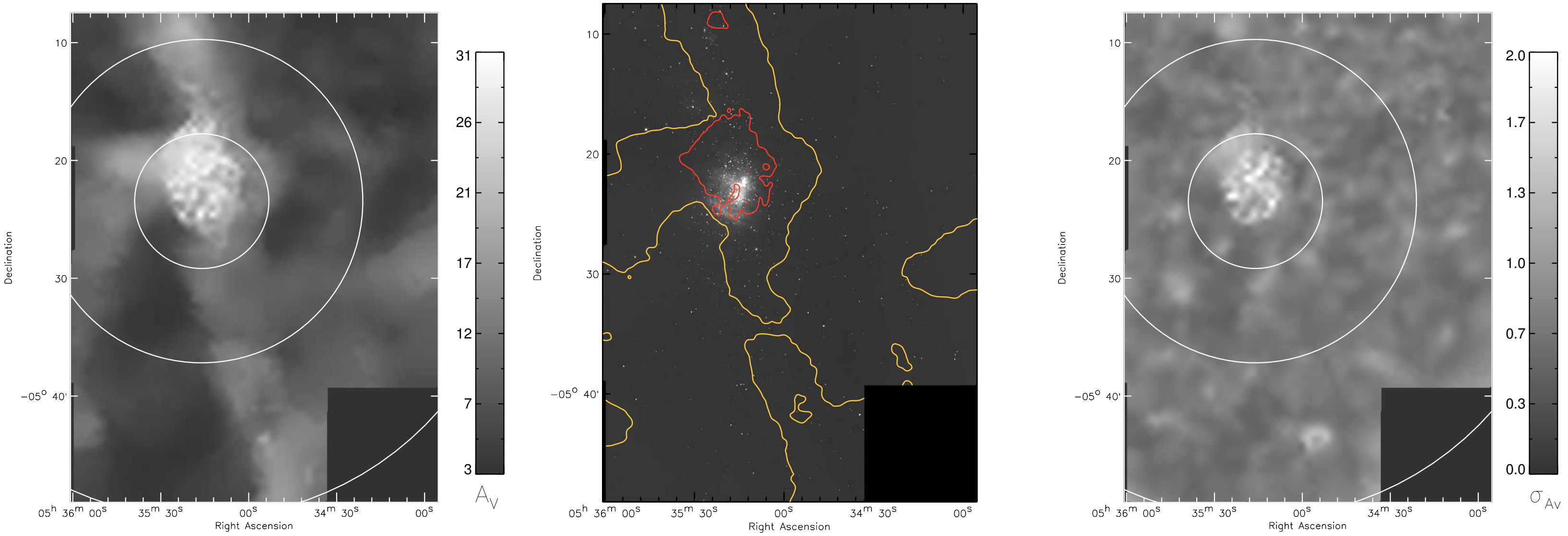

Figure 2.4: *Left panel* - Extinction map of the OMC-1 derived as described in the text. The color bar shows the correspondence between the gray scale and visual extinctions. We also mark the boundaries of the three regions outlined in Sect. 1.3. *Central panel* - ISPI K_S mosaic of the surveyed ONC. The overplotted contours represent the A_V=10 (yellow line) and the A_V=20 (red line) levels. *Right panel* - The error map for our derived OMC-1 extinction map. The OMC-1 extinction map and the corresponding error map are also available in electronic form at the CDS.

use a deep NIR catalog of galaxies based on SOFI observations in an area of 340 arcmin^2, centered on the coordinates RA=$3^h\ 32^m\ 28^s$ and DEC=-27° 48′27″ (kindly provided by T. Dahlen, *private communication*). At these coordinates, the interstellar galactic extinction is particularly low (SFD98 extinction map provides $A_V \sim 0.02$), i.e. entirely negligible compared to the extinction provided by the OMC-1. Thus, assuming that the distribution of galaxies beyond the OMC-1 is well reproduced by the SOFI catalog, we randomly and uniformly spread the sample of galaxies over the field. Then, assuming that the main source of extinction is provided by the OMC-1, we add the proper amount of extinction based on our map, converting from visible to the infrared wavelengths via the extinction curve given by Cardelli et al. (1989):

$$A_J = 0.288A_V;\ \ A_H = 0.182A_V;\ \ A_{K_S} = 0.118A_V \tag{2.1}$$

We repeat this procedure 1,000 times, and we average the sample of 1,000 extragalactic CMDs, in order to minimize statistical fluctuations. We find that the extincted extragalactic population accounts for just ~1% of the observed background sample in Fig. 2.1 down to H~17. This is roughly the same fraction of galaxies found by Ricci et al. (2008) in their analysis of the deep ACS images of the ON, and confirms our hypothesis of negligible extragalactic contamination. We also remark that we removed all the galaxies resolved by ACS from the analyzed sample, thus further minimizing the incidence of extragalactic sources.

2.3 The Orion Nebula extinction map

It is known that most of the extinction toward the Trapezium cluster arises at the interface between the M42 HII region and the neutral diffuse matter (see O'Dell et al. 2009, and references therein). As indicated by O'Dell & Yusef-Zadeh (2000), internal extinction may also play a role. Aiming at mapping the extinction provided by the diffuse matter in front of the OMC-1 (the "ON extinction" hereafter), we focus now our attention on the sample of stars which are candidate members of the ONC. All these sources have been detected in the J, H and K_S-bands.

We face now a different set of problems. Whereas one can safely assume that the 2 Myr isochrone provides a relatively accurate locus for the dereddened stellar photospheres, one has to consider the spurious presence of circumstellar matter, disks in particular, which may affect the brightness (and to a lesser ex-

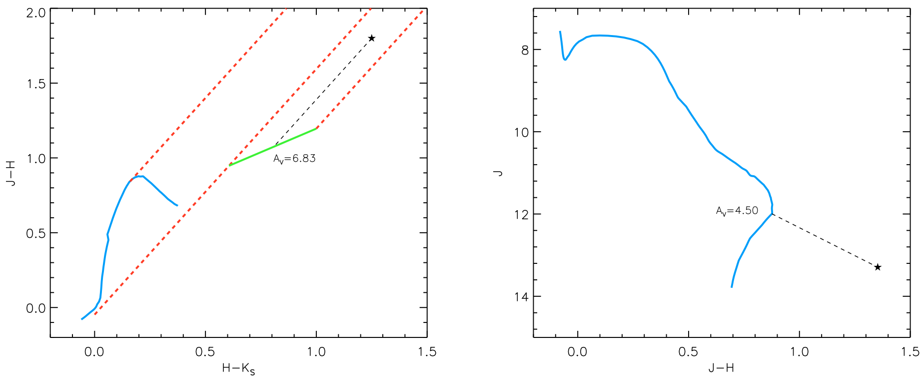

Figure 2.5: *Left panel* - Example of the extinction-correction algorithm, coded with the black dashed line, for a star with colors compatible with the reddened CTTSs locus provided by Meyer et al. (1997) (the green solid line). The blue solid line is the 2 Myr old isochrone suitable for the ONC. The red dashed lines are parallel to the reddening direction and bracket the regions occupied by the previous loci reddened by any A_V. *Right panel* - Example of the algorithm for a star with NIR colors compatible with extincted photospheric colors. The blue line represents the isochrone in the (J,J-H) diagram.

tent the IR colors) of the sources. Depending on the typical disk flaring angles, which are enhanced by the UV radiation within the HII region (Robberto et al. 2002) the sample of edge-on disks may be relevant. We shall assume that they still represent a small contamination, since they tend to move the sources beyond our K_S=15 limit for cluster membership. Probably more important is the fact that ∼11% of the point-like sources in the ISPI catalog do not show NIR colors compatible with extincted photospheric colors. Their position in the (J-H,H-K_S) diagram is compatible with the extincted CTTSs locus introduced by Meyer et al. (1997) (Fig. 2.5), i.e. their photometry is indicative of strong excess emission from circumstellar disks. Following Meyer (1996), we split our candidate members sample in two subgroups. If the observed colors are compatible with reddened CTTSs colors, then we correct the observed colors for extinction taking the CTTSs locus as reference. Otherwise, in order to minimize the effects of eventual NIR excesses from circumstellar disks, we correct our sources for extinction in the (J,J-H) diagram, taking the 2 Myr old isochrone as the reference locus. In both cases, our algorithm moves the observed photometry to the reference locus (either the CTTSs locus or the isochrone) along the extinction direction, computed using the Cardelli et al. (1989) reddening law. Figure 2.5 graphically shows our extinction-correction algorithm.

The set of A_V estimates is then locally averaged following the same strategy described in Sect. 2.2.2. In this case, we adopt a maximum angular resolution of 1,500 pixels ($\sim$7.5$'$) to allow our algorithm to find a good number of cluster members in the outskirts of the Nebula, where the surface density of stars is generally low (see Fig. 2.2). The resulting extinction map, with the associated error map, are shown in Fig. 2.6.

We find that in the direction of the Trapezium cluster the ON extinction is generally $A_V \lesssim 3$, with a clear increase ($A_V \gtrsim 6$) in correspondence of the dark ridge along the north-east edge of the HII region, which is therefore a foreground structure. The ridge is part of a larger bow-shaped feature extending from the east to the north of the ON. These findings are fully consistent with the map derived by O'Dell & Yusef-Zadeh (2000) combining radio and optical measurements over an area $360'' \times 425''$ wide around Θ^1OriC.

2.4 Discussion

2.4.1 Structure of the OMC-1 beyond the Orion Nebula Cluster

Alongside with the previous studies illustrated in Sect. 2.1, our map (Fig. 2.4) shows that the OMC-1 surface density generally increases towards the Trapezium. In particular, we find that the Trapezium cluster is located in front of a high-extinction region ($A_V \gtrsim 30$) extending $\sim$10$'$ to the north of Θ^1OriC. This region is delimited to the south-east side by a sharp edge: the optical thickness of the OMC-1 decreases steeply by $\sim$20 magnitudes in a few arcminutes. This edge corresponds to the Orion Bar, the bright feature directly discernible in the ISPI image (right panel in Fig. 2.4). The steep drop of extinction can be confirmed even by a direct inspection of the images. It is quite evident that the density of faint and red stars suddenly increases to the south of the Orion Bar. A similar extinction drop is found also to the north-eastern edge of the extinction peak, in correspondence of the dark structure, known as the Dark Bay or Fish Mouth, seen in absorption in the optical images of the ON. Elsewhere, the extinction smoothly decreases down to $A_V \gtrsim 4$ with increasing distance from the Trapezium cluster.

On larger scales, the OMC-1 extinction map shows a north-south pattern. The elongated extinction ridge is distributed over the full extent of the survey,

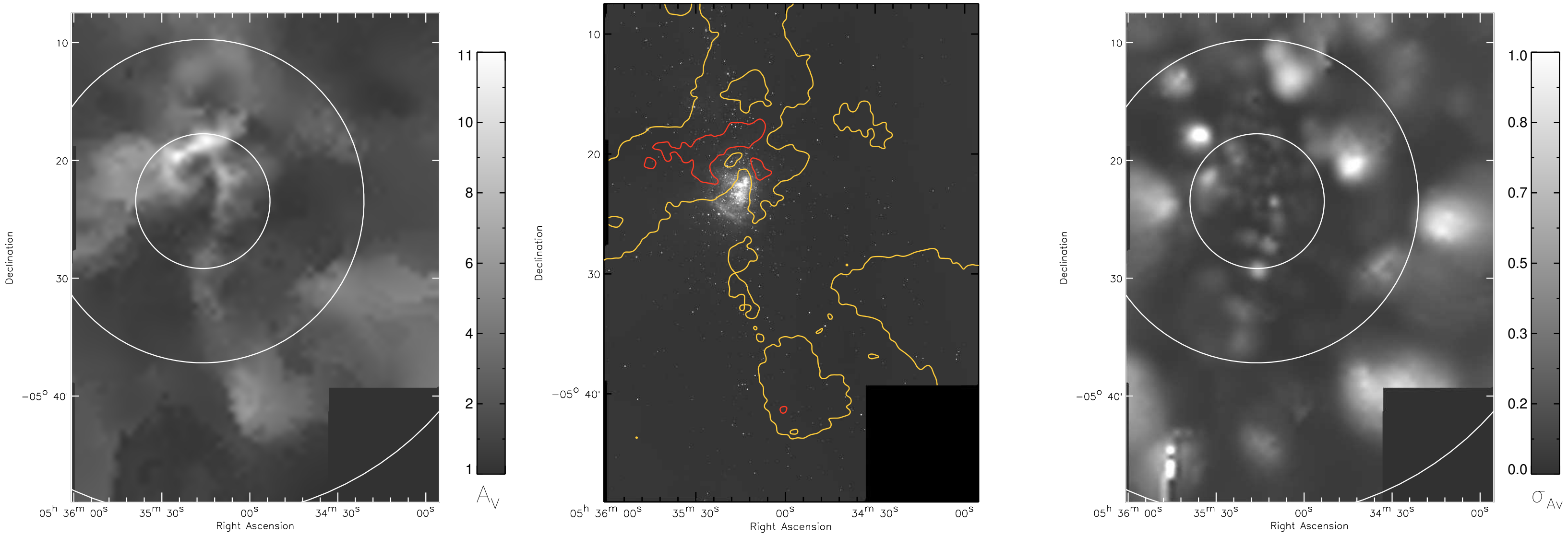

Figure 2.6: *Left panel* - Map of the average extinction affecting the ONC candidate members. The color bar shows the correspondence between the gray scale and visual extinctions. We also mark the boundaries of the three regions outlined in Sect. 1.3. *Central panel* - ISPI K_S mosaic of the surveyed ONC. The overplotted contours represent the A_V=3 (yellow line) and the A_V=6 (red line) levels. *Right panel* - Uncertainty on our derived ON extinction map. The ON extinction map and the corresponding error map are also available in electronic form at CDS.

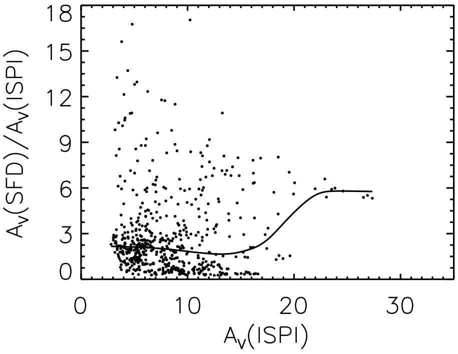

Figure 2.7: Diagram of the ratio r_{A_V} as a function of $A_V(ISPI)$. The solid line is a binned sample median, aimed at stressing the overall trend. This diagram shows that for low extinctions our measurements and the SFD98 extinction are comparable, and that the latter becomes up to 3 times larger for higher extinctions, as found by Dobashi et al. (2005).

reaching the OMC-2/3 star forming region to the north of the ONC (Peterson & Megeath 2008). The extinction map thus follows the dense filament traced by the molecular column density data of Goldsmith et al. (1997).

To compare our extinction map with the one of SFD98, we degrade our spatial resolution down to their value. The pixel-by-pixel ratio $r_{A_V} = \dfrac{A_V(SFD)}{A_V(ISPI)}$ is plotted in Fig. 2.7 as a function of $A_V(ISPI)$. For low extinction values, the SFD98 values generally overestimate the extinction by a factor of 1.5–2, consistently with what found by Arce & Goodman (1999). Moreover, consistently with Dobashi et al. (2005), the SFD98 values are systematically larger than ours, the ratio increasing in the $3 \lesssim r_{A_V} \lesssim 5$ range with the $A_V(ISPI)$ extinction. This is indicative of the fact that SFD98 map is not accurate either in high extinction regions or in regions with high extinction gradients.

2.4.2 Structure of the Orion Nebula

As proposed in the 3-D model of the ON by O'Dell et al. (2009), the boundary between the HII region and the bulk of the neutral matter is made up by a geometrically thin and optically thick shell swept up by stellar winds. Given this model, we argue that the extinction in the Dark Bay direction and the broad feature around it are spatially correlated, the former being a clump of high column density gas inside the remnant of the neutral shell located between the observer and the Trapezium (see Fig. 4 in O'Dell et al. 2009).

On larger scales, the ON is never thinner than A_V ∼2 and this is compatible with the presence of a foreground neutral veil (O'Dell et al. 2009). Furthermore, a north-south pattern is evident, similarly to what is found for the OMC-1 extinction map (Fig. 2.4). This pattern roughly follows the north-south elongation of the ONC observed by Hillenbrand & Hartmann (1998), indicating that the cluster is still partially embedded in the OMC-1. As pointed out by Hartmann & Burkert (2007), this suggest that it might be better to view the ONC as a dense, moderately elongated cluster embedded in a larger scale filamentary stellar distribution rather than a system having a smoothly varying ellipticity as a function of radius. As indicated by Hillenbrand & Hartmann (1998), the close association between the distribution of young stars and the elongated diffuse structures suggests that no dynamical relaxation has taken place so far, i.e. the stellar population has not dynamically adjusted from its initial state.

2.5 Summary

In this chapter we have used the most recent wide-field NIR photometric catalog to discriminate between two main families of stellar sources in the ON region: 1) ONC members, distributed over an area $\sim 30' \times 40'$ roughly centered on Θ^1OriC; 2) background stars. The two samples have been statistically analyzed to derive the extinction maps of the OMC-1 (Sect. 2.2.2) and the foreground ON (Sect. 2.3), with angular resolution $<5'$and $<7.5'$respectively.

Our results show that the OMC-1 generally accounts for the largest amount of extinction, typically $A_V \gtrsim 6$, steeply rising up to $A_V \gtrsim 30$ in the direction of the Trapezium cluster and dramatically dropping south of the Orion Bar. The extinction toward the ON is lower, $A_V \lesssim 3$, with a peak value $A_V \sim 6$ in the direction of the Dark Bay feature. Our findings agree with Hillenbrand (1997), Muench et al. (2002) and Da Rio et al. (2010) who derived that the ONC members are typically extincted by $A_V \lesssim 3$.

Together with Arce & Goodman (1999) and Dobashi et al. (2005), we find that the OMC-1 extinction map proposed by SFD98 is overestimated by a factor of∼3-5, especially in the optically thickest regions. Together with the comparability between our ON extinction map and the results of O'Dell & Yusef-Zadeh (2000), this supports both the robustness of our statistical approach and the general validity of our results over the full spatial extent of the ONC.

The maps of the OMC-1 and the ON are available as FITS files at CDS.

Chapter 3

Empiric NIR colors for low-mass stars and BDs in the ONC

In the last two decades several generations of evolutionary models of PMS objects have been published with continuous improvements on the treatment of the hydrostatic structure, radiation/heat transfer and thermodynamic equilibrium. There are at least 7 different families of published PMS evolutionary calculations that have been widely circulated in machine-readable formats and that span a suitable range of stellar masses: Swenson et al. (1994); D'Antona & Mazzitelli (1997) with 1998 electronic-only update (DM98); Palla & Stahler (1999); Siess et al. (2000) (SDF00); Baraffe et al. (1998) with Chabrier et al. (2000) (BCAH98); Yi et al. (2003); and Tognelli et al. (2011). However, considerable differences still exist as the various sets of evolutionary tracks show systematic differences in the predicted masses and ages of stars in the Hertzsprung-Russel Diagram (HRD) (Hillenbrand & White 2004; Hillenbrand et al. 2008).

The comparison of theoretical predictions with observations on the HRD requires converting observed quantities, e.g. spectral type and some photometry in at least two passbands, into physical parameters like effective temperature and absolute luminosity (see e.g. Hillenbrand 1997). This conversion is normally done using an empirical, or semi-empirical, calibration. It is also possible to take the complementary approach of deriving observational data from theoretical predictions. For example, plotting the photometry of a young stellar cluster in a CMD or 2CD may show structures (like e.g. the cluster isochrone) that can be compared with the results of evolutionary and synthetic photometry calculations. Varying the model parameters one can directly visualize, the effects of metallicity, effective temperature scale, surface gravity, reddening law, accretion (see e.g. Da Rio et al. 2010, D10 hereafter).

No approach is without drawbacks. On the one hand, the empirical corrections needed to derive the physical parameters of PMS stars, like e.g. colors and bolometric corrections, may have been derived on samples of stars which may not be fully representative of the sample under exam. There is a standing tradition, for example, of using for PMS stars the intrinsic colors of Main Sequence stars (e.g. Kenyon & Hartmann 1995). On the other hand, the systematic uncertainties of evolutionary models may compose with those of the atmospheric templates and provide erroneous results. The selection of adequate model atmospheres for PMS stars is especially critical for late type stars (M-type and later), which represent the peak of the IMF (Bastian et al. 2010) and whose SEDs are dominated by broad molecular absorption features. Cool atmospheres ($T_{\rm eff}\lesssim$3000 K) host a variety of molecules and provide an environment for dust condensation, whose role in the heat and radiation transfer through the photosphere cannot be neglected (Allard et al. 2001, 2010). Moreover, for sub-stellar objects, convection may reach the photosphere, which therefore can no longer be treated as a system in radiative equilibrium. It is therefore crucial, particularly for cool atmospheres, to include in the synthesis codes the largest number of molecular lines in order to accurately reproduce the radiation transfer through the atmosphere.

The situation is aggravated by observational limitations. It is hard to obtain high quality data for a statistically significant sample of PMS stars of comparable age and distance. Even in the solar vicinity, rich and young stellar clusters are typically affected by large and inhomogeneous reddening, being still enshrouded in their parental molecular cloud (Lada & Lada 2003), while the stars often show accretion excess. Older systems tend to be spatially spread and affected by membership uncertainties. In this respect, due to its relatively low foreground extinction ($A_V \lesssim 3$, Scandariato et al. 2011) and vicinity (d = 414 pc, Menten et al. 2007), the ONC provides a unique opportunity to analyze the intrinsic colors of its members and assess the accuracy of PMS models.

In the optical wavelength range, a recent attempt to calibrate empirically the colors of PMS stars is presented in Da Rio et al. (2009). In that work, based on optical BVI photometry of the ONC, the authors show how present families of synthetic spectra fail in matching the observed colors, and present a correction based on their data. In D10, they further refine this calibration, limited to the I band and 2 medium bands at $\lambda\sim$770 Å, by explicitly calibrating colors as a function of $T_{\rm eff}$, and by decreasing the lowest $T_{\rm eff}$ limit down to ∼2800 K.

The goal of this chapter is to use the extensive set of spectral types and photometric data available for the ONC to test the theoretical models and to determine with unprecedented accuracy the intrinsic (photospheric) JHK_S magnitudes of the cluster members. The intrinsic NIR colors of PMS stars in Orion we derive will be also appropriate for the (possibly ideal) cluster isochrone, and applicable to young (age$\lesssim$5 Myr) systems in general. In Sect. 3.1 we present the selection of our sample of stars, based on the latest spectral characterization and our recently published NIR photometry. In Sect. 3.2 we refine our list to select the subset of stars most suitable for our purposes. By means of this sample, in Sect. 3.3 we test the most recent atmospheric model of Allard et al. (2010), and in Sect 3.4 we derive the average colors of the cluster. Finally, in Sect. 3.5 we discuss our result and we compare them to the current theoretical predictions.

3.1 The data set

We base our analysis on the ONC NIR photometric catalog of Robberto et al. (2010). This catalog contains JHK_S photometry in the 2MASS system for ∼6500 point-like sources, spread over an area of $\sim 30' \times 40'$ roughly centered on θ^1Ori-C (RA=$05^h35^m16.46^s$, DEC=$-05°23'23.2''$). We cross-match the NIR catalog with the list of BVI photometry of Da Rio et al. (2009). The NIR and optical catalogs originate from *simultaneous* observations of the cluster, and therefore are largely immune from the uncertainties introduced by source variability when multi-band photometry is collected at different epochs.

Da Rio et al. (2011) provide photospheric luminosity, interstellar extinction and accretion luminosity for ∼1,200 stars, whose spectral types are known either from previous spectroscopic surveys (Hillenbrand 1997) or from observations of the narrow-band photometric index of TiO (D10, Da Rio et al. 2011).

In order to extend our analysis down to later M-subtypes and probing the brown dwarfs spectral range, we complement our list with the spectral classification of Riddick et al. (2007, R07 hereafter) for 45 M-type stars not in our catalog. The authors provide extinctions, luminosities and spectral types, together with JHK_S photometry from their previous NIR photometric survey (Lucas et al. 2005).

We also add 41 more stars from the spectroscopic study of Slesnick et al.

(2004, S04 hereafter), which also provides extinction, luminosity and spectral type of the stars. HK_S photometry is taken from Hillenbrand & Carpenter (2000), whereas no J photometry is available.

We correct the NIR photometry for interstellar extinction using the extinction law of Cardelli et al. (1989) and the values of A_V for individual stars from D11, R07 and S04. Spectral types are converted into effective temperature $T_{\rm eff}$ using the conversion scale provided by Luhman et al. (2003), well-suited for PMS stars (Table 3.2). Our list thus contains 1313 stars with spectral type, luminosity L, extinction A_V and extinction-corrected 2MASS-calibrated NIR photometry.

3.2 Extraction of the reference stars

In order to identify a “master” sample of PMS stars that may more adequately represent the intrinsic colors of the ONC photospheres, we need to clean our sample from field stars, outliers and members with NIR fluxes contaminated by circumstellar emission or strong activity.

3.2.1 Age spread

First, we reject outliers in the HRD. Using the list of $T_{\rm eff}$ and L compiled in the previous section, we derive ages and masses through a comparison of their positions in the HRD with the evolutionary models of DM98 (Fig. 3.1), which nicely cover the age and mass range spanned by the ONC.

The distribution of derived logarithmic ages, plotted in Fig. 3.1, indicates that according to this model the characteristic age of the ONC members is ~1 Myr. Aiming at a large statistical sample, representative of the whole cluster, we operate a rough selection retaining all stars with age within the full width at one quarter of the maximum ($5.0 < Log(age) < 6.8$), rejecting all those that appear too young or too old with respect to the average population. This selection thus rejects the stars too bright compared to the average cluster, i.e. the stars which are intrinsically too young, or the ones whose overluminosity is due to either multiplicity or circumstellar excess. We also discard the stars too faint compared to the average cluster, likely belonging to older stellar associations in the Orion complex (Brown et al. 1994).

Using other models would have provided different values for the mean age

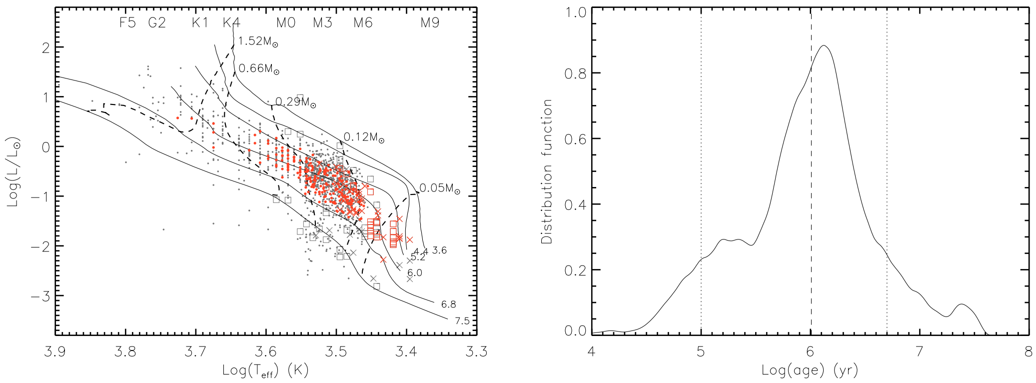

Figure 3.1: *Left panel* - HRD of our list of stars superimposed to the evolutionary model computed by DM98. Solid lines represent the isochrone at different ages (the logarithmic age in year is indicated), while dashed lines show the tracks at fixed mass. Dots, crosses and squares represent the stars from D10, R07 and S04 respectively. The master sample analyzed in Sect. 3.4 is shown in red. *Right panel* - Age distribution of the stars based on the DM98 evolutionary models. This plot indicates that the ONC is ∼1 Myr old. The two dotted lines outline the age range spanned by the analyzed sample of stars.

and lower/upper age limits, but basically the same sample. With these assumptions, the sample reduces to 957 stars.

3.2.2 Circumstellar Activity

We also reject stars showing significant circumstellar activity. For the subsample of stars with BVI photometry taken from Da Rio et al. (2009), D10 provide indications on ongoing accretion through the parameter l defined as:

$$l = Log\left(\frac{L_{accr}}{L_{tot}}\right),$$

where L_{tot} is the total luminosity of the system and L_{accr} is the accretion luminosity. We discard the stars with l >-6 (Fig. 3.2), in order to isolate only the stars showing no evidence of accretion.

We also exclude the stars in the R07 and S04 sublists with spectroscopic evidence of disk activity, mainly the presence CaII emission lines which are commonly attributed to the presence of disk winds. These selections leaves us with 337 stars.

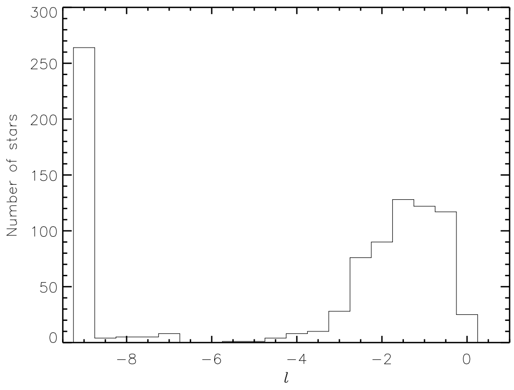

Figure 3.2: Distribution of the accretion luminosities l in our selected sample. Values l <-6 must be regarded as null detection of ongoing accretion, and are kept in the analyzed sample. On the contrary, stars with l >-6 show accretion evidences and are discarded, in order to avoid any contamination to the extinction-corrected photometry.

3.2.3 NIR excess from the inner disk

Circumstellar disks around young PMS stars may also radiate in the NIR domain (Meyer et al. 1997; Cieza et al. 2005; Fischer et al. 2011, and Hillenbrand et al. (1998) for the specific case of the ONC), contaminating the NIR continuum emission of the central stars. To reject sources with photometry contaminated by strong disks excess, we plot in Fig. 3.3 the NIR 2CD of our 311 sources, comparing their extinction-corrected colors to the 1 Myr isochrone of DM98. Whereas the majority of stars appear scattered around the DM98 isochrone, the redder sources (top-right corner of the plot) appear systematically shifted in the region corresponding to the Classical T-Tauri Stars (CTTS) locus proposed by Meyer et al. (1997). These dereddened colors cannot be accounted for by either inaccuracies in the theoretical 2CD or by measurement errors, and must therefore be attributed to circumstellar disk emission. Taking the theoretical isochrone as a proxy for the photospheric colors of the selected stars, we discard 64 stars with extinction-corrected photometry deviating from the isochrone for more than three times their photometric uncertainties.

This is the last step of our selection process. We end up with a master sample made of 254 stars with 2500 K$\lesssim T_{\rm eff} \lesssim$5000 K, in a relatively narrow range of ages and without substantial evidence of non-photospheric activity, either accretion or circumstellar disk emission.

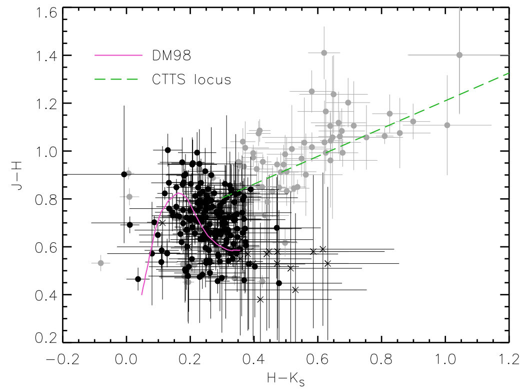

Figure 3.3: 2CD of our sample of stars, compared to the 1 Myr old model provided by DM98 (pink solid line). The observed colors do not strictly follow the theoretical model, indeed they occupy a region elongated along the CTTS locus provided by Meyer et al. (1997) (green dashed line). Circles and crosses represent stars with spectral types provided by Da Rio et al. (2011) and R07 respectively. Gray error bars represent stars with observed colors not compatible with the model at the 3σ level: they are rejected in our analysis.

3.3 Accuracy of the Allard et al. (2010) atmospheric model

The assignment of spectral types of late-type young stars is usually performed in the optical-red domain, as this wavelength range provides the best-studied sets of spectral lines for classification and is least affected by veiling from accretion and/or circumstellar emission. With spectral types at hand, it is then possible to obtain a prediction of the photospheric fluxes in a certain passband by convolving the corresponding filter profile with an appropriate template spectrum. Comparing the observed SED with the theoretical one allows to characterize the continuum due to accretion and/or circumstellar disks (in the near-UV and IR respectively), which may even dominate the photospheric emission.

In this section, we take advantage of the list of stars assembled in Sect. 3.1 to investigate the accuracy of the most recent synthetic atmospheric templates provided by Allard et al. (2010), which significantly improves the previous releases of atmospheric templates from the same group.

Having the luminosity L and the effective temperature $T_{\rm eff}$ of our master sample of stars, we first compute the stellar radius R_* using the Stefan-Boltzmann's law $L = 4\pi R_*^2 \sigma_{SB} T_{\rm eff}^4$. We also derive stellar masses M_* placing the stars in the HRD and comparing their position with the theoretical model of DM98 (Fig. 3.1). We refine the mass estimates taking into account the results of Hillenbrand & White (2004), which analyzed the discrepancies between track-predicted masses and dynamical masses for a sample of PMS stars in binary systems. They find that the DM98 model tends to underestimate masses by ∼20%. We then increase by 20% our track-predicted mass estimates, and we use the resulting values to compute the surface gravities g following the relation $g = GM_*/R_*^2$.

For each star, we then compute synthetic NIR photometry using the atmospheric models of Allard et al. (2010), with the appropriate values for the effective temperature and surface gravity. We also assume the standard solar metallicity for the ONC, as indicated by, e.g., D'Orazi et al. (2009) and Biazzo et al. (2011). The synthetic magnitudes and colors $X_{synthetic}$ are then compared to the corresponding extinction-corrected values $X_{extinction-corrected}$. The differences

$$\Delta X(T_{\rm eff}) = X_{extinction-corrected}(T_{\rm eff}) - X_{synthetic}(T_{\rm eff}) \tag{3.1}$$

represent our proposed corrections to the synthetic NIR colors. These are values to be added to the synthetic colors to derive the correct intrinsic colors of the stars. The corrections ΔH, $\Delta(J-H)$ and $\Delta(H-K_S)$ for the entire master sample are shown in Fig. 3.4 and reported in Table 3.1, as a function of the effective temperature.

The distribution of stars in terms of $T_{\rm eff}$ allows to smoothly fit the ΔX from $T_{\rm eff}$∼2500 K up to $T_{\rm eff}$∼4200 K, while the number of stars at higher temperatures is too low to allow for a robust fit (see Fig. 3.1). The best fits indicate that the H magnitude is overestimated by the model by ∼0.2 magnitudes, with an uncertainty $\lesssim$0.1 magnitude. The same is true for the colors, with a smaller offset of the order of $\lesssim$0.1 magnitudes. One possible explanation for these discrepancies is that the atmospheric model provides H fluxes larger than the observed ones. This may suggest that, despite the improvements in the latest release, the model still inaccurately accounts for the continuum opacity of water vapor, which significantly affects the NIR SED of cool stars.

3.3.1 Sistematic uncertainties

The corrections we have derived are based on the reddening law used to correct the observed photometry for extinction and on the accuracy of the mass

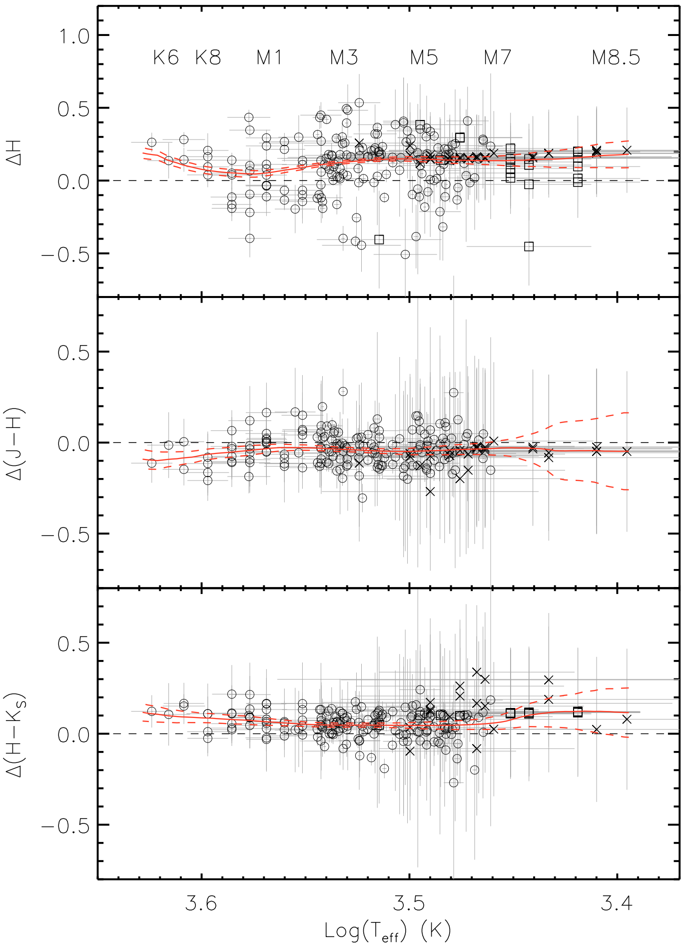

Figure 3.4: ΔH, $\Delta(J-H)$ and $\Delta(H-K_S)$ corrections to the synthetic colors (from top to bottom respectively). Circles, crosses and squares represent stars with spectral types provided by Da Rio et al. (2011), R07 and S04 respectively, while the error bars take into account the uncertainties in both the extinction-corrected photometry and the synthetic photometry. Red solid lines show our smooth outlier-resistant fits, together with the corresponding 1-σ confidence bands (dashed red lines).

Table 3.1: Corrections to the Allard et al. (2010) synthetic colors for LMSs and BDs in the ONC.

		R_V=3.1			R_V=5.5		
SpT	$T_{\rm eff}{}^a$	ΔH	Δ(*J*-*H*)	Δ(*H*-K_S)	ΔH	Δ(*J*-*H*)	Δ(*H*-K_S)
M8.5	2555	0.17	-0.05	0.12	-	-	-
M8	2710	0.15	-0.04	0.12	-	-	-
M7	2880	0.14	-0.03	0.06	0.20	-0.04	0.02
M6	2990	0.14	-0.04	0.05	0.22	-0.06	0.02
M5	3125	0.15	-0.05	0.05	0.24	-0.08	0.02
M4	3270	0.14	-0.05	0.05	0.25	-0.09	0.04
M3	3415	0.12	-0.04	0.05	0.23	-0.08	0.04
M2	3560	0.09	-0.03	0.05	0.18	-0.06	0.05
M1	3705	0.05	-0.03	0.07	0.12	-0.05	0.06
M0	3850	0.05	-0.05	0.08	0.08	-0.06	0.07
K8	3965	0.07	-0.07	0.09	0.09	-0.07	0.07
K7	4060	0.11	-0.08	0.09	0.11	-0.08	0.08
K6	4154	0.16	-0.10	0.10	0.15	-0.08	0.09

Notes. (a) Temperature scale of Luhman et al. (2003).

estimates. The results may be influenced by the assumed ratio of total to selective extinction R_V (Sect. 3.3.1) and by the accuracy of the mass (and surface gravity) estimates derived from the DM98 theoretical model (Sect. 3.3.1).

Effects of the assumed R_V

In our derivation of the intrinsic NIR colors of stars in the ONC, we have assumed that the total to selective extinction is $R_V = A_V/E(B-V)$=3.1, which is the typical galactic value. However, it has been proposed that the reddening law toward the OB stars of the Orion association can be better parametrized by $R_V \simeq 5.5$, typical of larger dust grains (Johnson 1967; Costero & Peimbert 1970; Baldwin et al. 1991; Osterbrock et al. 1992; Greve et al. 1994; Blagrave et al. 2007).

Assuming R_V=5.5, the values of $A_V^{5.5}$ estimated by D10 turn out to be typically larger than the corresponding $A_V^{3.1}$ values by ~10%. Moreover, given the R_V dependence of the extinction law proposed by Cardelli et al. (1989), it turns out the in the NIR the absorption is ~1.2 times larger if R_V=5.5 is assumed. The differences Δm_λ between the extinction corrected magnitudes assuming R_V=5.5 and R_V=3.1 is thus given by

$$\begin{aligned} \Delta m_\lambda = & \quad (m_{obs} - a_\lambda^{5.5} A_V^{5.5}) - (m_{obs} - a_\lambda^{3.1} A_V^{3.1}) = \\ \simeq & \quad a_\lambda^{3.1} A_V^{3.1} - (1.1 \times 1.2) a_\lambda^{3.1} A_V^{3.1} \simeq -0.3 a_\lambda^{3.1} A_V^{3.1} \end{aligned} \qquad (3.2)$$

where m_{obs} is the observed magnitude at wavelength λ and $a_\lambda = A_\lambda/A_V$.

Several studies (e.g. (Hillenbrand 1997), (Hillenbrand & Carpenter 2000), (Muench et al. 2002), (Da Rio et al. 2010), (Scandariato et al. 2011)) indicate that the typical extinction (assuming R_V=3.1) for stars in the ONC is $A_V \sim 2$. Plugging this value in Eq. 3.2, having $a_J^{3.1}$=0.28, $a_H^{3.1}$=0.18 and $a_{K_S}^{3.1}$=0.12, we derive that for R_V=5.5 the extinction-corrected *H*-magnitudes are typically brighter by ∼0.1, while the *J*-*H* and *H*-K_S colors are typically bluer by ∼0.07 and ∼0.04 respectively.

We can validate this estimate by investigating how our results vary with increasing R_V considering the subsample of stars of D10 (corresponding to ∼92% of our collected catalog down to spectral type M7), for which the authors provide the stellar parameters derived R_V=5.5. We do not include the list of stars of R07 and S04 in this analysis as the authors do not derive the stellar parameters assuming R_V =5.5. By consequence, we can derive the ΔX corrections only down to the M7 spectral type.

The new set is analyzed following the same strategy described in Sect. 3.2. Using the new set of the stellar parameters L, A_V and l, we compile a master catalog of 342 stars and derive new corrections to the NIR synthetic colors (Table 3.1). In Fig. 3.5 we compare these new corrections to the ones obtained with R_V=3.1. As anticipated above, the new corrections lead to corrected colors slightly bluer and *H*-magnitudes slightly brighter, roughly confirming our previous expectations.

Mass estimate

Our analysis of the synthetic photometry has been based on a particular family of evolutionary models, DM98, used to derive the stellar mass and therefore the surface gravity. This assumption may affect especially the NIR continuum of M-type stars, shaped by the water vapor opacity profile (Allard et al. 2010), which is sensitive to surface gravity. In order to reduce the uncertainties in $\log g$ related to the assumption of a particular model, in Sect. 3.3 we increased the DM98 track-predicted masses by ∼20%, as indicated by Hillenbrand & White (2004). Since mass and surface gravity are linearly correlated, this correction increases $\log g$ by ∼0.1 dex with respect to the value derived using the DM98 model masses at face value.

To further investigate the effects of surface gravity in our analysis, in Fig. 3.6 we compare the synthetic near-IR spectra of an M1 and M7 star both 1Myr old according to DM98. The dashed and solid lines show the spectra before and after the mass correction, respectively. For the M7 star the correction has no impact. On the other hand, the HK_S continuum of the M1 star decreases by $\lesssim$0.01 dex,

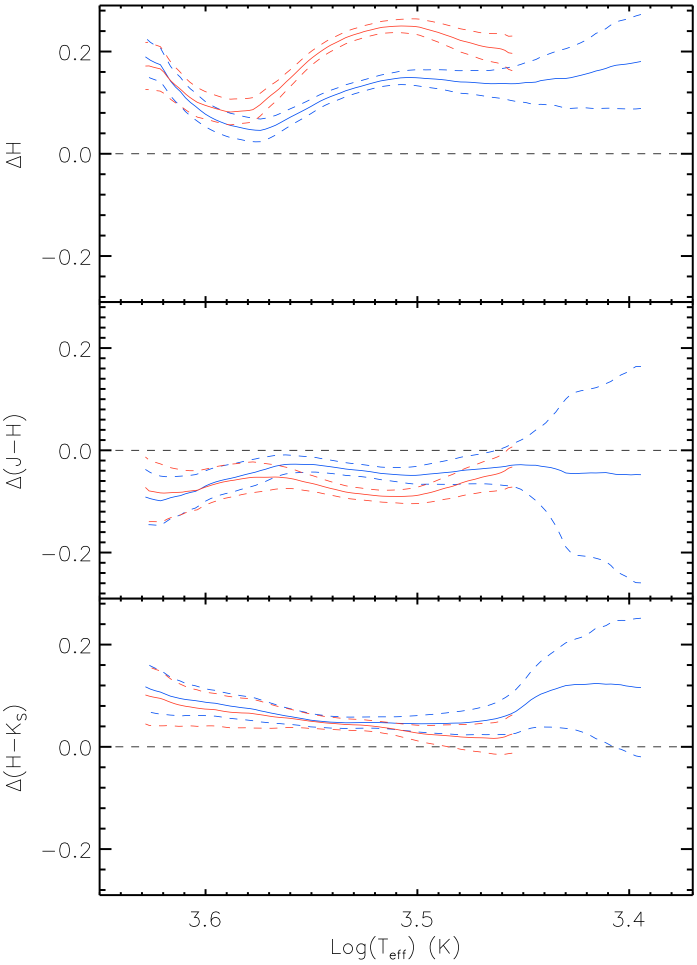

Figure 3.5: Comparison of the ΔH, $\Delta(J-H)$ and $\Delta(H-K_S)$ corrections (from top to bottom respectively) derived assuming R_V=3.1 (blue lines) ans R_V=5.5 (red lines). The dashed lines represent the 1-σ confidence bands.

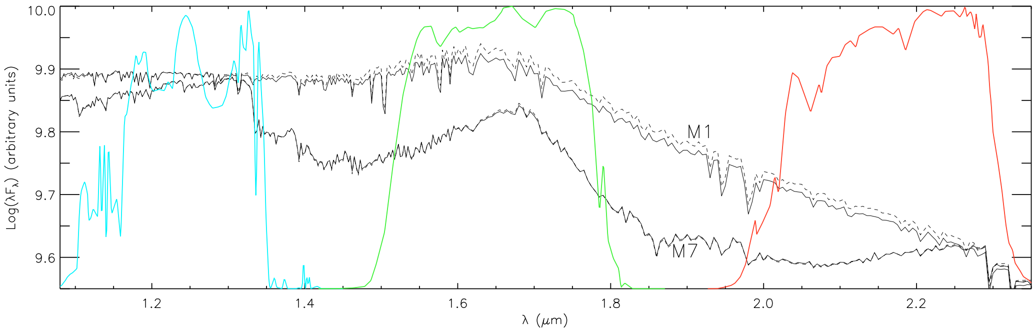

Figure 3.6: Synthetic spectra for a M1 and a M7 star (top and bottom spectrum respectively) as provided by Allard et al. (2010). For each spectral type, the dashed line shows the spectrum computed with $\log g$ provided by the 1 Myr old model of DM98 (3.63 and 3.33 respectively), while the solid line shows the same spectra with $\log g$ artificially increased by 0.1 dex (for the M7 star the two spectra overlap). The blue, green and red lines stand for the transmission curves of the 2MASS JHK_S filters respectively. We find that the M7 spectrum weakly depends on $\log g$. On the contrary, for the M1 star the continuum spectrum in the HK_S bands decreases with increasing $\log g$. No changes are seen in the J band.

while no significant changes are present in the J band. In terms of synthetic photometry, the increase of surface gravity leads to fainter HK_S magnitude and bluer J-H colors by $\lesssim$0.02 magnitudes. Thus, fine tuning the $\log g$ values has a small effect on the synthetic photometry and, by consequence, the differences between predicted and observed photospheric colors are not dominated by the uncertainties in the evolutionary models, as long as the track-predicted masses deviate by $\lesssim$20%.

If using different recipes for deriving the stellar mass, and therefore surface gravity, has a negligible effect on the synthetic spectra of PMS stars, the discrepancies we found between model predictions and extinction-corrected photometry (Table 3.1) must be largely attributed to the residual uncertainties of the atmospheric models of Allard et al. (2010) in the NIR.

3.4 The empirical NIR isochrone of the ONC

By taking advantage of the master catalog of ONC stars compiled in Sect. 3.1, we can empirically derive a representative NIR isochrone of the cluster. assuming both R_V=3.1 and R_V=5.5. In Fig. 3.7 we show the extinction-corrected H, J-H and H-K_S colors of the sample of stars analyzed in Sect. 3.2 as functions

Table 3.2: Empirical intrinsic colors for LMSs and BDs in the ONC.

		R_V=3.1			R_V=5.5		
SpT	$T_{\rm eff}{}^a$	H	J-H	H-K_S	H	J-H	H-K_S
M8.5	2555	14.96	0.54	0.48	-	-	-
M8	2710	14.50	0.56	0.44	-	-	-
M7	2880	13.23	0.60	0.35	12.90	0.61	0.28
M6	2990	12.95	0.61	0.31	12.69	0.62	0.27
M5	3125	12.71	0.63	0.29	12.35	0.63	0.26
M4	3270	12.23	0.68	0.27	11.97	0.67	0.25
M3	3415	11.88	0.73	0.25	11.74	0.70	0.24
M2	3560	11.63	0.76	0.24	11.51	0.74	0.24
M1	3705	11.30	0.78	0.24	11.14	0.77	0.22
M0	3850	11.10	0.77	0.24	10.89	0.76	0.22
K8	3965	11.02	0.75	0.24	10.79	0.74	0.22
K7	4060	10.92	0.72	0.23	10.70	0.72	0.21
K6	4154	10.82	0.70	0.24	10.57	0.70	0.22

Notes. [a] Temperature scale of Luhman et al. (2003).

of the effective temperature. Following the same strategy adopted in Sect. 3.3, we smoothly fit the intrinsic colors from $T_{\rm eff}\sim$2500 K up to $T_{\rm eff}\sim$4200 K using a robust outlier-resistant algorithm. The derived intrinsic NIR colors of the ONC are given in Table 3.2. As discussed in Sect. 3.3.1, assuming R_V=5.5 results in slightly brighter and bluer colors than those derived with R_V=3.1.

The magnitudes and colors presented in Table 3.2 represent our best estimate of the locus in the NIR CMDs along which the ONC stars should be located if one removes the effects of extinction and NIR excess. We underline that this is an average, ideal locus. The ONC population is spread across the HRD (see e.g. Fig. 3.1) by about ∼1.5 dex in luminosity, partially due to effects like stellar variability and unresolved companions, but also to an intrinsic age spread (Hillenbrand 2009; Reggiani et al. 2011). The observed luminosity spread, corresponding to a ∼3.5 magnitude spread, persists in the top panel of Fig. 3.7. Our empirical H magnitudes, therefore, may only be appropriate for an average ONC isochrone. On the other hand, we have seen that the differences in luminosity, while leading to differences is surface gravity, have small influence on the photospheric colors (Sect. 3.3.1). For this reason the average NIR colors in Fig. 3.7 are better constrained than the absolute magnitudes. One can therefore assume that our empirical, average *colors* properly describe those of the ONC sources, and of their corresponding isochronal sequences.

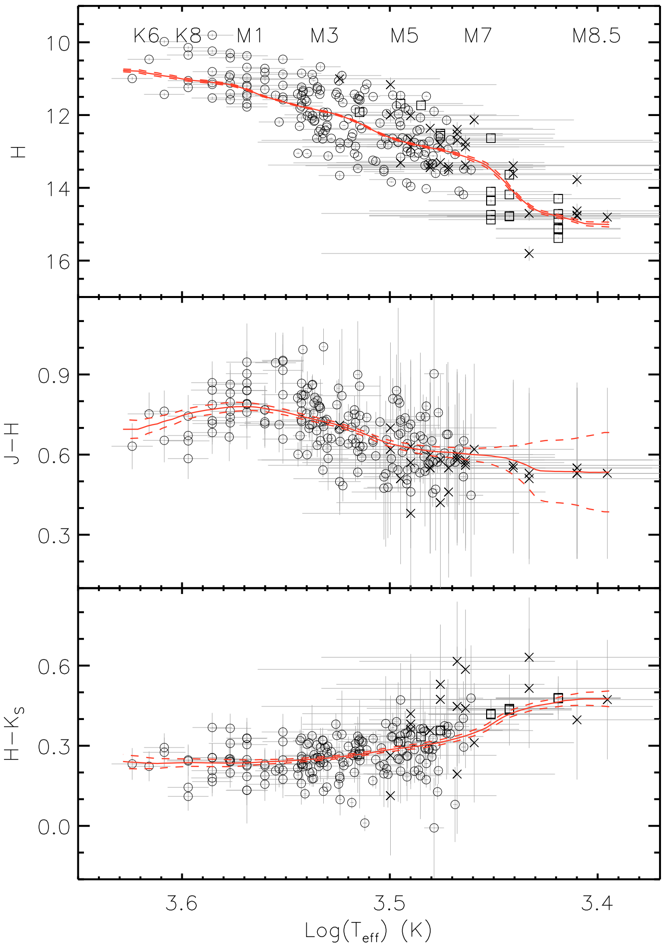

Figure 3.7: Intrinsic *H*, *J*-*H* and *H*-K_S colors of stars in the ONC as function of T_{eff} (from top to bottom respectively). Circles, crosses and squares represent stars with spectral types provided by Da Rio et al. (2011), R07 and S04 respectively, while the error bars take into account the uncertainties in both the extinction-corrected photometry and the synthetic photometry. Red solid lines show our smooth outlier-resistant fits, together with the corresponding 1-σ confidence bands (dashed red lines).

3.5 Comparison with other models and validation

3.5.1 Magnitudes and colors vs. temperature

As anticipated in the introduction of this chapter, current evolutionary models provide different predictions for the position of the PMS isochrones and evolutionary tracks in the HRD, especially at sub-solar masses and young ages (Hillenbrand et al. 2008). This is a consequence of the difficulties in adequately modeling the convective equilibrium in the interior of fast rotating sub-solar young stars, The inconsistencies between the various sets of models generally persist when they are converted into magnitudes and colors, for a direct comparison with the data in the CMDs (see Figs. 3.9–3.10). As discussed in Sect. 3.3.1, the synthetic magnitudes depend weakly on the exact value of the mass associated to a given $T_{\rm eff}$ and therefore these discrepancies are almost entirely a consequence of the different luminosities predicted by theoretical model, for any particular $T_{\rm eff}$.

To illustrate this point, we have computed synthetic photometry for the 1 Myr theoretical isochrones of DM98, and the 2 Myr isochrones of BCAH98 and SDF00, which are adequate to represent the typical ONC population (see D10). We used the synthetic spectra of Allard et al. (2010) and the empirical corrections to the atmospheric model derived in Sect. 3.3. In Fig. 3.8 we plot H, (J-H) and (H-K_S) as functions of $T_{\rm eff}$ for the various models.

Figure 3.8 shows that there are significant differences in the H–$T_{\rm eff}$ relation. The BCAH98 curve is consistently steeper than the curves of the other models: it is $\sim$1 mag brighter than the isochrone of DM98 for spectral types earlier than M2, and $\gtrsim$1 magnitude fainter for spectral types M5-M7. Smaller differences are also present between the DM98 and SDF00 isochrones in the overlapping spectral range, with the noticeable exception that the latter shows a bump in luminosity for M5 stars. At very late spectral types, the DM98 model steeply decreases reconciling with the BCHA98 model. This because the DM98 isochrones drastically turn down in luminosity for $\log T_{\rm eff} \lesssim 3.45$, as shown in Fig. 3.1. As discussed by Hillenbrand et al. (2008), this drop is a common feature of the PMS evolutionary models, which tend to under-predict the intrinsic luminosities of low-mass stars.

Figure 3.8 also shows that despite the discrepancies between the various H–

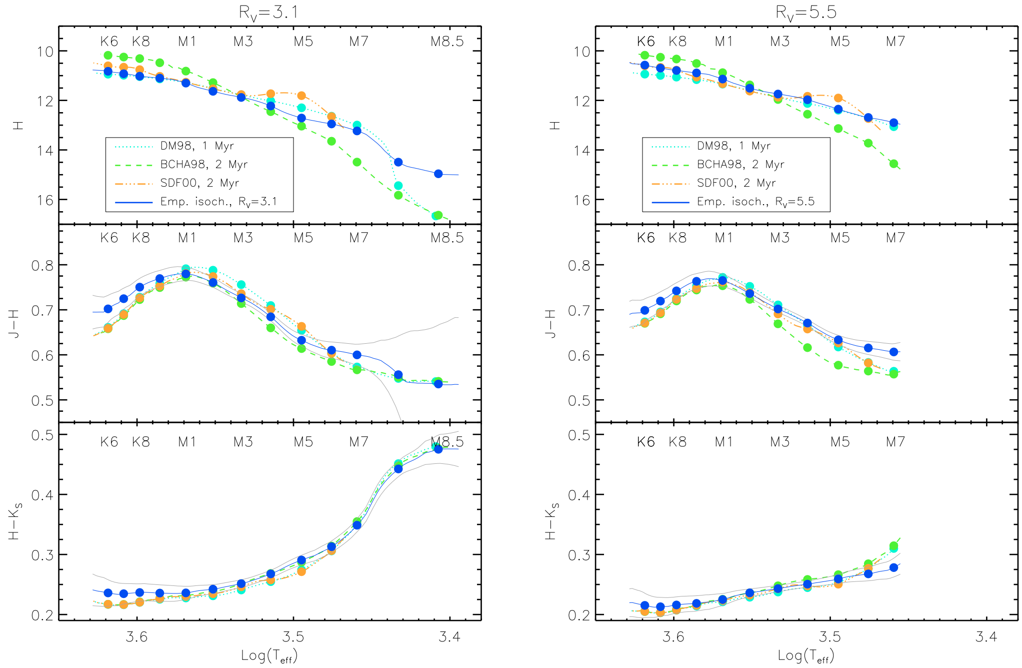

Figure 3.8: H, (J-H) and (H-K_S) as functions of $T_{\rm eff}$ (from top to bottom), assuming R_V=3.1 (left column) and R_V=5.5 (right column). At the top of each panel we report the spectral type–$T_{\rm eff}$ conversion of Luhman et al. (2003). In each panel, dots represent the spectral types listed in Table 3.2 for which the correction is available. The thin gray solid lines represent the uncertainties on our derived empirical colors, as shown in Fig. 3.7. The uncertainties on the empirical H-magnitudes (top panels) are >10 times smaller than the vertical scale, and therefore not visible.

$T_{\rm eff}$ relations, the situation is much better in what concerns synthetic colors. In this case, model predictions are consistent within ∼0.05 mag, confirming that the discrepancies are mainly due to different predictions of the intrinsic stellar luminosity, which reflects in the predicted magnitudes but not in the colors.

Our empirical H, (J-H) and (H-K_S) are also shown in Fig. 3.8 as functions of $T_{\rm eff}$. The H–$T_{\rm eff}$ curve provides higher fluxes for spectral types ≥M7 than the BCAH98 and DM98 models. In general, no model provides H magnitudes nicely consistent with our empirical curve, but the 1 Myr old model of DM98 closely follows our derived H–$T_{\rm eff}$ relation for spectral types earlier than M7. On the other hand, our empirical colors are fully consistent, within the error bars, with the model predictions.

3.5.2 Color-Magnitude Diagrams

Figures 3.9–3.10 summarize these relations in the CMDs, together with the density distribution of the extinction-corrected photometry of our sample of stars, relative to the cases with R_V=3.1 and R_V=5.5 respectively. The agreement between the various isochrones is generally poor, as the predicted magnitudes may differ by up to 1 mag.

The synthetic colors corrected for the inaccuracies of the atmospheric models (Sect. 3.3, solid lines in Figures 3.9–3.10) improve over the original theoretical predictions (dashed lines), tracing more closely the color distribution of the ONC sources in the CMDs. This correction, however, does not fix the systematic under-prediction of absolute magnitudes. Our empirical isochrone, derived from a subset of these data, also traces the color distributions of the sources in both CMDs and, for the case R_V=3.1, provides brighter H magnitudes for late type stars. Unfortunately, for the case R_V=5.5 no correction is available for spectral types later than M7.

3.6 Summary

In this paper we have accurately analyzed a sample of ∼300 stars with measured temperatures, luminosities and photospheric NIR photometry as a benchmark for current atmospheric and evolutionary models for low-mass PMS stars and BDs.

We have compared the extinction-corrected photometry to the expected photometry provided by the template spectra of Allard et al. (2010), finding that major improvements have been done in the synthesis of theoretical spectra with respect to previous releases from the same group. Nonetheless, we obtain indications on the lack of opacity in the H-band, likely due to the improper treatment of the water vapor absorption profile. We thus propose the set of empirical corrections listed in Table 3.1, to be regarded as additive terms to the synthetic NIR colors. These corrections are weakly influenced by the $\log g$ assumed to derive synthetic colors.

We also analyzed the same sample of stars in order to derive the average isochrone of the ONC, reported in Table 3.2. The analyzed sample of stars show a magnitude spread of the order of ∼3.5 mag, consistent to the ∼1.5 dex luminosity spread reported in previous study of the ONC. This spread does not

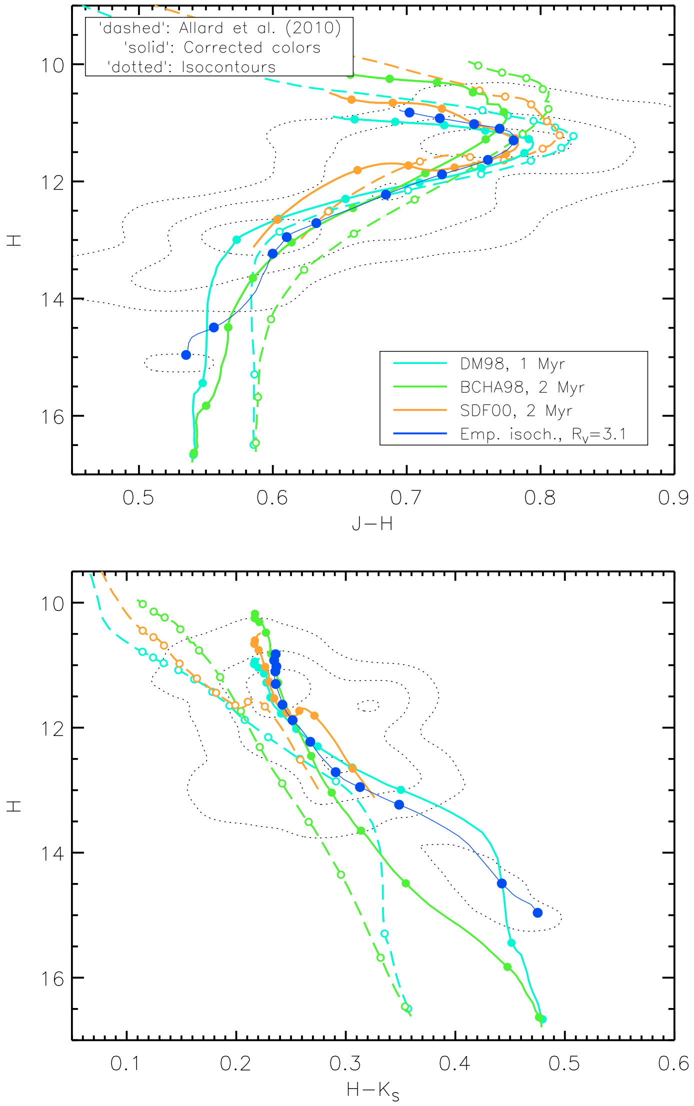

Figure 3.9: (H,J-H) and (H,H-K_S) CMDs (top and bottom panel respectively) of the ONC, compared to the 1 Myr old isochrone model of DM98 (cyan line), the 2 Myr old isochrone of Baraffe et al. (1998) (green line) and the 2 Myr old isochrone Siess et al. (2000) (green line). Synthetic photometry for these models has been computed using the grid of atmospheres provided by Allard et al. (2010) (in dashes) and then corrected using the corrections in Table 3.1 (solid lines), assuming R_V=3.1. Dots mark the position of the spectral types listed in Table 3.2 along the isochrones (from K6 to M8.5 with increasing magnitude, from K6 to M6 for the model of SDF00). The dotted lines show the iso-density contours for the analyzed stellar sample.

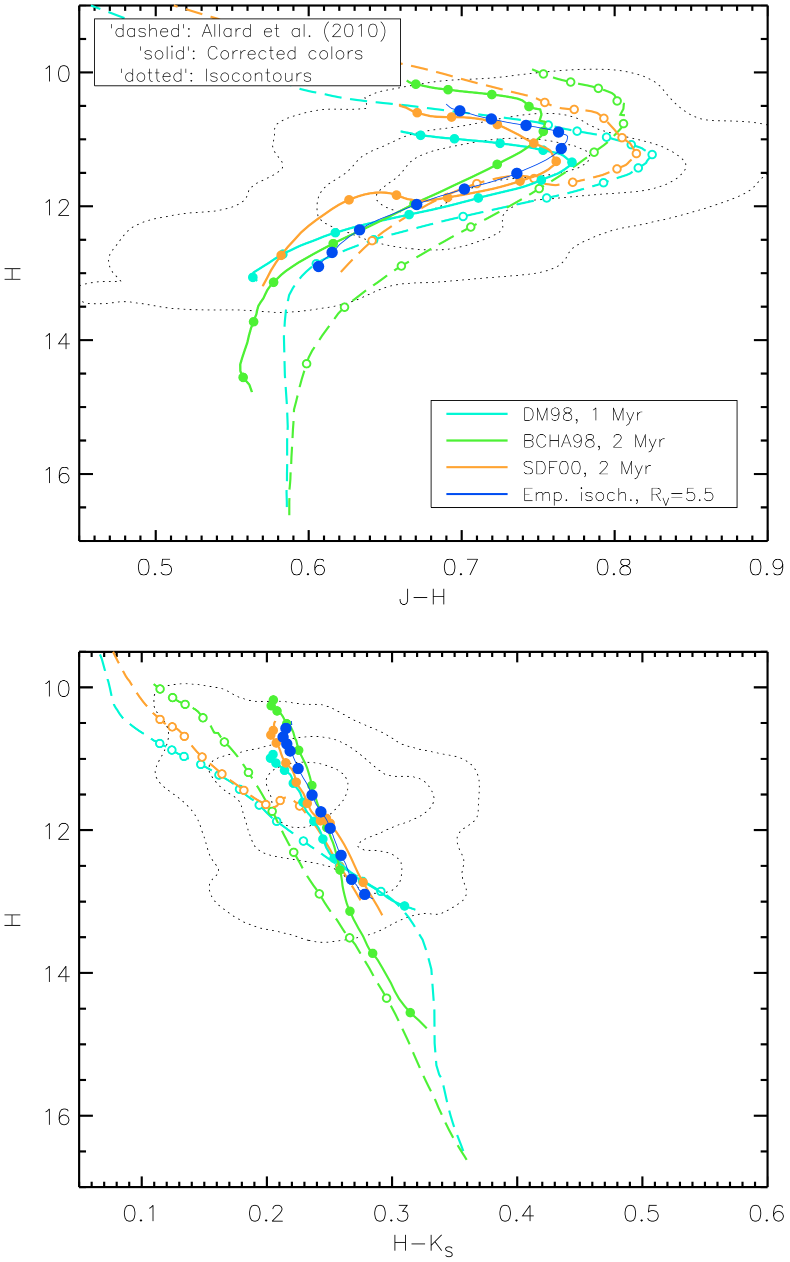

Figure 3.10: Same as in Fig. 3.9, for the case R_V=5.5.

allow us to constrain the magnitude scale of the ONC isochrone. On the other hand, the *J*-*H* and *H*-K_S colors weakly depend on the photospheric luminosity, and are well constrained by our statistical analysis.

Comparing our empirical isochrone to current theoretical models, we find that there is generally good agreement to the 1 Myr old model of DM98 and, to some extent, the 2 Myr old model of SDF00, both in colors and in magnitude scale. On the other hand, we find indications that the PMS isochrones of BCAH98 provide $T_{\rm eff}$–$\log L$ relations too steep compared to our observational data. The same is true for the DM98 evolutionary model at very late types.

The empirical NIR colors we have derived, in the 2MASS system, can be readily converted to other photometric systems using the prescriptions at http://www.ipac.caltech.edu/2mass/releases/allsky/doc/sec6_4b.html. Since low-mass stars slowly evolve in the HRD at very early stages, our empirical colors can conveniently be used as the intrinsic colors of young ($age \lesssim 5$ Myr) stellar clusters to derive NIR excess and extinction of individual stars.

Chapter 4

The NIR excess of T Tauri stars in the ONC

Young PMS stars often show ultraviolet, optical and infrared excesses that can dominate photospheric emission. It is widely accepted that these excesses are produced by various mechanisms involving the presence of a dusty disk around an accreting stellar object (Kenyon & Hartmann 1987; Calvet et al. 1991; Meyer et al. 1997, MCH97 hereafter).

Due to the large wavelength range spanned by these flux excesses, it is difficult to find a photometric band immune from contamination by non- emission. It is often assumed that the J magnitude provides the best approximation of the photospheric flux and, for this reason, it has been used to derive intrinsic magnitudes (e.g. Kenyon & Hartmann 1995; Meyer 1996; Lucas & Roche 2000). On the other hand, MCH97 and Hillenbrand et al. (1998), using Calvet et al. (1991, 1992) accretion disks models to compute a grid of star+disk spectra for T Tauri stars, found that the NIR SEDs can be contaminated by the presence of a disk, either passive or accreting, up to a few tenths of magnitude. This result, theoretically anticipated by Kenyon & Hartmann (1990), has been observationally confirmed by Cieza et al. (2005) and Fischer et al. (2011), who find that J excesses may be due to disk emission rather than the tail of the accretion SED. Consequently, normalizing the observed fluxes to the J-fluxes may lead to systematic overestimates of the bolometric luminosity of the stars, with a consequent underestimate of the age derived by placing stars in the HRD.

MCH97 (see also Meyer 1996) analyze the NIR colors of a sample of 30 CTTSs and 40 Weak-emission T Tauri Stars (WTTSs) in the Taurus region, with spectro-photometric observations in the $RIJHK$ bands. They find that WTTSs show colors consistent with normal main sequence stars, while CTTSs, by virtue of circumstellar activity, occupy a locus in the extinction-corrected (J-H,H-K_S) diagram described by the equation $(J-H) = (0.52 \pm 0.06) + (0.58 \pm 0.11) \cdot (H-K)$, which converts to

$$J - H = (0.54 \pm 0.07) + (0.63 \pm 0.12) \cdot (H - K_S) \tag{4.1}$$

in the 2MASS photometric system (Carpenter 2001).

The introduction of this locus in the (J-H,H-K_S) diagram identifies two regions (Fig. 4.1): in region II colors are consistent with photospheres extincted by interstellar medium, while region I contains the extincted photometry of CTTSs with strong NIR excess. In order to derive interstellar extinction of young stars with evident NIR excesses, many authors (e.g. Meyer 1996; Carpenter et al. 1997; Briceño et al. 2002; Muench et al. 2002; Luhman et al. 2003; Scandariato et al. 2011) shift the stars back to the CTTSs locus along a line parallel to the extinction direction.

While taking into account the presence of NIR excess, this procedure is not definitive in correcting the biases introduced by the excess itself: PMS sources may have indeed photometry compatible with interstellar extinction while still suffering from a non-negligible amount of (J-H) excess. For example, let's consider a T Tauri star with spectral type K3 ($T_{\rm eff} \sim 4500K$, the plain star symbol in Fig. 4.1) which, by virtue of its infrared excess, is shifted along the CTTSs locus following the dashed line, brightening and reddening the photometry such to reach the black dot in the diagram. The observed photometry of such a system would be located in region II, thus it would not show any evidence of circumstellar infrared excess.

In such a case, the whole color excess, which is $\Delta(J-H) \sim 0.3$ for the star in Fig. 4.1, would be attributed to interstellar extinction. Using the extinction law provided by Cardelli et al. (1989), we derive that it corresponds to A_V ~3. Since the extinction-correction consists in subtracting the interstellar absorption from the observed photometry, the star in the figure would be erroneously assigned a magnitude too bright. In summary, this procedure would erroneously overestimates the intrinsic flux of late-type PMS stars (~one order of magnitude for the case in Fig. 4.1), and this generally leads to the overestimate of the mass and the underestimate of the age when they are placed in the HRD.

The goal of this chapter is to use the extensive set of spectral types and photometric data available for the ONC in order to investigate the presence of circumstellar disks and to study their frequency depending on various stellar

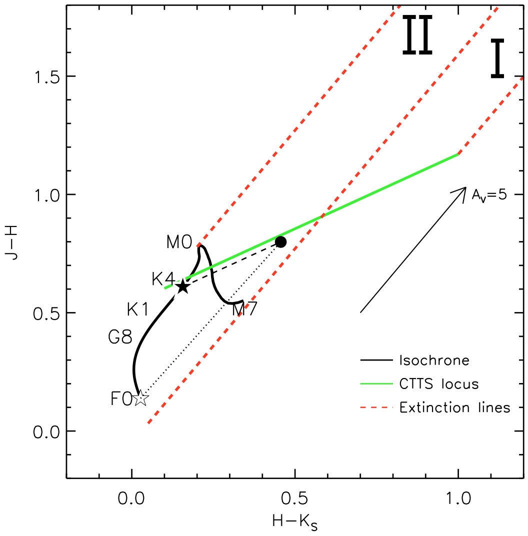

Figure 4.1: (*J*-*H*,*H*-K_S) 2CD in the 2MASS photometric system of the locus of CTTSs provided by MCH97 (green line). The black solid line represents the combination of the cluster isochrone we derive in Chapter 3 (up to spectral type K6) and Siess et al. (2000) (for earlier types). The red dashed lines are meant to redden the loci introduced above as a consequence of stellar extinction (the $A_V = 5$ extinction vector is also indicated). Meyer (1996) identifies two regions in this diagram: region I, populated by sources whose photometry is compatible with reddened stellar photospheres, and region II, populated by sources whose photometry shows evidences of infrared excesses. It is also shown the case of a reddened K4 CTTS discussed in the text. The plain star symbol is the position of the K4 star along the isochrone, which is reddened by virtue of infrared color excess (parallel to the CTTSs locus) towards the black dot. The open star symbol represent the intrinsic photometry recovered after correction for extinction.

parameters, such as mass and age. In particular, we take advantage of the empirical isochrone for the ONC stars derived in Chapter 3 in order to accurately disentangle the photospheric and circumstellar contribution in the observed photometry. In Sect. 4.1 we present the selection of our sample of stars. In Sect. 4.2 we define our diagnostic in detecting circumstellar NIR excess, and we discuss the observed NIR excess of stars with and without accretion evidences. Finally, in Sect. 4.3 we discuss the observed frequency of disks depending on the stellar mass, age and projected distance from the cluster center.

4.1 The data set

The large dataset of Robberto et al. (2010) allows to revisit the effects of disk emission and accretion luminosity on NIR photometry with much stronger statistical power than previous surveys. In particular, we analyze the cross-matched sample of stars with WFI and ISPI *simultaneous* photometry assembled in Sect. 3.1.

To avoid cases of unresolved multiple systems, we check that (1) the stars do not show any infrared companion within $2''$ (or about ∼3 times the FWHM of the PSF); and (2) they appear as isolated stars in the ∼50 mas pixel-scale HST/ACS optical images taken for the Treasury Program on the Orion Nebula Cluster. This minimizes the chances that our infrared photometry is contaminated by brilliant close-by neighbors.

Our final catalog contains 705 stars with effective temperature, photospheric luminosity, accretion luminosity and extinction, together with simultaneous JHK_S photometry from the ISPI catalog.

Moreover, having temperatures and luminosities, we place the stars in the HRD (Fig. 4.2) deriving masses and ages through a comparison of their position with the evolutionary model provided by D'Antona & Mazzitelli (1997, 1998). This allows us to compute synthetic NIR infrared photometry using the atmospheric grid of Allard et al. (2010). We also empirically correct synthetic colors for the inaccuracies of the atmospheric models based on the results discussed in Sect. 3.3, thus deriving accurate estimates of the photospheric colors.

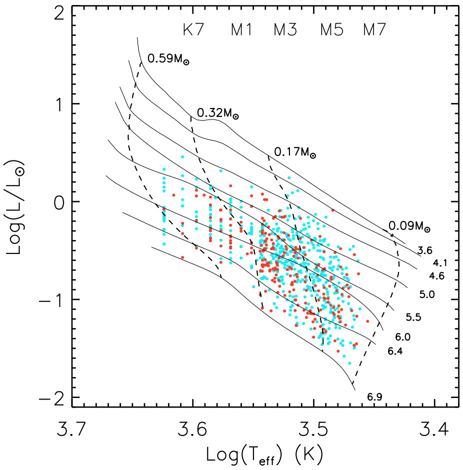

Figure 4.2: HRD of our list of 705 stars superimposed to the evolutionary model computed by D'Antona & Mazzitelli (1997, 1998). Solid lines represent the isochrone at different ages (the logarithmic age in year is indicated), while dashed lines show the tracks at fixed mass. Cyan and red dots stand for stars with and without evidences of accretion respectively (see Sect. 4.2). In the upper part of the diagram we report the $T_{\rm eff}$–spectral type conversion of Luhman et al. (2003) for late–K and M types.

4.2 Observational evidences of NIR excess

In Sect. 4.1 we compile a list of ONC members with observationally-derived stellar parameters, together with observed, extinction-corrected and photospheric NIR photometry. In order to discriminate non-accreting against accreting systems, we now define two subsamples of stars based on the presence of ongoing accretion, based on the parameter l (Sect. 3.2.2). The subsample of 225 stars with l <-6 is assumed to lack evidence of accretion; consistently, we expect their infrared excesses, if present, to be likely due to emission from a passive circumstellar disk. Viceversa, the remaining 528 stars are likely accreting stars (l >-6). Their infrared excess will be affected by the extra contribution due to the accretion luminosity.

The extinction-corrected (J-H,H-K_S) 2CDs for the two samples of stars are shown in Fig. 4.3. These diagrams show that the extinction-corrected photometries occupy an extended region roughly elongated along the CTTSs locus of MCH97. As indicated by the typical error bars shown in each plot, the spread of the regions cannot be entirely attributed to photometric errors, but it likely reflects a real distribution of stars in the diagram.

In particular, after correction for interstellar extinction, the majority of

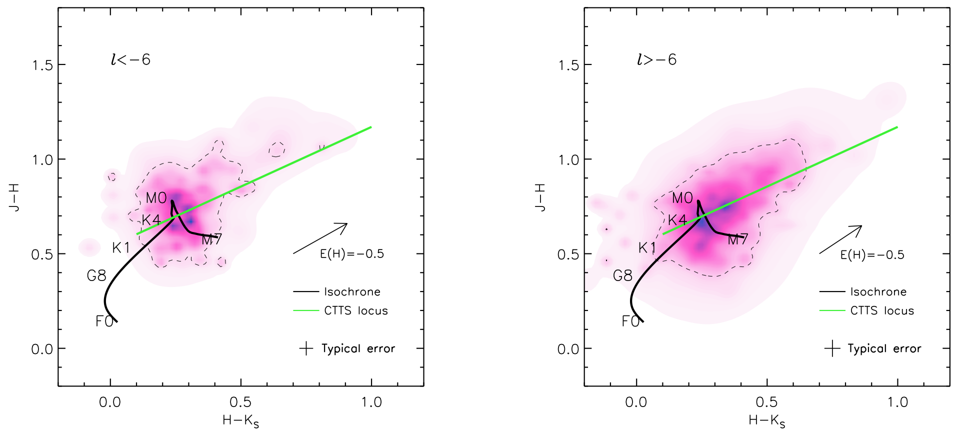

Figure 4.3: Extinction-corrected (*J*-*H*,*H*-K_S) diagram of the samples of stars without accretion evidences (i.e. l <-6, left panel) and with signatures of accretion (l >-6, right panel). The black solid line represents the cluster isochrone, while the green line is the CTTSs locus derived by MCH97. The extinction lines are shown in red dashes. In these diagrams each star is represented as a 2D gaussian probability distribution whose widths are determined by the uncertainties on the two colors. The shaded area is the total probability distribution of the sample, whose peak is coded in blue. In each plot, the black dashed contour encloses the 75% probability around the peak, and it shows that our extinction-corrected photometry is compatible with photospheres later than G0 plus some infrared excess as predicted by MCH97. The $E(H)$ vector shows the reddening direction, depending on the presence of ongoing accretion (see Sect. 4.2.1 and Sect. 4.2.2 for details).

sources show photometry compatible with bare photospheres plus a contribution of infrared excess, which shifts the star along the direction roughly parallel to the CTTSs locus (Eq. 4.1). It is also noteworthy that accreting stars are more elongated in the 2CD compared to the sample of non-accreting stars. As we will discuss in Sect. 4.2.3, this is indicative of the fact that the presence of ongoing accretion increases the infrared emission of circumstellar matter.

In order to investigate the observational properties of stars with infrared excess, we now combine extinction-corrected and photospheric magnitudes deriving the *magnitude excess*

$$E(m) = m_{ec} - m_p, \tag{4.2}$$

where m stands for any of the JHK_S bands, m_{ec} is the extinction-corrected magnitude and m_p is the photospheric magnitude.The magnitude excess of passive and actively accreting stars are discussed in Sect. 4.2.1 and Sect. 4.2.2 respectively.

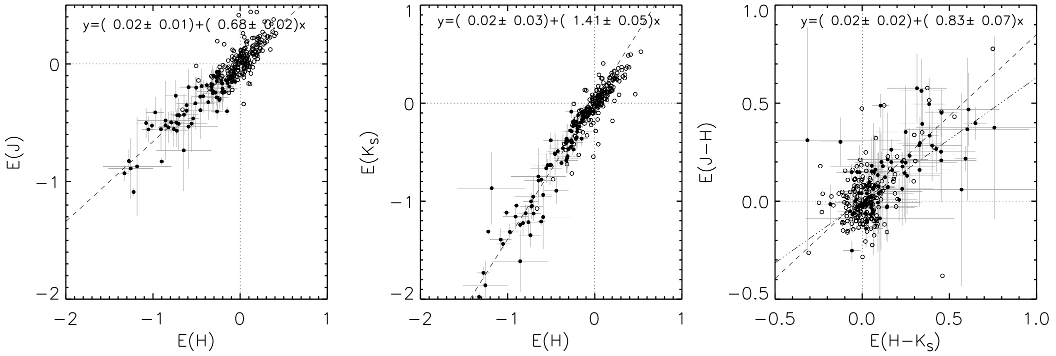

Figure 4.4: $E(J) - E(H)$ diagram (left panel), $E(K_S) - E(H)$ diagram (central panel) and $E(J - H) - E(H - K_S)$ diagram (left panel) for the sample of stars with no accretion evidences. In each diagram, we show our best fit in dashes. The fitted sample is shown as filled dots with the corresponding error bars, while open circles represent stars which do not meet our selection criterion and, by consequence, are not included in the fit. The dashed-dotted line in the right panel represents the CTTSs locus provided by MCH97 converted to the 2MASS photometric system. The dotted lines in each plot mark the axes positions.

4.2.1 Stars without evidence for accretion

Figure 4.4 shows the $E(J) - E(H)$ diagram and the $E(K_S) - E(H)$ diagram (left and central panel respectively) for the subsample of non-accreting stars. These diagrams show that we typically find negative $E(J)$, $E(H)$ and $E(K_S)$ excesses. Accordingly to our definition in Eq. 4.2, this result indicates that the observed fluxes are greater than the corresponding synthetic fluxes, i.e. we find *flux excesses.*

Figure 4.4 shows that most stars in this sample have weak evidence of NIR excess: in particular, we find that ∼90% of stars show $E(H)$ >-0.5. In order to better correlate the magnitude excesses, we consider only those stars in the excess diagrams with magnitude excesses above one sigma (i.e. $-E(m) > \sigma_{E(m)}$) simultaneously in the JHK_S bands. The 79 stars satisfying our criterion are fitted with a custom outlier-resistant algorithm accounting for the uncertainties on both variables: our best fits are reported in Eqs. 4.3–4.4.

$$E(J) = (0.02 \pm 0.01) + (0.68 \pm 0.02)E(H); \tag{4.3}$$

$$E(K_S) = (0.02 \pm 0.03) + (1.41 \pm 0.05)E(H); \tag{4.4}$$

Since infrared excesses of non-accreting stars arise from circumstellar disks (or circumstellar material in general), we would expect to find null $E(J)$ and

$E(K_S)$ corresponding to $E(H)$=0. This is confirmed, within the errors, by the intercepts in Eqs. 4.3–4.4. For the sake of simplicity, we thus artificially set the intercepts to zero in the following analysis.

To derive the correlation between the excess in the three bands, we combine Eqs. 4.3–4.4 to derive

$$\begin{aligned} E(J-H) &= E(J)-E(H) = ((0.68\pm0.02)-1)E(H) = \\ &= (-0.32\pm0.02)E(H); \qquad (4.5) \\ E(H-K_S) &= E(H)-E(K_S) = (1-(1.41\pm0.05))E(H) = \\ &= (-0.41\pm0.05)E(H). \qquad (4.6) \end{aligned}$$

Deriving $E(H)$ from Eq. 4.6 and substituting in Eq. 4.5 we obtain

$$E(J-H) = (0.78\pm0.04)E(H-K_S). \tag{4.7}$$

This correlation is confirmed, within the errors, by the linear fit of the $E(J-H)-E(H-K_S)$ colors of the excess in the corresponding diagram (right panel in Fig. 4.4). The linear correlation in this diagram is less evident than in the two magnitude excess diagrams, due to the fact that (1) the uncertainties on colors, computed as propagation of the uncertainties on magnitude excesses, are larger and (2) color excesses span a smaller magnitude range. The linear fit is thus less constrained by our data, while Eq. 4.7 provides a more robust estimate of the correlation between the color excesses. For this reason, in the following analysis we will refer to Eq. 4.7 when discussing the effects of circumstellar disks on the observed colors.

Equations 4.5–4.6 also give a parametrization in $E(H)$ units of the amount of color excess. This allows us to plot in Fig. 4.3 the shift corresponding to a NIR excess of $E(H)$=-0.5

4.2.2 Stars with accretion evidences

Figure 4.5 shows the magnitude excesses diagrams (left and central panel) for the subsample of accreting stars. Outlier-resistant fits performed over the sample of 212 stars with strong evidences of NIR excess (i.e. $-E(m) > \sigma_{E(m)}$ simultaneously in the three JHK_S bands) give the following relations:

$$E(J) = (-0.01\pm0.03) + (0.73\pm0.03)E(H); \tag{4.8}$$

$$E(K_S) = (-0.05\pm0.03) + (1.36\pm0.03)E(H). \tag{4.9}$$

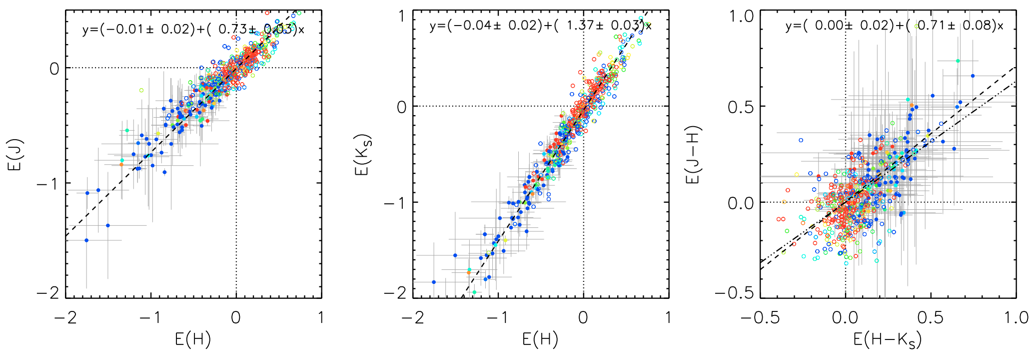

Figure 4.5: $E(J)-E(H)$, $E(H)-E(K_S)$ and $E(J-H)-E(H-K_S)$ diagrams, from left to right respectively, for the 528 stars with l >-6. As in Fig. 4.4, dashed lines represent our best fits, computed over the sample of filled dots (plotted with the error bars), while open dots are not included in the fits. The color scale codes the l parameter, running in the [-6,0] interval from red to blue. The dotted-dashed line in the color excess diagram represent the slope of the CTTSs locus provided by MCH97.

For the same reasons discussed in Sect. 4.2.1, we do not attribute any relevant physical meaning to the intercepts in Eqs. 4.8–4.9, and we artificially set them to zero.

Equations 4.8–4.9 also provide the parametrization of the reddening shift in the NIR 2CD:

$$E(J-H) = (0.76 \pm 0.10) E(H-K_S). \tag{4.10}$$

As in the case of Eq. 4.7, we prefer Eq. 4.10 to the best fit shown in the right panel of Fig. 4.5.

The reddening direction for accreting stars corresponding to $E(H)$=-1 is shown in the right panel of Fig. 4.3.

4.2.3 Discussion

Equations 4.8–4.9, compared to Eqs. 4.3–4.4, suggest that for a given $E(H)$ the magnitude excess $E(J)$ is larger for accreting systems, while we do not find significant differences between the two $E(K_S)$–$E(H)$ relations. This is consistent with the presence of an extra-source with blue *J-H* color.

According to Calvet & Gullbring (1998), the total emission from the accretion column can be well approximated by the superposition of an optically thick emission from the heated photosphere below the shock, and an optically thin emission generated in the infalling flow. The SED of the optically thick emission

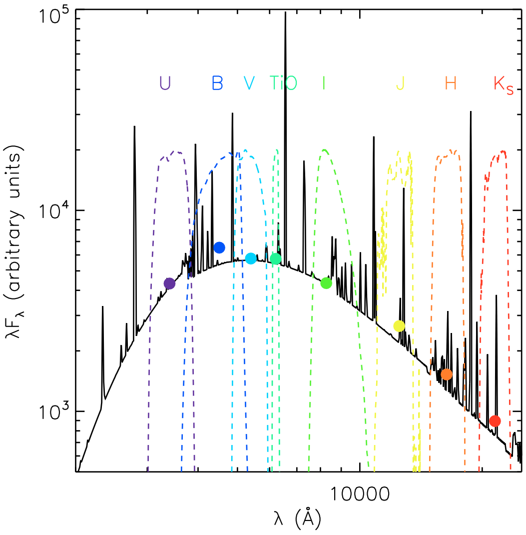

Figure 4.6: Accretion SED computed simulated with *Cloudy*. The WFI *U,B,V,TiO,I* and the 2MASS *JHK$_S$* transmission curves are overplotted as colored dashed lines. The big dots mark the flux densities of the spectrum for the corresponding passbands.

is compatible with a photosphere with $T_{\rm eff}$~6,000-8,000 K, while the optically thin pre-shock column can be modeled by thermal recombination emission. The relative fraction of the two components with respect to the total accretion emission is about 3/4 and 1/4; respectively. We therefore assume for the optically thick emission a black body with $T_{\rm eff}$=7,000 K, whereas for the thin emission we used the version 07:02:01 of the *Cloudy* software, last described by Ferland et al. (1998), to reproduce the spectrum of an optically thin slab (n=10^8 cm^{-3}) also at T=7,000 K. The derived low resolution accretion spectrum is shown in Fig. 4.6, together with the flux densities in the WFI and 2MASS photometric bands.

Let's now assume that the observed SEDs can be modeled as bare photospheres plus contributions from a passive circumstellar disk and the accretion shock. Given these assumptions, we compute the intrinsic photospheric fluxes of PMS stars in the 2,500 K$\lesssim$T$_{ph}$ $\lesssim$5,000 K temperature range, spanned by our selected sample. As suggested by Scandariato et al. (in preparation), we also compute the excesses due to a T$_{disk}$ ~1,600 K circumstellar disk and radiating surface $\Sigma = 10^{22.5}$ cm^2, with grain emissivity $\varepsilon = 2\pi a/\lambda$, where $a = 10^{-5}$ cm is the typical grain radius (Natta & Panagia 1976). Finally, for each synthetic photosphere we compute the *JHK$_S$* flux excesses due to accretion corresponding to $l = -6, -2, -1$ respectively, assuming the accretion SED shown in Fig. 4.6.

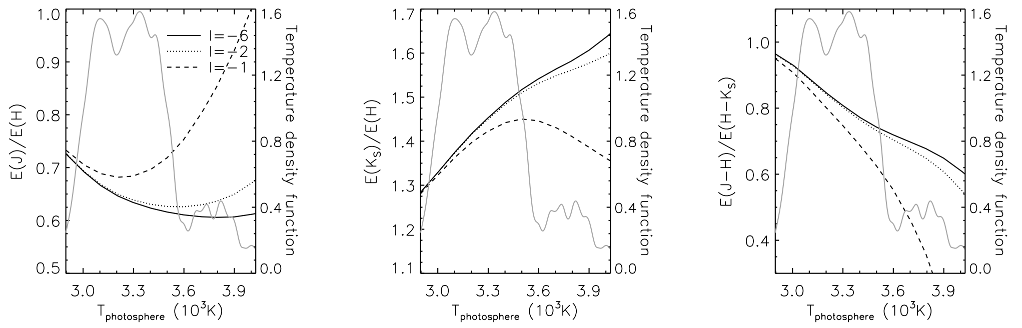

Figure 4.7: Predictions of the magnitude excesses and color excesses correlations as described in the text, for different values of l. In each diagram, the gray solid line represents the distribution function for photospheric temperatures in our analyzed sample. These diagrams show that our model roughly predicts the slopes in Eqs. 4.3–4.7 and Eqs. 4.8–4.10, and also the trend of the slopes with increasing accretion flux excess (i.e. the l parameter).

Converting flux excesses into $E(J), E(H), E(K_S)$ magnitude excesses, this naive model leads to the results shown in Fig. 4.7, where we plot the ratios between the predicted magnitude and color excesses as a function of T_{ph} and l. The predicted ratios, which correspond to the correlation coefficient between magnitude and color excesses in Fig. 4.4 and Fig. 4.5, roughly confirm Eqs. 4.3–4.7 and Eqs. 4.8–4.10. In particular, our model suggests that increasing the contribution from the accretion SED we obtain the following effects:

- the slope in Eq. 4.3 increases, i.e. we expect larger J excesses in the presence of accretion;
- the $E(H)$ and $E(K_S)$ are negligibly affected by the presence of ongoing accretion.

The net effect in terms of color excess is that the slope of the CTTSs locus slightly flattens in the presence of accretion. Broadly speaking, since the accretion SED steeply decreases in the infrared, it compensates the *J-H* color excess from circumstellar disks more than the *H-K_S*, where the disk plays a more important role.

We also remark that the slope of the CTTSs locus of MCH97 (Eq. 4.1) is consistent with the color excess correlation we derive for the samlpe of accreting stars (Eq. 4.10). This is likely due to the fact that the sample of stars analyzed by MCH97 in deriving their locus was made up by 30 CTTSs, i.e. stars actively accreting from their circumstellar disks.

Figure 4.5 shows that we generally observe the largest magnitude excesses corresponding to the largest accretions. This trend is compatible with the scenario depicted above: with the onset of accretion phenomena, an extra-source of radiation contributes to the flux in excess, and its contribution scales with the accretion luminosity l. In the color excess diagram this trend becomes less evident. This is due to the fact that, whilst the internal conversion of mechanical energy in accreting disks enhances the infrared emissivity of circumstellar matter (Hartmann 2009), accretion luminosity and disk emission counteract in terms of NIR colors, having respectively blue and red SEDs. Moreover, since the excess in colors is determined with lower signal-to-noise ratio, the color excess diagram is characterized by larger statistical scatter. Nonetheless, accreting stars still show typically larger displacement in the 2CD compared to non accreting stars (see Fig. 4.3 and the color excess diagrams in Fig. 4.4 and Fig. 4.5). This indicates that the enhancement of NIR emission of the disk has the largest effect on the NIR colors of the excess SED, compared to the blue component introduced by the accretion SED.

Considering that young PMS stars with photometric accretion evidences are bona-fide CTTSs, and conversely disked stars without accretion are bona-fide WTTSs, we obtain (1) the locus of WTTSs in the NIR 2CD; and (2) the update of the slope of the CTTSs locus provided by MCH97, providing greater statistical validity due to the large number of stars in our sample. Most importantly, we also remark the simultaneity of the optical and infrared photometries, which avoids the uncertainties introduced by photometric variability when multi-epoch observations are merged.

4.3 The disk frequency and trends with stellar properties and cluster environment

In this section we describe our methodology for quantifying the fraction of stars with circumstellar activity, given the detection limit for infrared excess introduced in Sect. 4.2.1, i.e. $-E(m) > \sigma_{E(m)}$ simultaneously in the three JHK_S passbands. We also keep the sub-classification in passive and active disks and, for each subsample, we discuss the disk frequencies with stellar mass, stellar age and distance from the cluster center in Sect. 4.3.2, Sect. 4.3.3 and Sect. 4.3.4 respectively.

4.3.1 Detection limit

To study frequencies and trends with stellar and/or cluster parameters, we take the standard approach of counting the number of stars with evidences for NIR excess as a fraction of the total number in our sample.

We now investigate how the observed frequencies are affected by selection effects due to our detection criterion. We show in Fig. 4.8 the uncertainties in the JHK_S excesses as functions of stellar mass. The uncertainties are computed canonically propagating the uncertainties on the observed photometry and the A_V measurements. In these plots we find that the intrinsic increase of photometric uncertainty with magnitudes is counteracted by the fact that, for masses below $M \sim 0.35M_\odot$ (corresponding to $T_{\rm eff}$~3500 K in the 1 Myr old model of DM98), the accuracy on the A_V estimates provided by Da Rio et al. (2011) is greatly improved. The net effect is a flattening of the uncertainty on the extinction-corrected magnitudes and, in turn, on the magnitude excesses.

Moreover, for any given stellar mass, we remark that the uncertainties are increasing functions with decreasing wavelength, following the shallower photometric depth of the ISPI survey with bluer passbands (Robberto et al. 2010). By consequence, most of the stars meeting our simultaneous detection criterion show the minimum SNR in the $E(J)$ magnitude excess, and it follows that $\sigma_{E(J)}$ represents, besides the minus sign, our 1σ-level detection criterion.

Using Eq. 4.3 and Eq. 4.8, we translate our detection limit in the J band in terms of detection limit in the H band, for the passive disks sample and for the accreting disks sample respectively. This represents our $E(H)_{threshold}$ sensitivity limits, i.e. the minimum H-excess we can detect meeting our selection criterion, depending on the stellar mas. This function is shown in the right panel of Fig. 4.8: converting magnitude excess in terms of flux excess (right vertical axis), this plot shows that the minimum flux ratio in the H band we can detect is a function weakly depending on stellar mass. As a matter of fact, for both subsamples the sensitivity limit is at ~8–12% of the corresponding photospheric H-flux over the spanned mass range. Furthermore, by virtue of the consistency between Eq. 4.3 and Eq. 4.8, our sensitivity limits weakly depends on the presence of ongoing accretion.

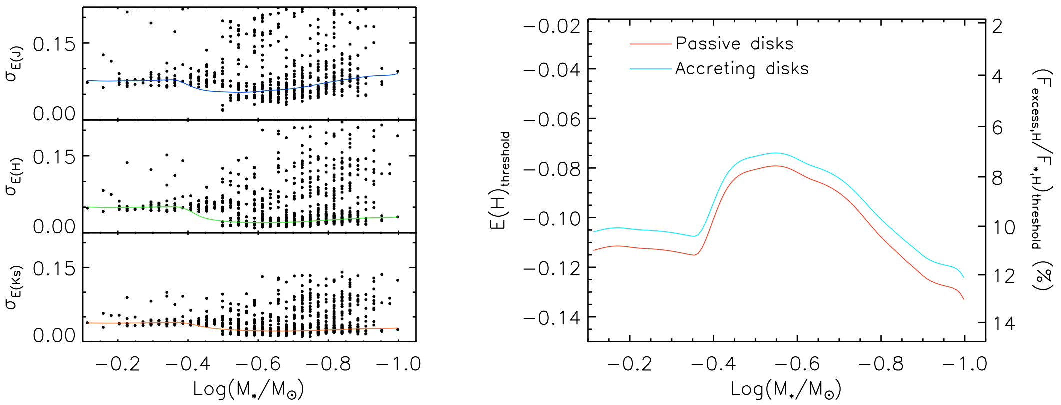

Figure 4.8: *Left panel* – Uncertainties on the magnitude excess measured in the JHK_S bands, from top to bottom respectively. The colored (blue, green and orange respectively) dashed lines show the kernel-regression fit of the data sample. These plots show that the uncertainties generally increase with decreasing stellar masses and with decreasing wavelength. *Right panel* – $E(H)$ magnitude excess threshold as function of stellar mass. The right vertical axis report the conversion from $E(H)$ to the ratio between excess and photospheric fluxes in the H-band. The red and the cyan lines stand for the passive/accreting subsamples respectively. In both cases, the minimum $E(H)$ we can detect is ∼-0.1 and weakly depends on the mass of the central star.

4.3.2 Disk frequency and trend with stellar mass

In Fig. 4.9 we present the observed disk frequency as a function of stellar mass for the two subsamples of stars. For the subsample of passive disks we find that the observed frequency is $\lesssim$40% and does not depend on stellar mass. On the contrary, the frequency of active disks increases from ∼30% up to ∼80% with increasing stellar mass.

In order to investigate whether this difference is a selection effect rather than an intrinsic property of the two subsamples of stars, for the accreting stars we compute the H-excess $E_{acc}(H)$ due to the accretion SED only. In Fig. 4.10 we plot the estimated $E_{acc}(H)$ excess as a function of stellar mass and accretion luminosity, and we find that accretion typically provides excess H-fluxes above our $E(H)$=-0.1 detection limit for $l \gtrsim$-1 and M$\gtrsim$0.2 M$_{\odot}$. The presence of a minimum mass for the detecting accretion in the NIR is most probably due to the fact that the accretion luminosity increases with the mass of the central star. As a matter of fact, assuming that the accretion luminosity is due to conversion of mechanical energy during the mass infall from the inner disk radius R_{disk} to

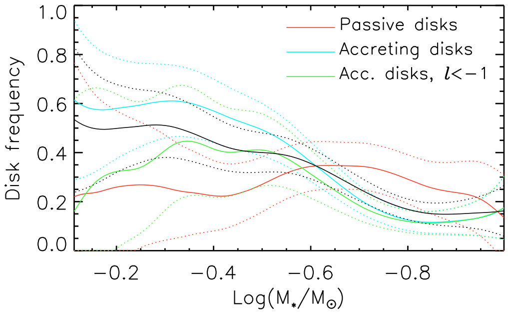

Figure 4.9: Frequency of circumstellar disks in our sample of stars as a function of stellar mass. The red line shows the frequency limited to the passive disk sample, while the cyan line corresponds to the subsample of accreting disks. The green line shows the case of accreting stars with l <-1. The black line shows the joint disk frequency. The dotted lines reflect poissonian uncertainties.

the stellar surface, the accretion luminosity is given by:

$$L_{acc} = G\frac{M_*\dot{M}}{R_*}\left(1-\frac{R_*}{R_{disk}}\right) \backsimeq G\frac{M_*\dot{M}}{R_*}, \tag{4.11}$$

i.e. it linearly increases with increasing stellar mass.

In summary, Fig. 4.10 tells us that if accretion were the only source of NIR excess, we would be able to detect it only for stars with $l \gtrsim$-1 and M$\gtrsim$0.2 M$_\odot$. This suggests that the steep rise in Fig. 4.9 for accreting stars with M$\gtrsim$0.2 M$_\odot$ is due to the additional contribution of systems with relevant ongoing accretion phenomena. From the observational point of view, we show in Fig. 4.9 that the frequency of active disks limited to the sample of stars with l <-1 partially reconciles with the frequency of passive disks. This further indicates that the observed high incidence of active disks is driven by the enhancement of NIR emission due to accretion.

4.3.3 Trend with stellar age

Stars in the ONC span only a limited range in age: many authors (e.g. Muench et al. (2008, and references therein), D10) find that the ONC is $\lesssim$2 Myr old. Thus, we expect relatively little disk evolution, since typical lifetimes for disks surrounding low mass stars appear to be $\lesssim$6 Myr (Skrutskie et al. 1990; Haisch et al. 2001).

In Fig. 4.11 we present the disk frequency as a function of the stellar age, derived using the theoretical model of D'Antona & Mazzitelli (1998). As we expected, we do not find any clear evidence of evolution in the ONC.

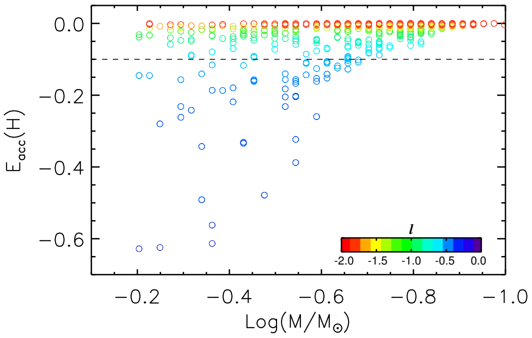

Figure 4.10: $E_{acc}(H)$ magnitude excess due to accretion only for the subsample of actively accreting stars. The excess of each stars is estimated accounting for the corresponding photospheric flux and the measured accretion luminosity. We find that the magnitude of the H-excess increases with accretion (coded in colors from red to purple with increasing l), and that our detection limit of -0.1 (shown in dashes) is exceeded for $l \gtrsim$-1 and log M/M$_\odot$ $\gtrsim$-0.7 (M$\gtrsim$0.2 M$_\odot$).

If anything, there appears to be an increase in the apparent disk frequency at young ages ($\lesssim 10^6$ yr), and a slow decrease towards older ages. The increasing trend at young ages is likely related to the star/disk contrast, which increases as the stars contract descending the Hayashi track (Hillenbrand et al. 1998). By consequence, our detection efficiency increases with age. On the other hand, although stars keep contracting, after $t \sim 10^6$ yr we find that the increasing trend is reverted, suggesting that some evolutionary effect may reduce the NIR emissivity of disks.

4.3.4 Trend with projected cluster radius

Based on the stellar volumetric density in the inner ONC measured by Hillenbrand & Hartmann (1998), the mean distance between stars is of the order of $\sim 10^3$ AU, i.e. a few times the size thought characteristic of circumstellar disks in the ONC (Vicente & Alves 2005). In this environment, effects such as the enhancement of accretion rates or the tidal truncation of disks may be important. The resultant shortening of circumstellar disk lifetimes might produce a preferential absence of disked stars in the innermost cluster. O'Dell et al. (2008) also suggest that circumstellar disk lifetimes in the inner ONC are significantly shorter than the estimated age of the cluster, due to photoevaporation induced by the UV radiation field. Robberto et al. (2004) support this scenario finding indication for disk dissipation in the inner ONC.

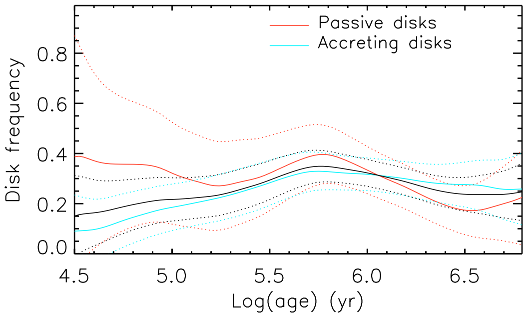

Figure 4.11: Frequency of circumstellar disks in our sample of stars as functions of stellar age. The red and the cyan lines show the frequencies limited to the passive and active disks subsamples respectively, while the black line shows the joint disk frequency. The dotted lines reflect poissonian uncertainties. In these plots we do not find any clear evidence of disk evolution in the limited age range spanned by the ONC. We just find some indication on the slow decrease of the apparent disk fraction with increasing age.

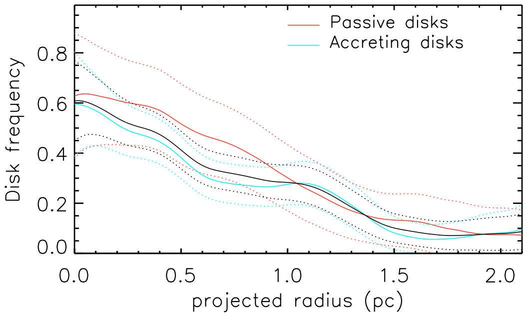

Figure 4.12: Same as in Fig. 4.11 for the trend of disk frequencies as functions of the projected cluster radius.

To investigate these effects, in Fig. 4.3.4 we plot the trend of passive/active disk frequencies with projected distance from the cluster center, namely Θ^1OriC (RA (2000.0)=$05^h35^m16.46^s$, DEC (2000.0)=$-05°23'23.18''$). We find that the apparent fraction of disked stars (whether passive or active) generally decreases with increasing distance, in contrast with the arguments above. In particular, the derived frequencies decrease from $\sim$80% in the inner cluster down to $\sim$10% at the largest projected distance.

Since there are no systematic effects in our ability in detecting disks as a function of cluster radius, we interpret the frequency trend to be a real indicator of variations in the disk population with the projected radius.

One possibility is that the stars in the neighborhood of Θ^1OriC have not had enough time to clear their inner disks, i.e. they are younger than the stars at larger distances. While recent studies support the hypothesis that the inner cluster may have formed in relatively recent times (t$\sim 10^5$ yr, e.g. Hillenbrand 1997; O'Dell et al. 2008; Reggiani et al. 2011), this scenario controverts the evidences of disk clearing in the Trapezium found by Robberto et al. (2004). Moreover, as we find in Sect. 4.3.3, there are little evidences of disk evolution in the age range spanned by the ONC.

The other possibility is that NIR emission is enhanced by environmental effects. As a matter of fact, Robberto et al. (2002) model the SED of circumstellar disks embedded in HII regions, finding that in the presence of the UV radiation field, circumstellar disks evaporate and form an ionization front surrounding the central disked star and shielding the system from the Lyman continuum radiation. The outcomes are called *proplyds* and they typically appear as drop-like shaped diffuse objects pointing towards the source of the radiation field, i.e. Θ^1OriC (O'Dell et al. 2008, and references therein). In particular, the photoevaporated envelope is an extra-source of NIR radiation whose emitted flux increases with wavelength. By consequence, assuming that disked stars are evenly distributed within the cluster, for both subsamples we expect larger frequencies with decreasing distance from Θ^1OriC. This is consistent with the fact that (1) the apparent frequency of disks smoothly increases towards the center of the cluster; and (2) the observed frequencies of both passive and active circumstellar disks show the increasing trend with decreasing projected distance.

4.3.5 Discussion

In the previous sections we have analyzed the apparent frequencies of disks in our sample of low-mass stars as functions of stellar mass, stellar age and projected distance from Θ^1OriC. Our results can be summarized as follows:

- the observed frequency of passive disks does not depend on the mass of the central star. For the accreting stars sample we find that the accretion activity enhances the excess infrared emission, leading to increasing observed frequencies with increasing stellar mass;
- the observed frequencies weakly depend on the age of the central star: for both subsamples of stars we find weak evidences of disk evolution in the ONC;
- for both subsamples we derive increasing frequencies with decreasing dis-

tance from the center of the cluster, as a consequence of the enhancement of NIR emission due to the UV radiation permeating the HII region in the ON.

We remark that the derived disk frequencies are lower limits for the actual frequencies of disks in the ONC. As a matter of fact, Hillenbrand et al. (1998) use the disk models of Calvet et al. (1991); Calvet & Gullbring (1998) to compute the star+disk SED for different inner radii, mass accretion rates and disk inclinations, deriving that the amount of infrared excess is a function strongly depending on these parameters. In particular, their results suggest that weak infrared excesses do not imply the absence of circumstellar matter, but they can also be indicative of large inclination angles γ with respect to the line of sight, or large inner radii, or a combination of them.

The theoretical SED models for star+disk systems computed by Robitaille et al. (2006) show that for $\gamma \gtrsim 80^\circ$ the optical thickness of the disk drastically increases, such to reduce the observed stellar flux by more than a factor of 10. Since most of the stars in the analyzed sample have $A_V \lesssim 2.3$, consistently to the extinction provided by diffuse matter within the Nebula (O'Dell & Yusef-Zadeh 2000; Scandariato et al. 2011), we argue that the corresponding disks are not seen edge-on. It is also remarkable that most of the stars, despite their intrinsic red colors, have measured WFI UB-magnitudes, supporting the assumption of limited extinction, i.e. $\gamma < 80^\circ$.

By consequence, assuming that γ is uniformly distributed between 0° and 90°, we argue that we miss at least $\sim (90-80)/90 \sim 10\%$ of disks, i.e. the disk frequencies derived in the previous sections underestimates the true frequencies by at least ∼10%.

Moreover, we still miss disks with large inner radii which, by virtue of their low temperatures, poorly radiate in the NIR domain. Thus, given the multiplicity of influences on the magnitude excess from disk properties, great care is needed in diagnosing the presence of disks using NIR excesses, and we conclude that from the $E(H)$ index we obtain a lower limit for the frequency of disks in the ONC.

4.4 Summary

In this chapter we have analyzed the NIR excess of ∼700 ONC members with previous spectroscopic characterization, and distinguishing the subsamples with and without accretion evidences.

Comparing the extinction-corrected magnitudes to the expected magnitudes given the spectral type, we have estimated the flux excess in the three JHK_S bands and we have found that they strongly correlate with each other. We have also found that the observed correlations are consistent with the JHK_S fluxes radiated by a circumstellar disk, plus the contribution from the accretion luminosity for the subsample of accreting objects.

We have also analyzed the incidence of circumstellar disks detection as a function of stellar mass, stellar age and projected distance from the cluster center. We have found that the observed fraction of disked stars ($\gtrsim 20\%$ of the total sample) does not depend on stellar mass or stellar age. We also found that disks are more easily detected in the presence of ongoing accretion: this is due to the twofold effect of ongoing mass accretion: (1) it heats up the disk enhancing its NIR luminosity; and (2) the continuum SED of the accretion column contributes to the total NIR excess.

Finally, we have found that the observed incidence of disks increases with decreasing distance from the cluster center. This result is consistent with the fact that the UV radiation field (powered by Θ^1OriC) interacts with circumstellar disks forming inflated ionization fronts, known as proplyds, via photoevaporation of dust from the disk surface. The NIR detectability of these system is thus enhanced by the fact that the hot photoevaporated matter represents an extra-source of NIR radiation.

Chapter 5

The IMF of the ONC

The main goal of this study is to derive the photometrically-determined IMF of the ONC. As discussed in D'Antona & Mazzitelli (1998); Lada & Lada (2003), the IMF of a population of stars can be derived from the intrinsic LF of the same population through the equation

$$\frac{dN}{dM_L} = \frac{dN}{dm} \cdot \frac{dm}{dM_L}, \tag{5.1}$$

where M_L is the logarithmic mass; the left hand of the equation is the IMF; $\frac{dN}{dm}$ is the LF in the photometric band m and $\frac{dm}{dM}$ is the derivative of the MLR $m(M_L)$, which gives the conversion from magnitudes to masses.

In order to derive the IMF of the ONC we thus have to recover the intrinsic LF from the observed LF. In the following sections we describe our statistical method to achieve this goal. In Sect. 5.1 we statistically estimate the incidence of contamination in our observed sample, while in Sect. 5.2 we introduce our recipe to correct the observed (JHK_S) photometry for any extra-photospheric effects (interstellar extinction and circumstellar excess), obtaining the intrinsic photometry. In Sect. 5.2.2 we describe our new algorithm which converts the LF into the IMF, and we run a simple simulation to test its robustness. Finally, in Sect. 5.3 we derive the photometrically-determined IMF of the ONC.

5.1 The corrected Color-Magnitude Diagrams of the ONC

In this section we aim at statistically deriving the intrinsic NIR CMDs of the ONC, as it will be a key tool in order to account statistically for contamination in deriving the IMF of the cluster (Sect. 5.3).

Scandariato et al. (2011) show that a rough discrimination of cluster against contaminant population is possible as the two groups of stars occupy different locations in the NIR CMDs, the former being generally brighter than the latter. Testing all the possible combinations of infrared magnitudes and colors, we find that the (J,J-H) diagram minimizes contamination of the cluster CMDs from contaminants (both galactic and extragalactic). This is due to the fact that the extinction law is a decreasing function of wavelength in the NIR domain: by consequence, the minimization of contamination, achieved maximizing the extinction suffered by background contaminants, occurs at the bluest wavelength, i.e. J and H.

We extract XXX point-like sources with measured JHK_S photometry from our infrared catalog.

Figure 5.1 shows the projected density of the stars in our photometric sample. It is apparent that the inner cluster is mostly concentrated within a few arcminutes ($\sim 3'$) from Θ^1OriC (indicated as the big star symbol). The core of the cluster is then surrounded by an intermediate population distributed following a north-south pattern. Finally, farther from the Trapezium, we find the outer sparse population of stars with uniform and relatively low projected density, which will be demonstrated to be mainly made up by background stars (Sect. 5.1.3). Together with these three subsamples, labeled as “Region 1”, “Region 2” and “Region 3”, we also define “Region 4”as the group of stars within $2.5'$from NU Orionis. This extra subsample is meant to avoid any contamination in our analysis of the ONC properties due to the M43 cluster. In the following analysis we will discuss the properties of these four subsamples of stars, in order to investigate any eventual variation of the cluster properties with the distance from the Trapezium cluster.

In Fig. 5.3 we plot the observed (J,J-H) CMDs of the four regions.

5.1.1 Completeness correction

In order to correct the CMDs for completeness, we use the fake-star experiment discussed in Sect. 1.3 in order to estimate the completeness sensitivity in the 4 regions and in the three bands. Our results are shown in Fig. 5.2.

We compute the completeness diagram corresponding to the (J,J-H), i.e. the probability detection for a star with given magnitude J and color J-H, by multiplying the completeness sensitivity in the J and H bands. We thus derive the

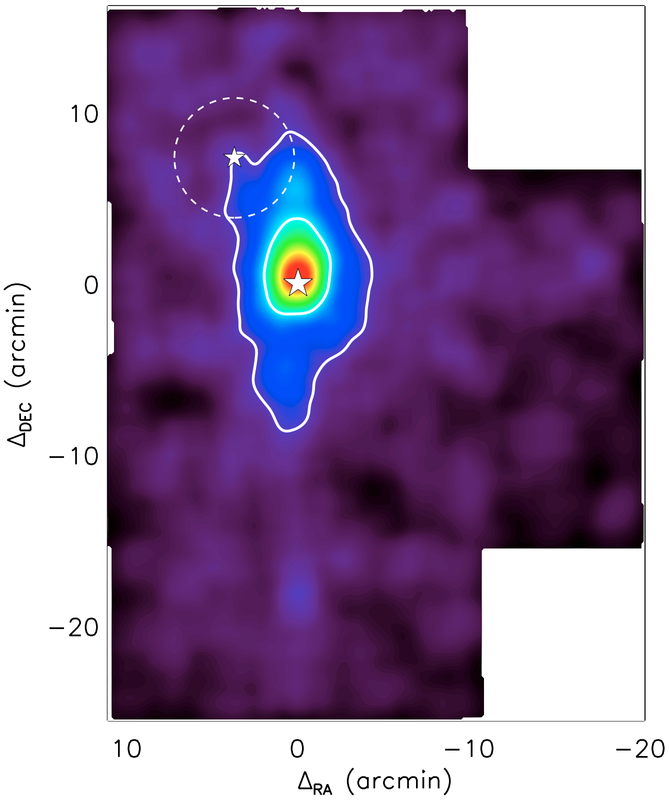

Figure 5.1: Projected density of the stars in our photometric sample. The solid white contours outline the three subsamples into which we divide the whole sample. We also plot the boundary of the M43 region with the dashed white circle (r=2.5′), centered on NU Orionis (the small star symbol).

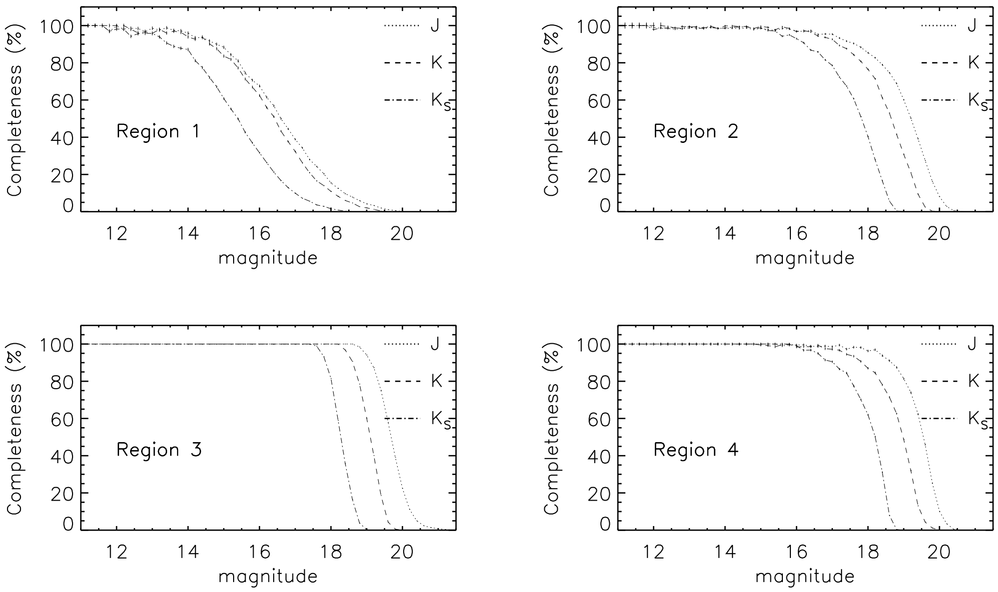

Figure 5.2: Completeness sensitivity in the four regions discussed in the text.

completeness-corrected (J,J-H) CMDs dividing the observed CMDs by the (J,J-H) completeness diagram. The CMDs corrected for completeness are plotted in the second column of Fig. 5.3. In these plots we show the 90% completeness sensitivity (dotted-dashed line), except for Region 1 where we set the 80% threshold. These cuts will be used is Sect. 5.3 to derive the completeness-limited IMF of the ONC.

5.1.2 Contaminant CMDs

The amount of contamination in the completeness-corrected CMDs is statistically computed by means of the extinction map derived in Chapter 2.

In order to estimate the incidence of background galaxies, seen as point-like sources in our images, we follow the procedure described in Sect. 2.2.3 and we derive the extragalactic CMD extincted by the OMC-1. Similarly, we estimate the galactic contamination in the CMDs using the galactic population model provided by Robin et al. (2003).

The sum of the galactic and extragalactic contaminant CMDs is shown in the third column of Fig. 5.3. In these diagrams, as discussed in Sect. 2.2.3, the main contribution ($\gtrsim$99%) is due to the background galactic population.

5.1.3 The intrinsic CMDs

Having the completeness-corrected CMDs and the contaminant CMDs at hand, the ONC intrinsic CMDs are computed by a simple subtraction. The derived CMDs are shown in the last column in Fig. 5.3.

Our results show that Region 1 is negligibly contaminated, while the background galactic population is detected in the regions farther out of the Trapezium direction. The contamination correction confirms the assumptions in 2.2, i.e. the bimodal distribution in the CMDs is due to the presence of two populations of stars: the brightest one, being unaffected by the correction, is the ONC population, while the faintest one, which cancels out after the correction, is due to background contamination.

5.2 From photometry to the mass distribution

In this section we discuss how we correct the observed photometry for interstellar extinction and circumstellar excess to derive the intrinsic photometry. We also discuss how we convert the intrinsic photometry into masses, and we present our algorithm aimed to derive the photometrically-determined IMF.

5.2.1 Derivation of the intrinsic photometry

Given an extinction law $a_\lambda = \frac{A_\lambda}{A_V}$, for any given star the effect of differential extinction can be expressed as:

$$\begin{bmatrix} J_i \\ H_i \\ K_{S,i} \end{bmatrix} = \begin{bmatrix} J_o \\ H_o \\ K_{S,o} \end{bmatrix} - \begin{bmatrix} a_j \\ a_h \\ a_k \end{bmatrix} \cdot A_V \tag{5.2}$$

where the left side of Eq. 5.2 is the unknown intrinsic NIR photometry, and the right side is the difference between the observed photometry and the amount of extinction respectively. The set of parameters (a_j, a_h, a_k) is given by the assumed extinction law, while A_V is the unknown extinction. Lucas et al. (2005), assuming an evolutive model and an extinction law, basically adopt this strategy to deredden the observed (J,H) photometry towards the PMS isochrone.

The intrinsic NIR photometry may also be affected by the presence of circumstellar disks, whose continuum SED can be detected as flux excess with respect to the intrinsic stellar flux (see Chapter 4). In order to parametrize

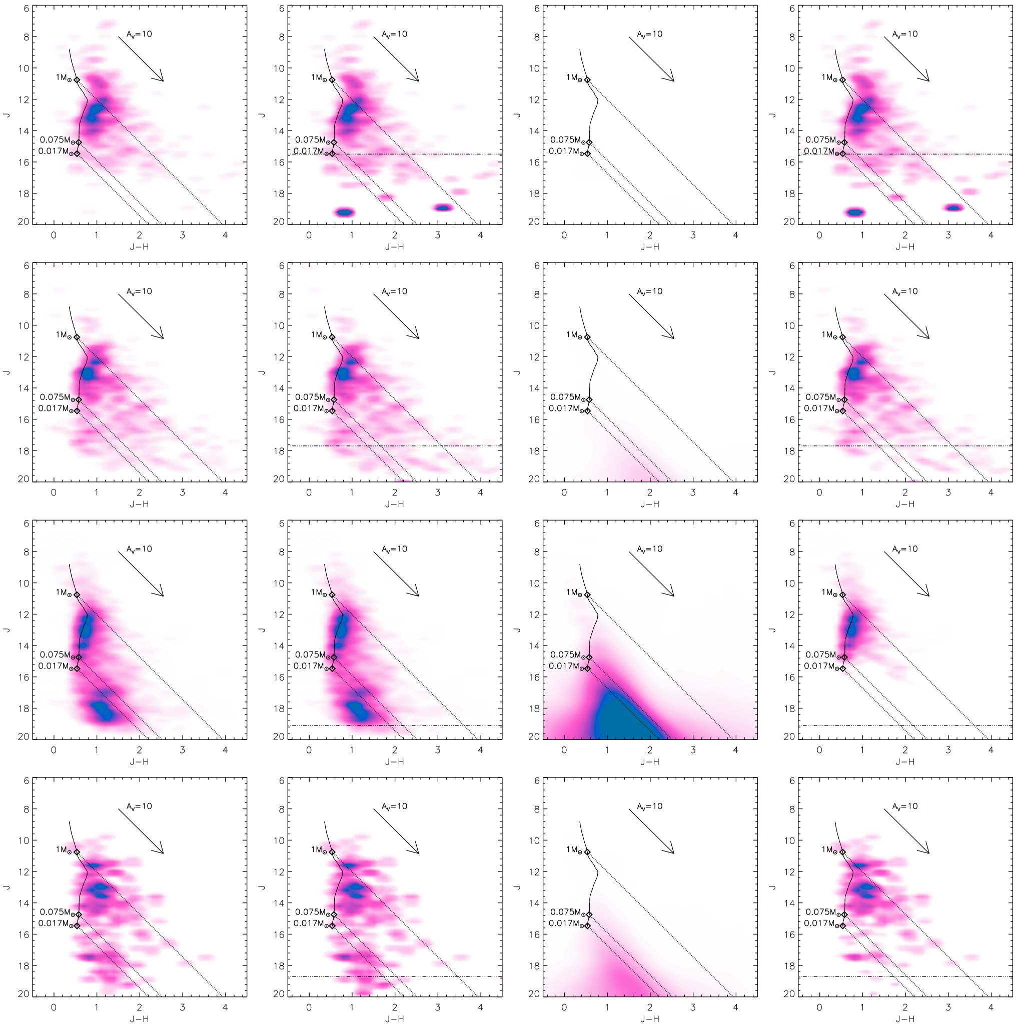

Figure 5.3: *First column* – Density distribution of stars in the observed CMDs for the four regions in the surveyed area (Region 1 to 4 from top to bottom respectively). The solid white line is the isochrone computed in Chapter 3. The dotted lines represent the extinction direction (also indicated as an array corresponding to A$_V$=10) corresponding to 1M$_\odot$, 0.075M$_\odot$ and 0.017M$_\odot$. *Second column* – Completeness-corrected CMDs. The horizontal dotted-dashed lines represent the 90% completeness limit (the 80% for Region 1) above which we perform our analysis. *Third column* – Contaminant CMDs accounting for both galactic and extragalactic contribution. *Last column* – Completeness-contamination-corrected CMDs, computed as the difference between the second and the third column. In each row, for the sake of comparison, the color scale is kept from left to right.

the disk excess in the three bands, in Sect. 4.2.1 we find strong correlations between the magnitude excesses $E(J)$, $E(H)$ and $E(K_S)$, defined as the difference between the extinction-corrected and the expected photometry. These correlations can be expressed as:

$$E(J) = e_J \cdot E(H) \tag{5.3}$$

$$E(K_S) = e_K \cdot E(H) \tag{5.4}$$

Aiming at the intrinsic magnitudes of stars, Eqs. 5.3-5.4 allow to modify Eq. 5.2 in order to take into account any eventual infrared excess due to disks:

$$\begin{bmatrix} J_i \\ H_i \\ K_{S,i} \end{bmatrix} = \begin{bmatrix} J_o \\ H_o \\ K_{S,o} \end{bmatrix} - \begin{bmatrix} a_j \\ a_h \\ a_k \end{bmatrix} \cdot A_V + \begin{bmatrix} e_j \\ e_h \\ e_k \end{bmatrix} \cdot E(H) \tag{5.5}$$

where $E(H)$ is the unknown magnitude excess in the H band.

Given the observed photometry, the unknown parameters A_V and $E(H)$ are crucial to univocally correct the observed photometry for both extinction and excess, allowing to derive the intrinsic photospheric flux of the targets.

5.2.2 The geometric solution

So far, Eq. 5.5 is basically a system of three equations with five unknowns: A_V, $E(H)$ and the three intrinsic magnitudes J_i, H_i and $K_{S,i}$. We now take advantage of the empirical isochrone reported in Table 3.2 in order to constrain the three intrinsic magnitudes as functions of the parameter T_{eff}. This allows us to reduce the number of unknowns from five to three: A_V, $E(H)$ and T_{eff}.

Since we aim at the mass distribution of the ONC, we need to convert the temperature T_{eff} into the stellar mass M_L. This relation is not provided by our empirical isochrone. We thus use the T_{eff}-vs-M_L relation provided by the theoretical 1 Myr old model of D'Antona & Mazzitelli (1997), assuming that it well represents the evolutionary state of the stars in the ONC. As a consequence, combining this theoretical model to our empirical isochrone, we derive the semi-empirical MLR appropriate for the ONC.

Given these assumptions, we re-write Eq. 5.5 as:

$$\begin{bmatrix} J_i \\ H_i \\ K_{S,i} \end{bmatrix} (M_L) = \begin{bmatrix} J_o \\ H_o \\ K_{S,o} \end{bmatrix} - \begin{bmatrix} a_j \\ a_h \\ a_k \end{bmatrix} \cdot A_V + \begin{bmatrix} e_j \\ e_h \\ e_k \end{bmatrix} \cdot E(H) \tag{5.6}$$

stressing that the intrinsic photometry is now function of just one unknown: the stellar mass M_L.

Since the MLR is not analytical, we adopt a geometric approach to solve the system in Eq. 5.6. We consider a 3D space with cartesian axes corresponding to the J, H and K_S magnitudes. In this geometry, the right side in Eq. 5.6 identifies a plane passing through the point corresponding to the observed photometry and generated by the vectors (a_J, a_h, a_k) and (e_J, e_H, e_K). This 2D space is spanned by all the (A_V,$E(H)$) couples, and by consequence it also contains the intrinsic photometry of the given star.

Given our empirical 3D "(JHK_S) diagram", provided that it is not degenerate with the $(A_V, E(H))$ plane (i.e. the solution of Eq. 5.6 is unique), the expected intrinsic photometry for the given star is the intersection between the isochrone and the plane (Fig. 5.4). Once the intersection between the plane and the (JHK_S) diagram is found, there is only one couple of vectors (indicated as a and e) which shifts the observed photometry to the derived intrinsic photometry. These two vectors represent the extinction A_V and the excess $E(H)$ in Eq. 5.6. Moreover, once the intersection is found, this procedure immediately provides the mass of the star through our semi-empirical MLR.

From a computational point of view, it is now more convenient to define a new reference system, in which the horizontal plane is generated by the $(A_V, E(H))$ vectors, and the axis perpendicular to this plane, defined as the s axis, measures the euclidean distance from the horizontal plane. The s coordinate is thus invariant for translations along horizontal planes. As a consequence, the observed photometry of a given star has the same s coordinate of the corresponding intrinsic photometry. In other words, the correction of the observed photometry for extinction and excess is no longer a necessary step in order to derive the intrinsic photometry of the star. In any case, we remark that the extinction law and the correlations between the excess in the JHK_S bands still enter the algorithm through the definition of the new horizontal plane.

From a physical point of view, the s parameter contains the photometric information. It can be interpreted as a new "magnitude", i.e. the "s magnitude", to be plugged in Eq. 5.1 in place of any standard photometric band m. With this in mind, we edit Eq. 5.1 such that the LF is the distribution of stars in terms of s, while the MLR is the Mass-vs-s relation:

$$\frac{dN}{dM_L} = \frac{dN}{ds} \cdot \frac{ds}{dM_L}. \tag{5.7}$$

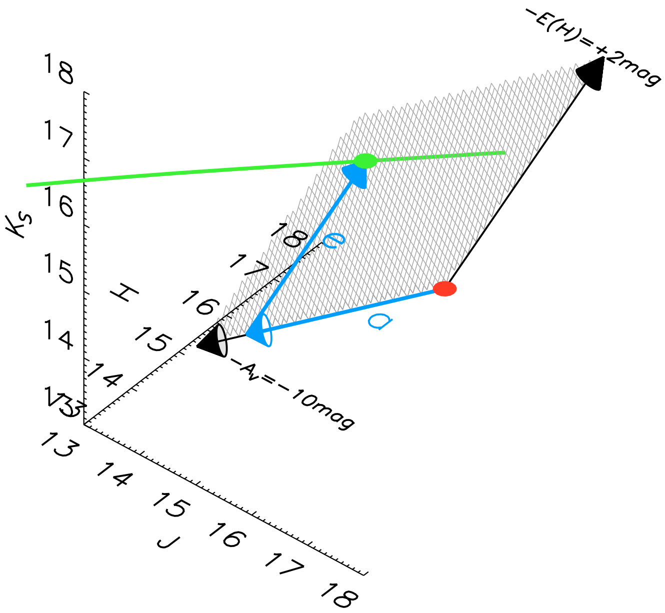

Figure 5.4: Correction of the observed photometry in the 3D (JHK_S) diagram. The red spot corresponds to the observed photometry: it locates the (A_V,$E(H)$) plane (the shaded gray plane), which intersects the isochrone (the green solid line). The green spot is the intersection between the plane and the isochrone, and it is given by a unique combination of the vectors a and e, parallel to A_V and $E(H)$ respectively. This method thus leads to the intrinsic photometry of the star, together with the amount of extinction and infrared excess affecting entering the observed photometry.

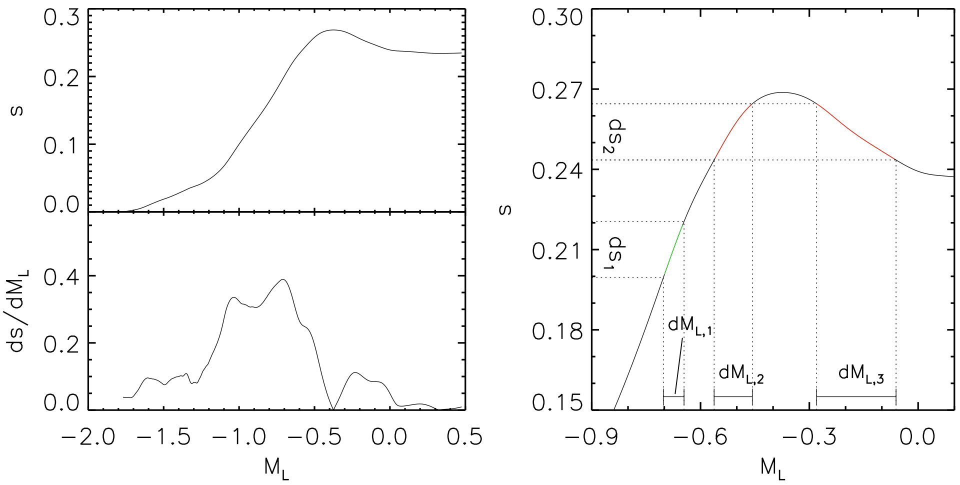

Figure 5.5: *Left panel* - MLR for the isochrone computed in 3.4 and its derivative, from top to bottom respectively. *Right panel* - Zoom in of the MLR relation shown in the left panel, showing the degeneracy problem. While for the ds_1 interval there is a unique $dM_{L,1}$ interval, there are two mass intervals corresponding to ds_2: in this case, a star in ds_2 belongs to either mass interval, with probabilities given by Eq. 5.10.

It is evident in Eq. 5.7 that the $s(M_L)$ function enters the equation only in terms of derivative. Therefore, this function can be defined up to an additive constant. For convenience, we set this constant such that the function s is zero for the lowest mass in our empirical isochrone: $s(M = 0.017M_\odot) = 0$. We also orient the s axis such to be positive for larger masses. In Fig. 5.5 we show the new MLR and the corresponding derivative.

5.2.3 The degeneracy problem

In Fig. 5.5 we show our s-based MLR, which allows us to take into account *simultaneously* the full set of JHK_S magnitudes of the star in deriving its mass. This relation provides a biunivocal link between s and M_L for $s \lesssim 0.24$, i.e. the mass of the star is straightforwardly derived by inverting the function $s(M_L)$.

For larger s magnitudes the MLR provides multiple solutions, i.e. the MLR is degenerate with respect to the $(A_V, E(H))$ plane. The presence of degenerate solutions is a problem, as long as we cannot break the degeneracy without any *a priori* knowledge on the mass distribution of the cluster.

Figure 5.5 shows a schematic picture of the degeneracy problem. If we consider an infinitesimal interval at $s = s_1$, then only one segment along the MLR relation is intercepted, i.e. there is just one $dM_{L,1}$ interval corresponding to the given ds_1 interval. Following D'Antona & Mazzitelli (1998), this means that the density of stars per unit logarithmic mass can be computed as:

$$\left(\frac{dn}{dM_L}\right)_{M_{L,1}} = \left(\frac{dn}{ds}\right)_{s_1} \cdot \left(\frac{ds}{dM_L}\right)_{M_{L,1}} \tag{5.8}$$

Let's now consider the case of the interval ds_2, which intercepts two mass intervals; this means that, given a star in ds_2, its mass is contained in either $dM_{L,2}$ or $dM_{L,3}$ (in the general case, more mass intervals may be intercepted). If we know the mass distribution of stars, we can compute the number of stars in the i-th mass interval $dM_{L,i}$ as:

$$dN(dM_{L,i}) = \left(\frac{dN}{dM_L}\right)_{M_{L,i}} \cdot dM_{L,i} \tag{5.9}$$

The probability $p(M_{L,j})$ that a star in the degenerate interval ds belongs to the $dM_{L,j}$ interval is thus given by:

$$p(M_{L,j}) = \frac{dN(dM_{L,j})}{\sum_i dN(dM_{L,i})} \tag{5.10}$$

where the sum over i is computed over all the intervals dM_L intercepted by ds.

The $p(M_{L,j})$ probabilities allow to break the degeneracy introduced by the M-s relation: introducing the probability $p(M_L)$ that a star in ds belongs to dM_L, Eq. 5.8 is modified as:

$$\left(\frac{dn}{dM_L}\right)_{M_L} = p(M_L) \cdot \left(\frac{dn}{ds}\right)_{s} \cdot \left(\frac{ds}{dM_L}\right)_{M_L} \tag{5.11}$$

In other words, we force a fraction $p(M_L)$ of the sample of stars in ds to be assigned to the dM_L mass interval. Obviously, if there is no degeneracy, Eq. 5.10 gives $p(M_L)$=1: Eq. 5.11 is thus a generalization of Eq. 5.8.

The probabilities $p(M_L)$ are not known a priory, unless there is no degeneracy, as they are given by the unknown mass distribution of the cluster. Nonetheless, in the following section we outline an iterative method which overcomes this indeterminacy.

5.2.4 The iterative algorithm

We now simulate an artificial sample of stars whose masses are distributed following the IMF of the ONC proposed by Muench et al. (2002) (Fig. 5.6). We

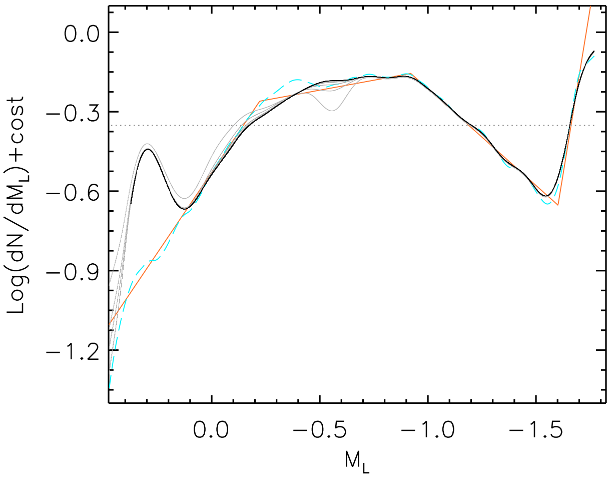

Figure 5.6: Results from our iterative algorithm. The solid orange line is the IMF of the ONC as derived by Muench et al. (2002), while the dashed blue line is the mass distribution of the artificial sample, simulated following the ONC IMF. We find that the recovered distribution is consistent with the assumed IMF. The dotted line is our flat initial guess, while the solid lines are the outcomes of the iterative algorithm, coded from gray to black towards convergence.

also assign to each star the JHK_S magnitudes provided by our semi-empirical MLR, and we compute the corresponding s-LF.

As a sanity check, we perform a naive computation aimed at testing the robustness of the theoretical apparatus described in the previous sections. Following the recipe described in Sect. 5.2.3, we compute the probabilities $p(M_L)$ using the simulated IMF, and we plug them in Eq. 5.11 in order to recover the mass distribution, shown in Fig. 5.6. Obviously, there is a non-sense in this computation: we assume to know the mass distribution in order to recover the same mass distribution. Nonetheless, the scope of this computation is to prove the correctness of Eq. 5.11, largely confirmed by our results: the assumed mass distribution is recovered almost exactly, besides small numerical approximations propagating through the algorithm.

As we anticipated above, the mass distribution is usually unknown, together with the $p(M_L)$ probabilities. To derive the unknown mass distribution, we thus adopt the following iterative approach.

We adopt a first guess of the mass distribution and we plug it in Eq. 5.10, in order to compute the probabilities needed in Eq. 5.11. The returned mass distribution is then smoothed out with a left-boxcar kernel for two main reasons. First of all, we want to reduce the noise introduced by numerical approximations and instabilities. In particular, the recovered distribution presents either positive or negative spikes in correspondence of the zeros of the derivative of the MLR.

Moreover, as shown in Fig. 5.5, degeneracy occurs for $M_L \lesssim -0.7$ ($M \lesssim 0.2 M_\odot$), while for lower masses there is a 1-to-1 correspondence in the MLR. This leads to the fact that the mass distribution at $M_L \lesssim -0.7$ is recovered right after the first iteration. For larger masses, there is no unique analytical solution for the $p(M_L)$ probabilities. Nonetheless, from previous studies of the ONC we do not expect any discontinuity in the IMF. The continuity requirement is therefore an extra-constrain which enables us to break the indeterminacy on $p(M_L)$. The left-boxcar kernel is thus aimed at forcing the recovered mass distribution to have a continuous shape, in such a way that the mass frequency at $M_L \gtrsim -0.7$ is continuously driven by the frequency at lower masses (where there is no degeneracy), and so on for masses larger than $M_L \gtrsim -0.7$.

The new guess of the mass distribution function is plugged back in Eq. 5.10, and the loop is repeated a large number of times until convergence is reached.

In Fig. 5.6 we show the results of this algorithm on our artificial sample of star. For simplicity, we start the loop with a flat distribution as our first guess. In any case, using different first guesses we find basically the same results. As we anticipated above, it is apparent that the simulated distribution at $M_L \lesssim -0.7$ is recovered right after the first iteration. For larger masses, the algorithm converges after ∼30 iterations. Notwithstanding, the algorithm is not able to recover the simulated frequencies for $M_L \gtrsim 0$: this is due to the fact that in this mass range the MLR is almost flat, and its derivative is small over a relatively extended mass range, such to introduce severe numerical instabilities which prevent the algorithm to converge.

5.3 The photometrically-determined IMF of the Orion Nebula Cluster

We no apply the iterative algorithm discussed in Sect. 5.2 to the specific case of the ONC.

We use the JHK_S of the sample of objects extracted in Sect. 5.1 limited to the 90% completeness level. Figure 5.3 shows that this threshold generally preserves the objects with masses well below the lower limit mass of our isochrone ($M = 0.017 M_\odot$). Only in Region 1 the completeness threshold potentially cuts a consistent fraction of BDs: for this reason we arbitrarily set a lower 80% completeness limit, including a larger fraction of BDs.

For each star in the sample we apply the geometric method discussed in Sect. 5.2.2, i.e. we derive the "*s*" magnitudes of the stars, taking our empirical isochrone as the reference locus for the ONC. Moreover, for each star we compute a statistical weight which takes into account the effects of completeness and contamination. This weight is computed as the product of two factors:

- the first factor is the inverse of the completeness diagram at the J magnitude and J-H color of the star, as discussed in Sect. 5.1.1: it compensates for detection losses due to our completeness sensitivity;
- the second factor is our statistical estimate of the membership of the star, i.e. the probability that the star belongs to the ONC. This probability is derived as the complement of the probability that the star belongs to the contaminant sample, which is computed as the point-wise ratio between the expected contaminant CMD and the completeness-corrected CMD (second and third column in Fig. 5.3 respectively).

We then derive the s-LF in each of the four regions, weighting each star with the statistical weights discussed above, and we derive the IMFs of the four regions using the iterative algorithm described in Sect. 5.2.4.

In order to take into account the photometric uncertainties, for each star we generate a set of 10^5 J, H and K_S magnitudes distributed following a gaussian function with mean and width given by the corresponding photometric measurement and uncertainty. For each star, we also compute a new completeness correction and membership corresponding to each of the 10^5 statistical JHK_S sets. We thus derive 10^5 s-LFs and we convert each of them into the corresponding mass distribution. The set of 10^5 IMFs is then averaged in order to derive the best estimate of the mass distribution and the corresponding 68% confidence band. Our results are shown in Fig. 5.7.

We find that the IMF of the four regions show the same general features: they increase with Salpeter-like slope with decreasing masses, they reach a broad peak at $M_L^{peak} \sim -0.77 \sim 0.17 M_\odot$, and then they continuously fall crossing the hydrogen-burning limit ($M = 0.075 M_\odot$).

Hennebelle & Chabrier (2008) provides a predictive theoretical foundation to understand the origin of the stellar IMF based on the concept of the gravother-

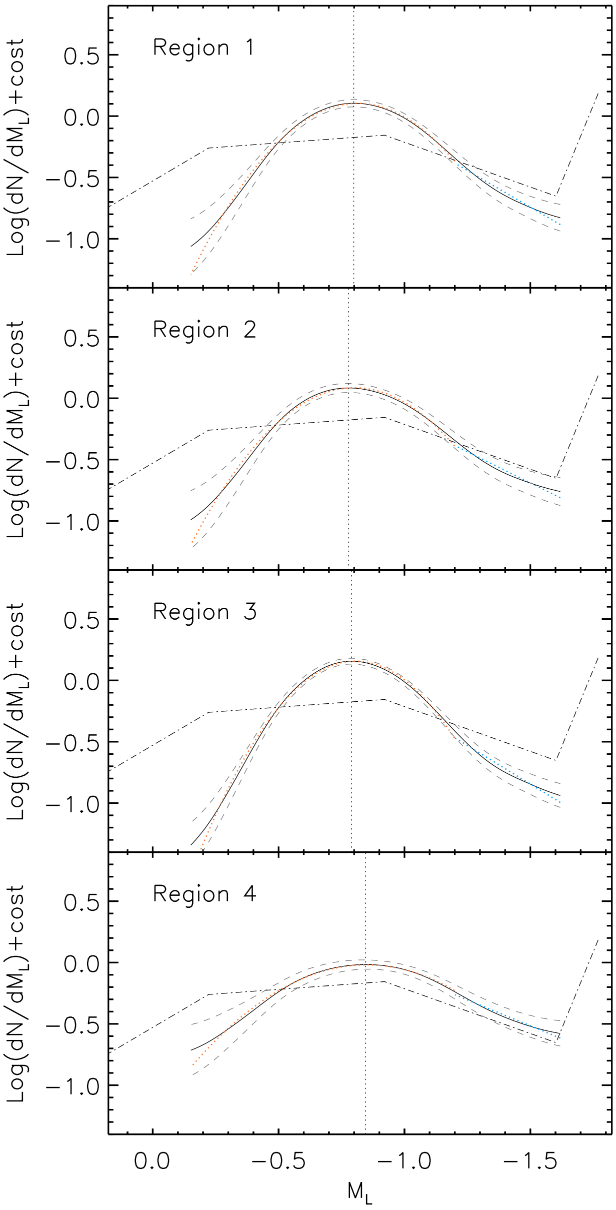

Figure 5.7: IMF of the 4 analyzed regions. In each panel, the solid and the dashed lines represent our derived IMF and the corresponding confidence band, while the vertical line marks the peak position. The dotted line show the log-normal ($M_L > -1.2$) and the power-law ($M_L < -1.2$) fits (red and blue dotted line respectively). For comparison, we also show the Trapezium IMF derived by Muench et al. (2002) (dashed-dotted line).

Table 5.1: Derived parameters for the IMF of the 4 regions.

Region	$M_L^{peak}\left(\frac{M^{peak}}{M_\odot}\right)$	$M_L^c\left(\frac{M^c}{M_\odot}\right)$	σ	Γ	$R_{ss}{}^a$	$R_{ss}{}^b$
1	-0.80 (0.16)	-0.81 (0.16)	0.39	1.16	0.19	0.16
2	-0.80 (0.16)	-0.82 (0.15)	0.40	0.86	0.23	0.19
3	-0.79 (0.16)	-0.80 (0.16)	0.35	1.21	0.15	0.13
4	-0.80 (0.16)	-0.82 (0.15)	0.51	0.81	0.25	0.20

Notes. (a) Upper limit, form our derived IMF. (b) Derived extrapolating the stellar regime.

mal and gravoturbulent collapse of a molecular cloud, and leading to the derivation of the mass spectrum of self-gravitating objects in a quiescent or a turbulent environment. The theory predicts that the shape of the IMF results from two competing contributions: an exponential cutoff (log-normal form) centered around the characteristic mass (M_L^c), smoothly extending towards larger scales following a power law.

We thus adopt this theoretical model, and we fit the IMFs in the $-1.2 < M_L < 0$ mass range using the log-normal function

$$\frac{dN}{dM_L} \propto exp\left(-\frac{(M_L - M_L^c)^2}{2\sigma^2}\right). \tag{5.12}$$

The fit parameters, listed in Table 5.1, confirm the consistency of the IMFs at different distances from the Trapezium cluster.

In the BDs domain ($M_L \lesssim -1.2$) the log-normal fits deviate from the IMFs, systematically underestimating the observed frequencies. On one hand, it may be due to an inaccurate contamination correction. As a matter of fact, in the completeness-contamination corrected CMDs for Regions 1-2 (fourth column in Fig. 5.3 we find some residuals after the contamination subtraction for $M < 0.075 M_\odot$, which are not present in the corresponding CMD of Region 3. In any case, these residuals are consistent with statistical poissonian noise, and this is reflected by the fact that the confidence band of the IMFs broadens with decreasing stellar mass. As a consequence, although the log-normal fits systematically provide lower frequencies, they still remain consistent within the uncertainties of the derived IMFs.

On the other hand, the fact that the derived IMFs present such a systematic discontinuity with respect to the theoretical predictions of Hennebelle &

Chabrier (2008) may be indicative of a secondary formation mechanism in the BDs domain. We quantify the decrease in the BDs domain fitting the IMFs with the power-law $\frac{dN}{dM_L} \propto M^{\Gamma}$, where Γ thus represents the slope of the IMFs in the log-log plot. Our best-fitting slopes, listed in Table 5.1, do not present any correlation or trend of the Γ parameter within the ONC.

In order to further investigate the substellar IMFs, we quantify the fraction of BDs with respect to the number of stars computing the ratio of the numbers of substellar and stellar objects (Briceño et al. 2002) as:

$$R_{ss} = \frac{N(M < 0.075M_{\odot})}{N(M > 0.075M_{\odot})}, \tag{5.13}$$

where the numerator and the denominator are computed integrating the observed IMFs in the two mass ranges. Estimates of this kind are useful diagnostic tools because they have the advantage that the bins adopted are significantly wider than the errors in the assigned masses. In Table 5.1 we list our derived ratios. Since these values may be biased by the cut at $M = 1M_{\odot}$, we extrapolate the IMFs at higher masses using smoothly extending the log-normal fit with a straight line, as predicted by Hennebelle & Chabrier (2008), and we update the R_{ss} values, finding ratios lower by ∼15-20%. We find that the R_{ss} ratio decreases towards the outskirts of the ON from ∼0.2 down to ∼0.1, while Region 4, which corresponds to the M43 nebula, has a R_{ss} ratio consistent to Region 1, i.e. the core of the M42 nebula. The consistency between the R_{ss} ratios of Region 1 and 4 supports the gravitational fragmentation mechanism of star formation, as proposed by Bonnell et al. (2008); Bonnell et al. (2011). In this scenario, structures in the star forming cloud form filaments flowing into the cluster center (the Trapezium in the ON, NU Orionis in M43). The gas density in the filaments increases with the downfall, and the Jeans mass decreases, allowing the formation of very low-mass fragments. The deviation of the low-mass IMFs from the mass distribution predicted by Hennebelle & Chabrier (2008) may thus be indicative of this alternative star forming mechanism in the sub-stellar domain, competing the gravothermal and gravoturbulent collapse scenario.

5.3.1 Comparison with previous studies

A number of other authors have recently derived the IMF of the ONC, using somewhat different cluster parameters and employing a variety of different

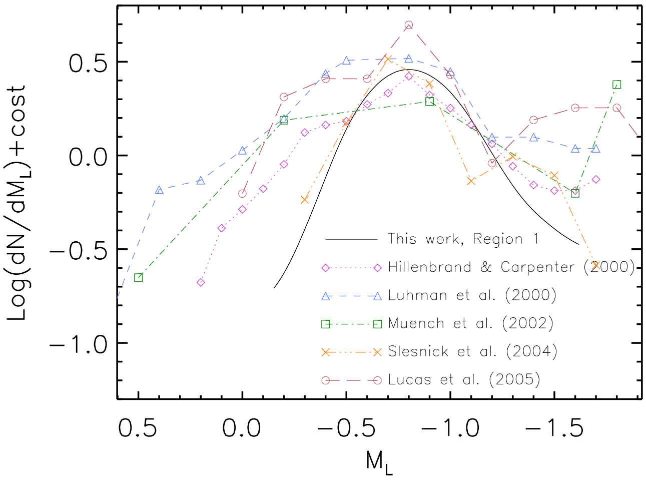

Figure 5.8: Comparison of the published IMFs for the inner ONC discussed in the text, together with our derived IMF for Region 1.

methodologies. Systematic uncertainties might arise from the varying of cluster parameters such as distance, different assumptions about the cluster population such as field star contamination, or simple observational effects such as survey area or the wavelength regime analyzed. Further, it is not understood how closely different methods can arrive at the same IMF.

In Fig.5.8 we compare the IMFs derived several authors. A determination based on NIR photometric data was made by Hillenbrand & Carpenter (2000) using H and K magnitudes and colors combined with star count data to constrain the IMF down to ∼0.03 $M_\odot$. They find a mass function for the inner ∼5′×5′ region of the ONC, which rises to a peak around 0.15 $M_\odot$ and then declines across the hydrogen-burning limit, with slope Γ=0.57.

Luhman et al. (2000) combined NIR NICMOS photometry of the inner 140″×140″ of the ONC with limited ground-based spectroscopy of the brightest objects (K ¡ 12) to determine a mass function that follows a power-law slope similar to but slightly steeper than the Salpeter value, until it turns over at ∼0.2 $M_\odot$ and declines steadily through the brown dwarf regime.

Muench et al. (2002) transform the inner ONC's K-band LF into an IMF and find a mass function that rises with decreasing mass to form a broad peak between 0.3 $M_\odot$ and the hydrogen-burning limit before turning over and falling off into the substellar regime. This decline is broken between 0.02 and 0.03 $M_\odot$, at which the IMF may contain a secondary peak near the deuterium-burning limit of 0.013 $M_\odot$.

A fully spectroscopically-determined IMF of the inner ONC is provided by Slesnick et al. (2004): they find that the mass distribution peaks at $\sim$0.2 $M_\odot$, then it falls across the hydrogen-burning limit and it levels off below $\sim$0.08 $M_\odot$ down to their completeness limit of $\sim$0.02 $M_\odot$, with poor evidence for a secondary peak in the BDs regime. They also estimate a substellar-to-stellar objects ratio of $R_{ss} \lesssim 0.65$.

In order to improve the sensitivity to the faintest objects against the background nebular emission, Lucas et al. (2005) collect *JHK* photometry in a region in the ONC $\sim 3'$ off the Trapezium cluster (roughly in our Region 2, see Fig. 5.1) in the S-E direction. They thus provide the deepest photometric IMF, finding a characteristic mass $M^c \sim 0.2$ $M_\odot$ and a slow decline in the IMF in the $-1 < M_L < -2.2$ range with Γ=0.31.

Globally, these IMFs are remarkably similar: together with our derived IMFs (Fig. 5.7), they all have Salpeter-like high-mass slopes, peak at subsolar masses, and decline in frequency with decreasing mass below the hydrogen-burning limit. While the IMFs share these global features, it seems that the fine details, such as the Salpeter slope in the high-mass range or the peak position, are precluded by the differences between the applied methodologies.

Moreover, at the low-mass end, the IMF derivations appear to diverge, and it is unclear how to make detailed comparisons between the different methods. In Sect. 3.5.2 we discussed the differences between the PMS tracks provided by the current theoretical models, and their inconsistencies with our empirical NIR isochrone, especially for very late spectral types. Since photometrically-derived IMFs primarily depend on the theoretical mass-luminosity relation extracted from PMS track, the derived mass distributions depend on the assumed evolutionary model, cluster distance and age, and this may explain the discrepancies at subsolar masses between the IMFs in Fig. 5.8.

Spectroscopically-derived IMFs depend as well on the assumed PMS tracks. As a matter of fact, PMS K-M stars are on nearly vertical Hayashi tracks in the HRD. As a result, a star's mass derived from the HRD is primarily a function of its assigned $T_{\rm eff}$, i.e. the observed spectral type. This method has two drawbacks. First of all, the conversion from spectral types to temperatures is affected by the uncertainties on the conversion scale for late-type sources, due to their sub-giant gravities (Luhman 1999). Moreover, a star's mass derived based on its $T_{\rm eff}$ is uncertain as a result of differences in the PMS models.

Hence, we conclude that the specific IMFs details, such as the exact location of the peak, cannot be securely identified by these methods, although we can conclude that the ONC IMF peaks at subsolar masses somewhere at $\sim$0.2 $M_{\odot}$ and decreases crossing the hydrogen burning limit. Moreover, due to the uncertainties in the current PMS models and on the assumptions on the cluster parameters, it is still controversial whether the ONC IMF keeps decreasing in the substellar mass range or it shows a secondary peak, indicating an alternative formation mechanism for very low-mass objects.

5.4 Summary

In this chapter we have used our results obtained in Chapter 1-4 in order to photometrically-derive the IMF of the ONC.

First of all, using the OMC-1 extinction map computed is Chapter 2, we have computed the expected galactic CMDs as seen through the bulk of the OMC-1. This allow us to derive the contamination-completeness corrected (J,J-H) CMDs of the ONC, canceling out the contribution from the contaminant population.

We have also introduced a statistical algorithm, applicable to any population of coeval stars, which derives the mass distribution of the stars given the observed JHK_S photometry and a reference isochrone. Our algorithm takes into account the presence of interstellar extinction and NIR excess (Chapter 4), which typically affect the observed photometry of young PMS stars as the ones in the ONC.

Finally, we have combined the two previous results with our empirical NIR isochrone for the ONC (Chapter 3), and we have converted the NIR magnitudes into masses. Taking into account the statistical incidence of contaminant sources in the analyzed sample of stars, we have derived our statistical estimate of the IMF at different distances from the Trapezium cluster. Our results show that, consistently with previous results, the mass distribution of the cluster is peaked at $\sim 0.16 M_{\odot}$ and falls off crossing the hydrogen burning limit, continuously decreasing in the BDs domain down to $\sim 0.03 M_{\odot}$. We have also estimated the substellar-to-stellar objects ratio in the ONC, finding that it decreases with increasing distance from the cluster center. This result may thus suggest that BDs are preferentially formed in the gravitational potential well where the Trapezium cluster was formed, as indicated by the gravitational fragmentation mechanism of star formation.

Conclusion

The main goal of this work has been the characterization of the young population of the ON. These studies aimed at the determination of the IMF, which is still under debate, particularly in the very low-mass and sub-stellar regimes.

The data come from the NIR survey of the ONC performed using the ISPI imager mounted at the Blanco 4m telescope of CTIO, in the framework of the HST Treasury Program on the ONC. An area of about 0.3 deg^2 was observed in the J, H and K_S broad bands.

In order to characterize the stellar population of stars in the cluster in terms of luminosity, temperature, mass and age, the NIR data have been combined with simultaneous optical measurements, HST observations from the Treasury Program and spectroscopic characterization available in literature for the ONC.

The conclusions are as follows:

- we assembled a photometric catalog containing ∼7,800 sources. This represents the largest NIR catalog of the ONC to date. Our sensitivity limits allow to detect objects of a few Jupiter masses under about $A_V \simeq$10 magnitudes of extinction;

- due to the optical thickness of the OMC-1, located at the backdrops of the ONC, the NIR CMDs allow to statistical discriminate cluster members and contaminant stars. The two samples have been statistically analyzed to derive the extinction maps of the OMC-1 and the foreground ON. The former generally accounts for the largest amount of extinction, typically $A_V \gtrsim$6, steeply rising up to $A_V \gtrsim$30 in the direction of the Trapezium cluster. The extinction toward the ON is lower, $A_V \lesssim$3, with a peak value $A_V \sim$6 in the direction of the Dark Bay feature. Our findings agree with previous studies of the ON. Our derived maps for the OMC-1 and the ON are available as FITS files at CDS;

- we accurately analyzed a sample of ∼300 stars with measured temperatures, luminosities and photospheric NIR photometry to test current atmospheric and evolutionary models for low-mass PMS stars and BDs. Despite the latest improvements in the synthesis of stellar spectra, we found indications on inaccuracies in the models. We thus propose our empirically-determined average isochrone of the ONC. Comparing our empirical isochrone to current theoretical models, we found that the theoretical PMS isochrones generally provide $T_{\rm eff}$–$\log L$ relations too steep compared to our observational data, in particular at very late spectral types;

- we have analyzed NIR excess of a sample of ONC members with previous spectroscopic characterization, and we found that the flux excess in the three JHK_S bands strongly correlate with each other. We have also found that the observed correlations are consistent with the JHK_S fluxes radiated by a circumstellar disk, plus the contribution from the accretion luminosity for the subsample of accreting objects. The observed fraction of disked stars ($\gtrsim$ 20% of the total sample) does not depend on stellar mass or stellar age, while it increases with the presence of ongoing accretion. This is a selection effect, due to the twofold effect of ongoing mass accretion: (1) it heats up the disk enhancing its NIR luminosity; and (2) the continuum SED of the accretion column contributes to the total NIR excess. We also found that the incidence of disks increases with decreasing distance from the cluster center, consistently with the fact that the UV radiation field propagating in the HII region photoevaporate circumstellar disks. The NIR detectability of these system is thus enhanced by the fact that the hot photoevaporated matter represents an extra-source of NIR radiation.

- we statistically determined the photometrically-derived IMF of the ONC, taking into account the presence of contaminant stars in our catalog and the possibility that the observed NIR photometry is contaminated by circumstellar NIR excess. Consistently with previous results, we found that the mass distribution of the cluster is peaked at $\sim 0.16 M_\odot$ and falls off crossing the hydrogen burning limit, continuously decreasing in the BDs domain down to $\sim 0.03 M_\odot$. We also estimated the substellar-to-stellar objects ratio in the ONC, finding that it decreases with increasing distance from the cluster center.

To study a cluster's IMF in more than just a statistical sense, spectroscopy is needed to confirm cluster membership of individual stars and uniquely determine location in the HRD (and hence mass). For this reason, we have planned to perform spectroscopic observations of the ON. Priority A time was granted during ESO period 86A with VLT+VIMOS for the multi-object spectroscopic observations of ∼100 VLMSs and BDs in the ONC. This project aims at the spectroscopic confirmation of brown dwarfs candidate in the ONC through several diagnostics in the optical-red wavelength range. In particular, the analysis of the TiO and VO spectral bands allow the derivation of spectral types for cool atmospheres, while the LiI λ6708 Åline, the H_α line, the CaII triplet at 8498/8542/8662 Åand the NaI 8183/8195 Ådoublet as youth indicators. Data reduction and analysis is ongoing.

List of Acronyms

2CD	Two-Color Diagram
BD	Brown Dwarf
CDS	Centre de Données astronomiques de Strasbourg
CMD	Color-Magnitude Diagram
CTTS	Classical T Tauri Star
HRD	Hertzsprung-Russel Diagram
HST	Hubble Space Telescope
IMF	Initial Mass Function
ISPI	Infrared Side Port Imager
LF	Luminosity Function
MLR	Mass-Luminosity Relation
NIR	Near-Infrared
OMC-1	Orion Molecular Cloud 1
ON	Orion Nebula
ONC	Orion Nebula Cluster
PMS	Pre-Main Sequence
PSF	Point Spread Function
SED	Spectral Energy Distribution
SNR	Signal-to-Noise Ratio
VLMS	Very Low Mass Star
WTTS	Weak-emission T Tauri Star

Bibliography

Allard, F., Hauschildt, P. H., Alexander, D. R., Tamanai, A., & Schweitzer, A. 2001, ApJ, 556, 357

Allard, F., Homeier, D., & Freytag, B. 2010, arXiv:1011.5405

Arce, H. G., & Goodman, A. A. 1999, ApJ, 512, L135

Baldwin, J. A., Ferland, G. J., Martin, P. G., Corbin, M. R., Cota, S. A., Peterson, B. M., & Slettebak, A. 1991, ApJ, 374, 580

Baraffe, I., Chabrier, G., Allard, F., & Hauschildt, P. H. 1998, A&A, 337, 403

Baraffe, I., Chabrier, G., Allard, F., & Hauschildt, P. H. 2002, A&A, 382, 563

Bastian, N., Covey, K. R., & Meyer, M. R. 2010, ARA&a, 48, 339

Biazzo, K., Randich, S., & Palla, F. 2011, A&A, 525, A35

Black, D. C. 1980, ICARUS, 43, 293

Blagrave, K. P. M., Martin, P. G., Rubin, R. H., Dufour, R. J., Baldwin, J. A., Hester, J. J., & Walter, D. K. 2007, ApJ, 655, 299

Bonnell, I. A., Clark, P., & Bate, M. R. 2008, MNRAS, 389, 1556

Bonnell, I. A., Smith, R. J., Clark, P. C. & Bate, M. R. 2011, MNRAS, 410, 2339

Briceño, C., Luhman, K. L., Hartmann, L., Stauffer, J. R., & Kirkpatrick, J. D. 2002, ApJ, 580, 317

Brown, A. G. A., de Geus, E. J., & de Zeeuw, P. T. 1994, A&A, 289, 101

Burrows, A., Saumon, D., Guillot, T., Hubbard, W. B., & Lunine, J. I. 1995, Nature, 375, 299

Calvet, N., Patino, A., Magris, G. C., & D'Alessio, P. 1991, ApJ, 380, 617

Calvet, N., Magris, G. C., Patino, A., & D'Alessio, P. 1992, Rev. Mexicana Astron. Astrofis., 24, 27

Calvet, N., & Gullbring, E. 1998, ApJ, 509, 802

Cardelli, J. A., Clayton, G. C., & Mathis, J. S. 1989, ApJ, 345, 245

Carpenter, J. M., Meyer, M. R., Dougados, C., Strom, S. E., & Hillenbrand, L. A. 1997, AJ, 114, 198

Carpenter, J. M. 2001, AJ, 121, 2851

Chabrier, G., Baraffe, I., Allard, F., & Hauschildt, P. 2000, ApJ, 542, 464

Cieza, L. A., Kessler-Silacci, J. E., Jaffe, D. T., Harvey, P. M., & Evans, N. J., II 2005, ApJ, 635, 422

Costero, R., & Peimbert, M. 1970, Boletin de los Observatorios Tonantzintla y Tacubaya, 5, 229

D'Antona, F., & Mazzitelli, I. 1997, Mem. Soc. Astron. Italiana, 68, 807

D'Antona, F., & Mazzitelli, I. 1998, Brown Dwarfs and Extrasolar Planets, 134, 442

Da Rio, N., Robberto, M., Soderblom, D. R., Panagia, N., Hillenbrand, L. A., Palla, F., & Stassun, K. 2009, ApJS, 183, 261

Da Rio, N., Robberto, M., Soderblom, D. R., Panagia, N., Hillenbrand, L. A., Palla, F., & Stassun, K. G. 2010, ApJ, 722, 1092

Da Rio, N., in preparation

Dobashi, K., Uehara, H., Kandori, R., Sakurai, T., Kaiden, M., Umemoto, T., & Sato, F. 2005, PASJ, 57, 1

D'Orazi, V., Randich, S., Flaccomio, E., Palla, F., Sacco, G. G., & Pallavicini, R. 2009, A&A, 501, 973

Feigelson, E. D., & Montmerle, T. 1999, ARA&a, 37, 363

Fischer, W., Edwards, S., Hillenbrand, L., & Kwan, J. 2011, ApJ, 730, 73

Ferland, G. J., Korista, K. T., Verner, D. A., Ferguson, J. W., Kingdon, J. B., & Verner, E. M. 1998, PASP, 110, 761

Goldsmith, P. F., Bergin, E. A., & Lis, D. C. 1997, ApJ, 491, 615

Greve, A., Castles, J., & McKeith, C. D. 1994, A&A, 284, 919

Haisch, K. E., Jr., Lada, E. A., & Lada, C. J. 2001, ApJ, 553, L153

Hartmann, L., & Burkert, A. 2007, ApJ, 654, 988

Hartmann, L. 2009, Accretion Processes in Star Formation: Second Edition, by Lee Hartmann. ISBN 978-0-521-53199-3. Published by Cambridge University Press, Cambridge, UK, 2009.

Hennebelle, P., & Chabrier, G. 2008, ApJ, 684, 395

Hillenbrand, L. A. 1997, AJ, 113, 1733

Hillenbrand, L. A., & Hartmann, L. W. 1998, ApJ, 492, 540

Hillenbrand, L. A., Strom, S. E., Calvet, N., Merrill, K. M., Gatley, I., Makidon, R. B., Meyer, M. R., & Skrutskie, M. F. 1998, AJ, 116, 1816

Hillenbrand, L. A., & Carpenter, J. M. 2000, ApJ, 540, 236

Hillenbrand, L. A., & White, R. J. 2004, ApJ, 604, 741

Hillenbrand, L. A., Bauermeister, A., & White, R. J. 2008, 14th Cambridge Workshop on Cool Stars, Stellar Systems, and the Sun, 384, 200

Hillenbrand, L. A. 2009, IAU Symposium, 258, 81

Jayawardhana, R. 2010, Highlights of Astronomy, 15, 729

Johnson, H. L. 1967, ApJ, 150, L39

Kenyon, S. J., & Hartmann, L. 1987, ApJ, 323, 714

Kenyon, S. J., & Hartmann, L. W. 1990, ApJ, 349, 197

Kenyon, S. J., & Hartmann, L. 1995, ApJS, 101, 117

Kroupa, P. 2001, MNRAS, 322, 231

Kroupa, P. 2002, Science, 295, 82

Lada, C. J., & Lada, E. A. 2003, ARA&a, 41, 57

Lee, H.-T., Chen, W. P., Zhang, Z.-W., & Hu, J.-Y. 2005, ApJ, 624, 808

Lombardi, M., & Alves, J. 2001, A&A, 377, 1023

Lucas, P. W., & Roche, P. F. 2000, MNRAS, 314, 858

Lucas, P. W., Roche, P. F., & Tamura, M. 2005, MNRAS, 361, 211

Luhman, K. L. 1999, ApJ, 525, 466

Luhman, K. L., Rieke, G. H., Young, E. T., et al. 2000, ApJ, 540, 1016

Luhman, K. L., Stauffer, J. R., Muench, A. A., Rieke, G. H., Lada, E. A., Bouvier, J., & Lada, C. J. 2003, ApJ, 593, 1093

Massey, P. 1998, The Stellar Initial Mass Function (38th Herstmonceux Conference), 142, 17

Menten, K. M., Reid, M. J., Forbrich, J., & Brunthaler, A. 2007, A&A, 474, 515

Meyer, M. R. 1996, PASP, 108, 380

Meyer, M. R., Calvet, N., & Hillenbrand, L. A. 1997, AJ, 114, 288

Muench, A. A., Lada, E. A., Lada, C. J., & Alves, J. 2002, ApJ, 573, 366

Muench, A., Getman, K., Hillenbrand, L., & Preibisch, T. 2008, Handbook of Star Forming Regions, Volume I: The Northern Sky ASP Monograph Publications, Vol. 4. Edited by Bo Reipurth, p.483, 483

Natta, A., & Panagia, N. 1976 A&A, 50, 191

O'Dell, C. R., & Yusef-Zadeh, F. 2000, AJ, 120, 382

O'Dell, C. R., Muench, A., Smith, N., & Zapata, L. 2008, Handbook of Star Forming Regions, Volume I, 544

O'Dell, C. R., Henney, W. J., Abel, N. P., Ferland, G. J., & Arthur, S. J. 2009, AJ, 137, 367

Osterbrock, D. E., Tran, H. D., & Veilleux, S. 1992, ApJ, 389, 305

Palla, F., & Stahler, S. W. 1999, ApJ, 525, 772

Persi, P., Marenzi, A. R., Olofsson, G., et al. 2000, A&A, 357, 219

Persson, S. E., Murphy, D. C., Krzeminski, W., Roth, M., & Rieke, M. J. 1998, AJ, 116, 2475

Peterson, D. E., & Megeath, S. T. 2008, Handbook of Star Forming Regions, Volume I, 590

Prusti, T., Whittet, D. C. B., Assendorp, R., & Wesselius, P. R. 1992, A&A, 260, 151

Reggiani, M., Robberto, M., Da Rio, N., Meyer, M. R., Soderblom, D. R., & Ricci, L. 2011, arXiv:1108.1015

Reipurth, B., & Clarke, C. 2001, AJ, 122, 432

Ricci, L., Robberto, M., & Soderblom, D. R. 2008, AJ, 136, 2136

Riddick, F. C., Roche, P. F., & Lucas, P. W. 2007, MNRAS, 381, 1077

Robberto, M., Beckwith, S. V. W., & Panagia, N. 2002, ApJ, 578, 897

Robberto, M., Song, J., Mora Carrillo, G., Beckwith, S. V. W., Makidon, R. B., & Panagia, N. 2004, ApJ, 606, 952

Robberto, M., Soderblom, D. R., Scandariato, G., Smith, K., Da Rio, N., Pagano, I., & Spezzi, L. 2010, AJ, 139, 950

Robin, A. C., Reylé, C., Derrière, S., & Picaud, S. 2003, A&A, 409, 523

Robitaille, T. P., Whitney, B. A., Indebetouw, R., Wood, K., & Denzmore, P. 2006, ApJS, 167, 256

Salpeter, E. E. 1955, ApJ, 121, 161

Scandariato, G., Robberto, M., Pagano, I., & Hillenbrand, L. A. 2011, A&A, 533, A38

Scandariato, G., Robberto, M., Pagano, I. 2012, A&A, *in preparation*

Schlegel, D. J., Finkbeiner, D. P., & Davis, M. 1998, ApJ, 500, 525

Siess, L., Dufour, E., & Forestini, M. 2000, A&A, 358, 593

Silverman, B. W. 1986, Monographs on Statistics and Applied Probability, London: Chapman and Hall, 1986

Skrutskie, M. F., Dutkevitch, D., Strom, S. E., Edwards, S., Strom, K. M., & Shure, M. A. 1990, AJ, 99, 1187

Slesnick, C. L., Hillenbrand, L. A., & Carpenter, J. M. 2004, ApJ, 610, 1045

Swenson, F. J., Faulkner, J., Rogers, F. J., & Iglesias, C. A. 1994, ApJ, 425, 286

Tognelli, E., Prada Moroni, P. G., & Degl'Innocenti, S. 2011, arXiv:1107.2318

Vicente, S. M., & Alves, J. 2005, A&A, 441, 195

Whitworth, A., Bate, M. R., Nordlund, Å., Reipurth, B., & Zinnecker, H. 2007, Protostars and Planets V, 459

Xin-yue, E, Zhi-bo, J., Yan-ning, F. , 2009, Chinese Astronomy and Astrophysics, 33, 139

Yi, S. K., Kim, Y.-C., & Demarque, P. 2003, ApJS, 144, 259